UNIVERSITY OF CALIFORNIA, SAN DIEGO

Coupled Plasmonic Nanostructures for Improved Biological Sensing Applications

A dissertation submitted in partial satisfaction of the
requirements for the degree
Doctor of Philosophy

in

Electrical Engineering (Photonics)

by

Hai Ping Matthew Chen

Committee in charge:

Professor Yeshaiahu Fainman, Chair
Professor Shu Chien
Professor Alex Groisman
Professor Vitaliy Lomakin
Professor Paul Yu

2012

The dissertation of Hai Ping Matthew Chen is approved, and it is acceptable in quality and form for publication on microfilm and electronically:

_____

_____

_____

_____

_____

Chair

University of California, San Diego

2012

DEDICATION

To my grandmother and my parents for all the sacrifices that they have made so I could be where I am today

EPIGRAPH

An investment in knowledge pays the best interest. —Benjamin Franklin

TABLE OF CONTENTS

LIST OF FIGURES

LIST OF TABLES

ACKNOWLEDGEMENTS

Right off the bat, I would like to thank my Ph.D. advisor, Professor Yeshaiahu (Shaya) Fainman, for his support and guidance during this journey, especially for sticking with me during the early years as I struggle to find my Ph.D. calling (i.e., research topic). I would also like to thank all my committee members, Profs. Fainman, Chien, Groisman, Lomakin, and Yu, for serving on my committee and offering invaluable advices on how to improve my research.

I would also like to thank all the UNO group members throughout the years from Dr. Robert Saperstein when I first joined the group to current members such as Janelle, Qing, Olesya, and Joanna. I enjoyed the hiking and camping trips that we had. I also would like to thank Dr. Aleksander Simics and Dr. Boris Slutsky for their computer support throughout the years and also thank Aleks for introducing me to LaTeX and helping me with it. I would like to thank all the Nano3 staff (Bernd, Larry, Ryan, Sean, Maribel, and Xuekun) for their support of the equipments in the cleanroom, without their help the fabrication would not be possible. I would like to say a special thank you to Dr. Lin Pang for his help, guidance, and encouragement throughout the entirety of my Ph.D. study. I remembered it was Lin who introduced me to the field of plasmonics, specifically using surface plasmon resonance techniques for biosensing applications. It was Lin and his selflessness and unending help that have made the completion of this dissertation possible.

I would also like to take this opportunity to thank Professor Shun-Lien Chuang from the University of Illinois, Urbana-Champaign, for introducing me to the field of optics and photonics. I still remember when my very good friend, Dr. Maytee Lerttamrab, and I entered UIUC, we both listed Communication Theory as a sub-field. However, while taking Prof. Chuang's 'Electromagnetic waves and electro-optics' class, which was my very first optics class, we both decided to switch to optoelectronics and photonics. We marveled at Prof. Chuang's ability to lecture and write complex Maxwell's equations on the board without any notes. Secondly, I would also like to thank my Master's advisor, Professor Kent Choquette, for his guidance, kindness, understanding, and humor. One of the hardest things that I

had to do at UIUC was to tell Kent that I did not want to pursue my Ph.D. at UIUC. He and his wife, Lori, made me feel at home at their house as we cheered for the Fighting Illini football team. Thirdly, I would like to thank Dr. Curtis Kidner and Daniel Garcia of NAWCWD, China Lake, for their mentorship and advices during my first few years working there. I learned a lot from them on how to be a successful engineer/scientist.

Finally, I would like to thank my family (my grandmother, parents, brother and sister) for their endless support and encouragement throughout my studies ever since I was young. I appreciate all the sacrifices that my parents have made, working long hours for 6 or 7 days a week to make ends meet. I will never be able to repay what they have done for me, but I hope the completion of my Ph.D. study will make them even prouder of me and justify all their sacrifices. Last but not less, I would like to thank my fiancée, Johana, for her company throughout some long evenings and mornings while we were both in the lab working to make progress in our respective researches. She has made this journey enjoyable and worthwhile with her unique personality, humors, and laughters. Now, I look very much forward to the next chapter of our lives spend together.

This dissertation was prepared with LaTeX using the unofficial UCSD doctoral dissertation template (http://ucsd-thesis.googlecode.com).

Chapter 3, in part, is a reprint of the material as it appears in "Three-dimensional composite metallodielectric nanostructure for enhanced surface plasmon resonance sensing," H. M. Chen, L. Pang, A. Kher, Y. Fainman, *Applied Physics Letters*, 94, 073117, 2009. The dissertation author was the primary investigator and author of this paper. The co-authors listed either helped or supervised the research.

Chapter 4, in part, is a reprint of the material as it appears in "Controlled detection in composite nanoresonant array for surface plasmon resonance sensing," L. Pang, H. M. Chen, L. L. Wang, J. M. Beechem, Y. Fainman, *Optics Express*, 17, 14700-14709, 2009. The dissertation author performed the simulations and helped with the experiments and writing of the publication.

Chapter 5, in part, is a reprint of the material as it appears in "Real-time

template-assisted manipulation of nanoparticles in a multilayer nanofluidic chip," H. M. Chen, L. Pang, M. S. Gordon, Y. Fainman, *Small*, 7, 2750-2757, 2011. The dissertation author was the primary investigator and author of this paper. The co-authors listed either helped or supervised the research.

Chapter 6, in part, has been recently submitted for publication of materials, entitled, "Controllable orientation of nanotorch structures leading to uniform surface enhanced Raman scattering detection," H. M. Chen, L. Pang, A. King, G. M. Hwang, Y. Fainman. The dissertation author was the primary investigator and author of this paper. The co-authors listed either helped or supervised the research.

VITA

1996-2000	Bachelor of Science in Electrical Engineering *magna cum laude*, University of California, Davis
2000-2002	Master of Science in Electrical Engineering, University of Illinois, Urbana-Champaign
2006-2012	Doctor of Philosophy in Electrical Engineering (Photonics), University of California, San Diego

PUBLICATIONS

H. M. Chen, L. Pang, A. Kher, Y. Fainman, "Three-dimensional composite metallodielectric nanostructure for enhanced surface plasmon resonance sensing," *Applied Physics Letters*, 94, 073117 (2009).

L. Pang, H. M. Chen, L. L. Wang, J. M. Beechem, Y. Fainman, "Controlled detection in composite nanoresonant array for surface plasmon resonance sensing," *Optics Express*, 17, 14700-14709 (2009).

H. M. Chen, L. Pang, M. S. Gordon, Y. Fainman, "Real-time template-assisted manipulation of nanoparticles in a multilayer nanofluidic chip," *Small*, 7, 2750-2757 (2011).

H. M. Chen, L. Pang, A. King, G. M. Hwang, Y. Fainman, "Controllable orientation of nanotorch structures leading to uniform surface enhanced Raman scattering detection."(submitted).

L. Pang, H. M. Chen, L. Freeman, Y. Fainman, "Optofluidics devices and applications in photonics, sensing, and imaging"*Lab on a Chip*, (accepted), 2012.

ABSTRACT OF THE DISSERTATION

Coupled Plasmonic Nanostructures for Improved Biological Sensing Applications

by

Hai Ping Matthew Chen

Doctor of Philosophy in Electrical Engineering (Photonics)

University of California, San Diego, 2012

Professor Yeshaiahu Fainman, Chair

Plasmonics, a sub-field of nanophotonics, has attracted amazing interests in recent years due to its promise of revolutionary impacts on nanotechnologies, medicine, and our daily lives. In short, plasmonics guides, confines, localizes, and enhances electromagnetic waves to a small area to enable novel applications such as plasmonic waveguides, sub-wavelength diffraction lithography and imaging, higher photovoltaic efficiency, sub-wavelength lasers, and biological sensing.

The first part of this dissertation will introduce the general concepts of plasmonics and its applications in biological sensing, starting from Maxell's equations and the Drude model of metal. In the second part, it will delve into the specifics of designing, simulating, fabricating, and characterizing nanostructures

that show improved performance characteristics over previous published results. Plasmonic coupling of propagating surface plasmon polaritons and localized plasmons is utilized to fabricate three-dimensional mushroom-like metallodielectric array for improved surface plasmon resonance biological sensing over conventional nanohole array. It is used to determine the hydrophilicity of a surface by monitoring the shift in resonant wavelength. In addition, the fabricated structure is used to detect specific binding events between biotinylated-bovine serum albumin and streptavidin protein and demonstrates an improved limit of detection.

The real-time control and manipulation of nanoparticles in a biocompatible aqueous solution is demonstrated in a multilayer micro/nanofluidic chip platform by using voltage control. This will have future applications to control and position nanoparticles and biomolecules to an area of maximum field enhancement to co-localize the analyte with the plasmonic nanostructure for maximal enhancement efficiency. Finally, the intra-particle plasmonic coupling of a nanotorch structure is utilized for surface enhanced Raman scattering detection to yield high enhancement factor and better than 80% Raman signal uniformity due to the fabrication of controllable rim opening of the nanotorch and the deterministic orientation of the structure. The common theme of this dissertation is coupled plasmonic nanostructures for improved biological sensing applications.

Chapter 1

Introduction

Plasmonics is an emerging, interdisciplinary field that combines material science, physics, nanophotonics, and computational simulation in revealing many fascinating phenomena that have led to discoveries, advancements, and applications with potential deep technological and societal impacts, ranging from sub-diffraction imaging and lithography, biological sensing and drug design, solar cells, improved semiconductor laser designs, and much more. It can be considered a sub-field within nanophotonics, which is a branch within electrical or optical engineering that studies the behavior and interaction of light with particle matters at the sub-wavelength scales (here, nanometer scale). The underlying physics of plasmonics is based on the interaction between electromagnetic waves and conduction electrons at metal-dielectric interfaces or in metallic nanostructures to produce an enhanced optical near-field with sub-wavelength dimension. The electromagnetic field will be dependent on the size and shape of the nanostructure that interacts with light.

The field of plasmonics has its roots more than a hundred years ago with Rayleigh's diffraction gratings, Wood's anomaly intensity of visible light reflected from metallic gratings [1], Drude's study of metal [2], Mie's theoretical treatment of particles [3], and Zenneck's and Sommerfeld's surface waves of radio frequency. More recently, Thomas Ebbessen and colleagues' discoveries on extraordinary transmission of subwavelength nanohole have attracted more curious minds into this burgeoning field [4].

1.1 Motivation

With current advancements in the microelectronic industry and the ever increasing speed of microprocessors, it is easy to assume that this trend will continue indefinitely. However, like all things in life, it will come to an end: that is, Moore's law of doubling transistor density every 2 years is unsustainable. The integration and miniaturization of modern electronic devices is rapidly approaching its fundamental speed and bandwidth limitations. However, there is hope: one of the most promising solutions is believed to be replacing electronic signals used for information carriers with light. This has already happened to some extent for long distance communication with the implementation of long-haul optical fiber communication. More recently, advances have been made in short-distance communication such as chip-to-chip fiber communication. However, a major problem still with using electromagnetic waves as information carriers in optical signal processing devices is the low levels of integration and miniaturization compare to electronics. The issue arises because of the diffraction of light, which precludes the localization of electromagnetic waves into an area much smaller than the wavelength of light in the material.

However, materials with a negative dielectric permittivity, such as noble metals, can solve this diffraction roadblock by localizing electromagnetic waves at the optical frequency into nanometer scale areas, as small as a few nanometers by utilizing metal structures and interfaces to guide surface plasmon polariton (SPP) modes. Plasmonics is thus a field that could potentially combine the compactness and integration of an electronic circuit with the huge bandwidth of a photonic network. The potential applications include plasmonic chips that function as ultra-low-loss optical interconnects and plasmonic circuits and components that can guide light within ultra-compact optically functional devices [5–8].

Besides improvement in miniaturization and integration, plasmonics also has the potential to improve the sensitivity and limit of detection in biological sensing by utilizing propagating surface plasmon polaritons and/or localized surface plasmons (LSPs). Generally speaking, sensing can be based either on the refractive index dependence of the plasmon resonance or on the amplification of

the near field of the nanostructure. In surface plasmon resonance (SPR) sensors that utilize SPPs, changes in the dielectric constant of the medium surrounding the metallic nanostructure are detected by monitoring the shift of the SPR absorption maximum. Although for this modality, the SPR response is not chemically specific, but can be overcome by using nanoparticles conjugated to specific antibodies or DNA, which allows for binding specificities of specific target-receptor molecules, such as biotin-streptavidin [9, 10]. The second modality is the amplification of the near field of the nanostructures and using that local field enhancement in applications such as localized surface resonance (LSP) or surface enhanced Raman scattering (SERS) sensing. In LSP sensor, minute changes in the refractive index on the surface of the metal structure will cause a change in the resonance of the localized plasmon of the structure. While LSP sensors are not expected to compete with SPR sensors based on thin films in detecting bulk refractive index change, they are more likely to enable a higher sensitivity to local perturbation such as molecular bindings on the surfaces. The main advantage is the possibility of tailoring the optical properties by careful design in controlling and changing their size, shape, composition, and environment [11–13]. Using nanosphere lithography (NSL), large arrays of LSP sensors have been fabricated to detect amyloid-β in Alzheimer's disease [14], anti-biotin antibody [11], and surface-assembled monolayer of 1-hexadecanethiol molecules with zeptomole sensitivity [15].

The chemical synthesis of noble metal nanostructures of varying shapes and sizes has enabled inexpensive fabrication of plasmonic materials, such as triangles [16], cubes [17], metallic half-shells [18], and gold nanorice [19] with controllable sizes and narrow size distribution. Another approach is colloidal lithography, whereby close-packed array of polystryrene nanoparticles is formed followed by noble metal evaporation to fabricate nanometer-size, patterned surface of a large area such as the silver nanoprism [9]. However, the controlled assembly and integration of nanoparticles into plasmonic devices remains a challenge. We will address this issue in Chapter 5 when we introduce real-time assembly of nanoparticles into an array in an aqueous solution.

Presently, there have been extensive research into developing and optimizing

SERS substrates with good uniformity in a practical and an economical fashion. The local field enhancement is known to be very high between small gaps of coupled nanostructures. Carefully designing these optical nanoantenna structures have been investigated such as the nanorods [20] and bowtie antennas. The bowtie antenna's gap and polarization dependence were carefully studied [21] and the structure was found to increase the fluorescence by a few orders of magnitude [22].

With the understanding that plasmonic properties could be manipulated and engineered by careful design, together with faster and more powerful computers and the ever increasing accuracies of simulation softwares in simulating these physical phenomena, there have been a myriad display of creativity and advancements in the field of plasmonics. Yet, it is still in its infancy and the practical realization, integration and commercialization of all plasmonic components designed for generation, manipulation and detection is still challenging and faces many obstacles. There is currently lots of interests in the detection of low concentration of proteins and small molecules with potential applications in biomedicine, drug discovery, food assessment, and even military applications such as biological warfare in detecting hazardous bioagents. This dissertation hopes to contribute at least in some aspects to this fascinating field. A common theme of the research is fabricating plasmonic devices in an economical fashion while improving the sensitivity of biological detection without resorting to the high-cost and serial-speed of electron beam lithography.

1.2 Organization of dissertation

This dissertation will first review some of the background materials needed to understand this dissertation and in general, the field of plasmonics in Chapter 2, beginning from first principle—Maxwell's equations. Next, it will derive the propagating surface plasmon polaritons dispersion relation and discuss methods to overcome the momentum mismatch to achieve phase matching. The chapter will next discuss localized surface plasmons, a second type of plasmons that are important in plasmonics. The chapter will close with an introduction to surface

enhanced Raman scattering and the metrics used to evaluate its effectiveness.

Chapter 3 will discuss a new three-dimensional (3-D) composite metallodielectric nanostructure for enhanced surface plasmon resonance biological sensing. This novel mushroomlike nanostructure combines both SPPs and LSPs to produce higher local field enhancement as confirmed with simulations. The ease of fabrication is very beneficial for low-cost, large-area manufacturable SPR sensors. Using these fabricated devices, the hydrophilicity of the gold surface is determined in the absence and presence of a self-assembled monolayer.

Chapter 4 will present specific binding event measurements between a ligand and an analyte using these mushroomlike nanostructures. The limit of detection is improved to sub-nanomolar, which is a substantial improvement to the tens of nanomolar in conventional nanohole array SPR sensor.

Chapter 5 will discuss how to deliver and control nanoparticles (and potentially, biomolecules) in an aqueous environment. The ability to control dynamically the flow and placement of nanoparticles in a biocompatible, aqueous environment will have profound impact in advancing the fields of nanoplasmonics, nanophotonics, and medicine. We will demonstrate an approach that is based on electrokinetic forces to dynamically control the placement of nanoparticles into a predefined two-dimensional pattern. The technique uses an applied voltage to manipulate nanoparticles in a multilayer nanofluidic chip architecture and demonstrate the ability to hold and release these nanoparticles over nanochannels. The results presented are important as they provide a new method that is capable of dynamically capturing and releasing nanoscale particles and biomolecules in an aqueous environment which could lead to creation of reconfigurable nanostructure patterns for nanoplasmonic, nanophotonic, biological sensing, and drug delivery applications.

Chapter 6 will present recent works on nanotorch structure as a single SERS substrate. Finite element method simulations, fabrication process, and SERS characterization are presented that showed smaller rim opening will yield higher local field enhancement and thus a higher SERS enhancement factor due to plasmonic coupling between the tips, edges, and cavity of the nanotorch. Since the fabrica-

tion technique enables fabrication of controllable rim opening and deterministic orientation, the uniformity of the Raman signal for all the analyzed mode of the analyte benezenethiol adsorbed onto the gold nanotroch is better than 80%.

Finally, Chapter 7 will summarize my contributions during my Ph.D. study and offer future directions and outlooks.

Chapter 2

Background on plasmons

In this chapter, we will first discuss the properties of metal in the optical regime as it relates to the field of plasmonics in order to understand the rest of the dissertation. We will derive the very important complex dielectric function of the free electron gas, which is central to the field of plasmonics. Next, we will introduce propagating surface plasmon polaritons (SPPs) and the dispersion relation. Different coupling methods to the SPP modes are discussed. We will next introduce another type of plasmons—localized surface plasmons (LSPs), which unlike SPPs, are non-propagating and depend on the shape, size, and composition of the nanostructure. Lastly, we will introduce Raman scattering and methods to increase the Raman signal through surface enhanced Raman scattering (SERS) techniques.

2.1 Maxwell's equations and electromagnetic wave propagation

The particle-photon interaction of metals with electromagnetic (EM) fields can be understood from classical physics based on Maxwell's equations without resorting to quantum mechanics, since the high density of free carriers results in minute spacings of the electron energy levels compared to the thermal energy

excitations k_BT at room temperature.[1] Therefore, in this dissertation, only the classical framework of the interaction of metal with electromagnatic waves are considered. Yet this treatment does not preclude interesting and unexpected optical phenomena from occurring due to the metal's strong frequency dependence.

From our daily lives, we experience the shiny, reflective properties of metals at the visible spectrum such as in mirrors, telescopes, or even kitchen silver wares, which, at first glance, we would assume that electromagnetic propagation do not penetrate through these metals. This is a valid assumption in the low-frequency regime, such as the microwave and the far-infrared spectral regions, where the perfect or good conductor approximation of infinite or fixed finite conductivity is valid for most purposes since only a negligible fraction of the incident EM waves penetrates through the metal. However, at the higher frequencies toward the infrared and the visible spectrum, field penetration does increase significantly for certain metals, leading to increased dissipation of photonic devices to this regime. At the ultraviolet frequencies, alkali metals acquire dielectric character and allow the propagation of EM waves with varying degree of attenuation depending on the details of the electronic band structure and can exhibit an ultraviolet transparency with an almost free-electron-like response [23]. However, for noble metals such as gold or silver, transitions between electronic bands lead to strong absorption in this frequency band. Novel optical properties can result from the material's extremely small size. An example is the color change associated with colloidal gold nanoparticles. Bulk gold exhibits its yellow color, while gold nanoparticles of sizes ranging from 10 nm to 100 nm exhibit a rich red color. The critical size where these novel properties are evident is related to the mean free path of the conduction electrons in the metal.

The dispersive properties of metal can be described by a complex dielectric function, $\epsilon(\omega)$, which is fundamental to the field of plasmonics and provides the basis of all phenomena described in this dissertation. The underlying physics of the strong frequency-dependent optical response is due to a change in the phase of the induced currents with respect to the driving electromagnetic field for frequencies

[1]Metal has a high free electron density $n_{\mathrm{e}} \approx 10^{23}\,\mathrm{cm}^{-3}$

approaching the reciprocal of the characteristic electron relaxation time τ of the metal [23]. Like most physical phenomena, we can begin with the Maxwell's equations of electromagnetism and is presented first as a background refresher. The advantage of this approach is that details of the fundamental interactions between charged particles inside the media and the EM fields do not need to be taken into account since the rapidly changing microscopic fields are averaged over distance much larger than the underlying nanostructure [24].

As a starting point, the macroscopic EM waves can be expressed by Maxwell's equations of the form:

$$\nabla \cdot \mathbf{D} = \rho_{\text{ext}} \tag{2.1a}$$

$$\nabla \cdot \mathbf{B} = 0 \tag{2.1b}$$

$$\nabla \times \mathbf{E} = -\frac{\partial \mathbf{B}}{\partial t} \tag{2.1c}$$

$$\nabla \times \mathbf{H} = \mathbf{J_{ext}} + \frac{\partial \mathbf{D}}{\partial t}. \tag{2.1d}$$

The equations link the four fields, $\mathbf{D}$ (the dielectric displacement), $\mathbf{E}$ (the electric field), $\mathbf{H}$ (the magnetic field), and $\mathbf{B}$ (the magnetic flux density), with the external charge and current densities ρ_{ext} and $\mathbf{J_{ext}}$.

These four fields are related to the polarization $\mathbf{P}$ and magnetization $\mathbf{M}$ by

$$\mathbf{D} = \epsilon_0 \mathbf{E} + \mathbf{P} \tag{2.2a}$$

$$\mathbf{H} = \frac{1}{\mu_0}\mathbf{B} - \mathbf{D}, \tag{2.2b}$$

where ϵ_0 and μ_0 are the electric permittivity[2] and magnetic permeability[3] of vacuum, respectively.

In this dissertation, only nonmagnetic media are used; therefore, the magnetic response induce by $\mathbf{M}$ will not be considered but only the electric polarization effects are analyzed. $\mathbf{P}$ describes the electric dipole moment per unit volume inside the material caused by the alignment of microscopic dipoles with the electric field

[2] $\epsilon_0 \approx 8.854 \times 10^{-12}$ F/m
[3] $\mu_0 \approx 1.257 \times 10^{-6}$ H/m

and is related to the internal charge density by $\nabla \cdot \mathbf{P} = -\rho$. Charge conservation, i.e., $\nabla \cdot \mathbf{J} = -\frac{\partial \rho}{\partial t}$, requires that the internal charge and current densities satisfy the following

$$\mathbf{J} = \frac{\partial \mathbf{P}}{\partial t}. \tag{2.3}$$

The advantage of this approach is that the macroscopic electric field includes all polarization effects with both the external and induced fields absorbed into the underlying equation as derived by inserting (2.2a) into (2.1a),

$$\nabla \cdot \mathbf{E} = \frac{\rho_{\text{tot}}}{\epsilon_0}. \tag{2.4}$$

Only isotropic and nonmagnetic media will be considered here, so one can define the constitutive relations as

$$\nabla \cdot \mathbf{D} = \epsilon_0 \epsilon \mathbf{E} \tag{2.5a}$$

$$\nabla \cdot \mathbf{B} = \mu_0 \mu \mathbf{H}, \tag{2.5b}$$

where ϵ is called the dielectric constant or relative permittivity and $\mu = 1$ is the relative permeability of a nonmagnetic medium. The linear relationship between $\mathbf{P}$ and $\mathbf{E}$ can be expressed as

$$\mathbf{P} = \epsilon_0 \chi \mathbf{E}, \tag{2.6}$$

where χ is the dielectric susceptibility and it can be shown to be $\chi = \epsilon - 1$.

Another important constitutive linear relationship is between the internal current density $\mathbf{J}$ and the electric field $\mathbf{E}$, defined via the conductivity σ by

$$\mathbf{J} = \sigma \mathbf{E}. \tag{2.7}$$

There exits a relationship between ϵ and σ and the electromagnetic interaction with metals can be described using either quantity. Historically, at low frequencies σ is used, while at optical frequencies, preference is given to ϵ—the dielectric constant. It is now important to point out that (2.5) and (2.6) are valid only for linear media that do not have temporal or spatial dispersion. Since the optical response of metals is clearly frequency-dependent, the non-locality in time

and space have to be taken into account by generalizing those linear relationships to the Fourier domain [23]

$$\mathbf{D}(\mathbf{K},\omega) = \epsilon_0\epsilon(\mathbf{K},\omega)\mathbf{E}(\mathbf{K},\omega) \tag{2.8a}$$

$$\mathbf{J}(\mathbf{K},\omega) = \sigma(\mathbf{K},\omega)\mathbf{E}(\mathbf{K},\omega). \tag{2.8b}$$

Using equations (2.2a),(2.3) and (2.8) and recalling that in the Fourier domain $\partial/\partial t \rightarrow -i\omega$, we now have the fundamental relationship between the relative permittivity (also known as the *dielectric function*) and the conductivity

$$\epsilon(\mathbf{K},\omega) = 1 + \frac{i\sigma(\mathbf{K},\omega)}{\epsilon_0\omega}. \tag{2.9}$$

For the interaction of light with metals, the general form of the dielectric response $\epsilon(\mathbf{K},\omega)$ can be simplified to $\epsilon(\mathbf{K}{=}\mathbf{0},\omega) = \epsilon(\omega)$ in the limit of a *spatially local* response and is valid as long as the wavelength λ of the light in the material is significantly longer than all characteristic dimensions such as the size of the unit cell or the mean free path of the electrons. At optical frequencies, $\epsilon(\omega) = \epsilon_1(\omega) + i\epsilon_2(\omega)$ can be measured experimentally via reflectivity characterization and hence, the complex refractive index $\tilde{n}(\omega) = n(\omega) + i\kappa(\omega)$ of the medium can be derived from $\tilde{n} = \sqrt{\epsilon}$. This yields

$$\epsilon_1 = n^2 - \kappa^2 \tag{2.10a}$$

$$\epsilon_2 = 2n\kappa \tag{2.10b}$$

$$n^2 = \frac{\epsilon_1}{2} + \frac{1}{2}\sqrt{\epsilon_1^2 + \epsilon_2^2} \tag{2.10c}$$

$$\kappa = \frac{\epsilon_2}{2n}. \tag{2.10d}$$

κ is the extinction coefficient and determines the optical absorption of electromagnetic waves propagating through the medium and is linked to the absorption coefficient α of Beer's law, which describes the exponential attenuation of the intensity of a light beam propagating through the medium ($I(x) = I_0 e^{-\alpha x}$), by the relation

$$\alpha(\omega) = \frac{2\kappa(\omega)\omega}{c}, \tag{2.11}$$

where $c = \frac{1}{\sqrt{\epsilon_0\mu_0}}$ is the speed of light in vacuum. Therefore, the imaginary part ϵ_2 of the dielectric function determines the absorption inside the medium. For

$|\epsilon_1| \gg |\epsilon_2|$, the real part of n, which quantifies the amount of lowering of the propagating wave's phase velocity due to polarization of the material, is determined mainly by ϵ_1.

2.2 The dielectric function of the free electron gas (Drude model)

Metals can be defined as either having overlapping valence and conduction bands or having partially filled conduction bands. In either case, the electrons are able to move around the lattice relatively freely and in the simplest electronic model of metals, the positive ions are ignored while the electrons are treated as a virtual free electron gas. The optical properties of metals can then be explained by a plasma model over a wide frequency range, where a gas of free electrons of metal with number density n moves against a fixed background of positive ions while the overall system is kept macroscopically neutral. Due to the motion of electrons and the interactions between different electrons, the system exhibits fluctuation of the electron density at the microscopic level. The validity of this model extends to the ultraviolet for alkali metals, while for noble metals, interband transitions occur at visible frequencies, thus limiting this model. The plasma model does not take into account of the details of the lattice potential and electron-electron interactions; instead, it assumes that certain aspects of the band structure are incorporated into the effective optical mass m of each electron. Electrons oscillate when an electromagnetic field is applied and since electrons are fermions, they will interact and collide with each other so their motion is damped by collisions occurring with a characteristic collision frequency $\gamma = 1/\tau$, where τ is the relaxation time of the free electron gas, which at room temperature is on the order of 10^{-14}, giving $\gamma \approx 100\,\mathrm{THz}$.

The motion for an electron of the plasma with an external electric field $\mathbf{E}$ is:

$$m\dddot{\mathbf{x}} + m\gamma\ddot{\mathbf{x}} = -e\mathbf{E}. \tag{2.12}$$

If the external electric field has a harmonic time dependence $\mathbf{E}(t) = \mathbf{E}_0 e^{-i\omega t}$, then one particular solution that describes the oscillations of the electron is $\mathbf{x}(t) = \mathbf{x}_0 e^{-i\omega t}$. The complex amplitude $\mathbf{x}_0$ incorporates any phase shifts between the driving field and the response by

$$\mathbf{x}(t) = \frac{e}{m(\omega^2 + i\gamma\omega)}\mathbf{E}(t). \tag{2.13}$$

The displaced electrons affect the polarization via $\mathbf{P} = -ne\mathbf{x}$, and is explicitly rewritten as

$$\mathbf{P} = -\frac{ne^2}{m(\omega^2 + i\gamma\omega)}\mathbf{E}. \tag{2.14}$$

Inserting the above expression for $\mathbf{P}$ into equation (2.2a) yields

$$\mathbf{D} = \epsilon_0 \left(1 - \frac{\omega_\mathrm{p}^2}{\omega^2 + i\gamma\omega}\right)\mathbf{E}, \tag{2.15}$$

where $\omega_\mathrm{p}^2 = \frac{ne^2}{\epsilon_0 m}$ is the *plasma frequency* of the free electron gas. Now we finally arrive at the desired solution for the dielectric function of free electron gas:

$$\epsilon(\omega) = 1 - \frac{\omega_\mathrm{p}^2}{\omega^2 + i\gamma\omega}. \tag{2.16}$$

The real and imaginary components of this complex function $\epsilon(\omega) = \epsilon_1(\omega) + i\epsilon_2(\omega)$ are given by

$$\epsilon_1(\omega) = 1 - \frac{\omega_\mathrm{p}^2\tau^2}{1 + \omega^2\tau^2} \tag{2.17a}$$

$$\epsilon_2(\omega) = \frac{\omega_\mathrm{p}^2\tau}{\omega(1 + \omega^2\tau^2)}, \tag{2.17b}$$

where $\gamma = 1/\tau$. For different frequency regions, the dielectric function in (2.16) behaves differently with respect to the collision frequency γ. We will limit our attention to frequencies $\omega < \omega_\mathrm{p}$, where metals maintain their metallic character. For large frequencies close to ω_p, the product $\omega\tau \gg 1$ leads to negligible damping, leaving $\epsilon(\omega)$ as mostly real. The dielectric function of the undamped free electron plasma is then given by

$$\epsilon(\omega) = 1 - \frac{\omega_\mathrm{p}^2}{\omega^2}. \tag{2.18}$$

One caveat is that the behavior of noble metals (such as gold and silver) in this region is altered by interband transistions which increases the magnitude of ϵ_2.

For the second regime of very low frequencies, where $\omega \ll \tau^{-1}$, $\epsilon_2 \gg \epsilon_1$ and the real and imaginary parts of refractive index are of comparable magnitude with

$$n \approx k = \sqrt{\frac{\epsilon_2}{2}} = \sqrt{\frac{\tau\omega_{\mathrm{p}}^2}{2\omega}}. \tag{2.19}$$

Metals are highly absorptive in this region, with the absorption coefficient

$$\alpha = \left(\frac{2\omega_{\mathrm{p}}^2\tau\omega}{c^2}\right)^{1/2}. \tag{2.20}$$

Defining the dc conductivity as $\alpha_0 = \frac{ne^2\tau}{m} = \omega_{\mathrm{p}}^2\tau\epsilon_0$, this expression becomes

$$\alpha = \sqrt{2\alpha_0\omega\mu_0}. \tag{2.21}$$

Using Beer's law of absorption for low frequencies, the fields decay inside the metal as $e^{-z/\delta}$, where δ is the skin depth defined as

$$\delta = \frac{2}{\alpha} = \frac{c}{\kappa\omega} = \sqrt{\frac{2}{\alpha_0\omega\mu_0}}. \tag{2.22}$$

This description is valid at low-frequency as long as the mean free path of the electrons $l = v_{\mathrm{F}}\tau \ll \delta$, where v_{F} is the Fermi velocity [25]. At room temperature, $l \approx 10\,\mathrm{nm}$ and $\delta \approx 100\,\mathrm{nm}$ for typical metals, thus justifying the use of the free-electron model.

At higher frequencies ($1 \leq \omega\tau \leq \omega_{\mathrm{p}}\tau$), the complex refractive index is mostly imaginary and σ becomes more and more complex, blurring the boundary between free and bound charges.

Up until now, we have only dealt with ideal free-electron metal; now we will contrast this with an example of a real metal that's important in the field of plasmonics. In the free-electron model, $\epsilon \to 1$ for $\omega \gg \omega_{\mathrm{p}}$. However, for noble metals, such as Au, Ag, Cu, a modification is needed in the region for $\omega > \omega_{\mathrm{p}}$ (where the response is dominated by free s electrons), since the filled d band close to the Fermi surfaces induce high polarization. This residual polarization is due to the positive background of the ion cores and can be described by adding the term $\mathbf{P}_\infty = \epsilon_0(\epsilon_\infty - 1)\mathbf{E}$ to (2.2a), where $\mathbf{P}$ is now the polarization (2.14) due to only free electrons. Equivalently, we can define the dielectric constant ϵ_∞, which

includes the contribution of the bound electrons to the polarizabillity, (typically $1 \leq \epsilon_\infty \leq 10$) and rewrite the dielectric function of the free-electron model (also known as the Drude model, named after Paul Drude in 1900 [2]) as

$$\epsilon(\omega) = \epsilon_\infty - \frac{\omega_\mathrm{p}^2}{\omega^2 + i\gamma\omega}. \tag{2.23}$$

2.2.1 The dispersion of free electron gas

Now, we will focus our attention on the transparency regime $\omega > \omega_\mathrm{p}$ of the free electron gas model. To start, we will examine the traveling-wave solutions of Maxwell's equations in the absence of external stimuli. Combining (2.1c) and (2.1d) leads to the wave equation

$$\nabla \times \nabla \times \mathbf{E} = -\mu_0 \frac{\partial^2 \mathbf{D}}{\partial^2 t} \tag{2.24a}$$

$$\mathbf{K}(\mathbf{K} \cdot \mathbf{E}) - K^2 \mathbf{E} = \epsilon(\mathbf{K}, \omega) \frac{\omega^2}{c^2} \mathbf{E}, \tag{2.24b}$$

in the time and Fourier domains, respectively. There are two solutions depending on the polarization direction of the electric field vector. For transverse waves, $\mathbf{K} \cdot \mathbf{E} = 0$, the solution will be the generic dispersion relation [23]

$$K^2 = \epsilon(\mathbf{K}, \omega) \frac{\omega^2}{c^2}. \tag{2.25}$$

For longitudinal waves to satisfy (2.24b) requires

$$\epsilon(\mathbf{K}, \omega) = 0, \tag{2.26}$$

which implies that longitudinal collective oscillations can only occur at frequencies corresponding to zeros of $\epsilon(\omega)$ and we have assumed that all electrons move in phase.

Inserting equation (2.18) into (2.25), the dispersion relation of the traveling waves becomes

$$\omega^2 = \omega_\mathrm{p}^2 + K^2 c^2. \tag{2.27}$$

This relation is plotted in Figure 2.1 for a generic free electron metal. For $\omega < \omega_\mathrm{p}$, the propagation of the transverse EM waves is forbidden inside the metal plasma.

However, for $\omega > \omega_p$, the plasma supports transverse waves propagating with a group velocity $v_g = d\omega/dK < c$. The significance of the plasma frequency is that in the limit of small damping, $\epsilon(\omega_p) = 0$ (for $\mathbf{K} = 0$), corresponding to the longitudinal mode, as discussed above. In this case, $\mathbf{D} = 0 = \epsilon_0\mathbf{E} + \mathbf{P}$. Then, the electric field is a pure depolarization field with $\mathbf{E} = -\mathbf{P}/\epsilon_0$. The dispersion can be measured in inelastic scattering experiments such as electron energy loss spectroscopy (EELS).

Physically, the plasma frequency ω_p can be thought of as the natural frequency of a free oscillation of the electron gas. The quanta of these charge oscillations are refer to *plasmons* (or volume plasmons to distinguish them from surface and localized plasmons). Now, because of its longitudinal nature, volume plasmons do not couple to transverse EM waves, and can only be excited by direct particle impact. The plasma frequency of metals is typically determined by electron loss spectroscopy experiments, where electrons are passed through thin metallic foils, and is typically in the ultraviolet regime with $\omega_p \sim 5 - 15\,\text{eV}$, depending on the band structure [26].

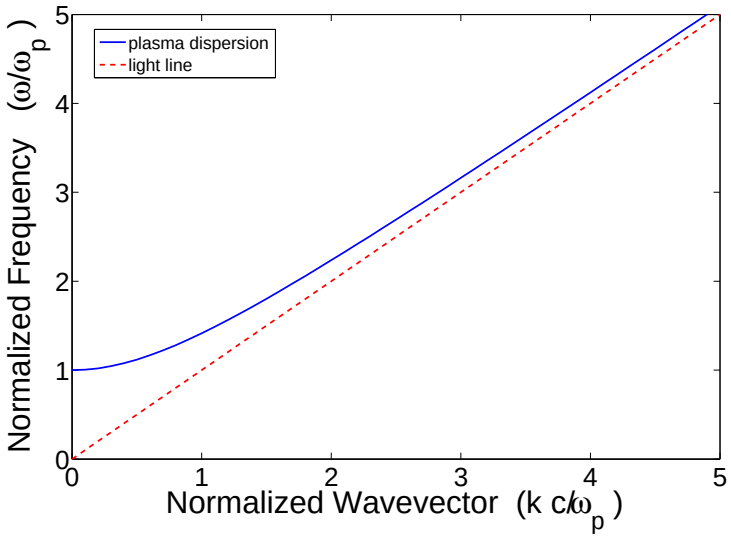

Figure 2.1: The normalized dispersion relation of the free electron gas. Electromagnetic wave propagation is only allowed for $\omega > \omega_p$. The light line is shown as a reference.

2.2.2 Modifications for real metals and interband transitions

The agreement between equation (2.23) and experimental data obtained by Johnson and Christy [27] for gold and silver (two important metals in plasmonics in the visible and near-infrared) is good until interband transitions become more prominent at visible and higher frequencies (leading to an increase in ϵ_2), at which point the validity of the expression starts to fail. Interband transitions occur when electrons from the filled band below the Fermi surface are excited to higher bands. As a result, higher damping and competition between the two excitations result at visible frequencies. To fix this, a modification is added to (2.12) to become

$$m\dddot{\mathbf{x}} + m\gamma\ddot{\mathbf{x}} + m\omega_0^2\mathbf{x} = -e\mathbf{E}. \tag{2.28}$$

Now interband transitions are accounted for using the classical framework of a bound electron with resonance frequency ω_0, and (2.28) can then be used to calculate the polarization as derived previously. A Lorentz-oscillator term of the form $\frac{A_i}{\omega_i^2-\omega^2-i\gamma_i\omega}$ is added to the free-electron derivation in (2.16) [28].

2.2.3 Gold—metal of choice for biosensing

Gold has immerged as the metal of choice for almost all optical biological sensing applications not only because of its plasmonic properties, but also because the surface chemistry of gold makes it relatively easy to establish sulfur bonds between gold atoms and organic molecules. Since gold's plasmonic properties are only prominent in the visible and near-infrared regimes, these biological applications are only limited to these regimes. Although silver offers better local field enhancement, it is not used as often since it oxides naturally without additional processing steps.

2.3 Surface plasmon polaritons

Surface plasmon[4] polaritons[5] (SPPs) are transverse magnetic (TM) electromagnetic wave propagating along the interface between a metal and a dielectric. The coupling of the EM waves to the oscillations of the metal's electron plasma produce these electromagnetic surface waves. Thus, SPPs have a combined EM wave and surface charge characteristic. Since these are TM waves, the generation of surface charge requires the electric field to be normal to the surface, leading to fields being enhanced near the surface, which is then sensitive to perturbations such as biomolecular bindings (as we will discuss in Chapter 3 and Chapter 4). The fields decay exponentially away from the surface and are call evanescent fields, which prevent power from propagating away from the surface.

2.3.1 The wave equation

The equations governing SPPs can be derived from Maxwell's equations (2.1). We will not show the full derivation here but interested readers can consult an electromagnetic textbook [29]. Instead, we will begin at an intermediate step, that of the wave equation

$$\frac{\partial^2 \mathbf{E}(z)}{\partial z^2} + (k_0^2\epsilon - \beta^2)\mathbf{E} = 0. \tag{2.29a}$$

$$\frac{\partial^2 \mathbf{H}(z)}{\partial z^2} + (k_0^2\epsilon - \beta^2)\mathbf{H} = 0, \tag{2.29b}$$

where β is the propagation constant.

For TM modes, it could be shown that the governing equations become

$$E_x = -i\frac{1}{\omega\epsilon_0\epsilon}\frac{\partial H_y}{\partial z} \tag{2.30a}$$

$$E_z = -\frac{\beta}{\omega\epsilon_0\epsilon}H_y. \tag{2.30b}$$

[4] In quantum mechanic theory, plasmon are quasiparticles that result from quantization of plasma oscillations interacting with a photon.

[5] In physics, polaritons are quasiparticles that results from coupling of electromagnetic waves with an electric or magnetic dipole excitations, such as the mixing of a photon with an excitation of a material. Besides SPPs, there are also phonon polaritons and exciton polaritons.

Analogously, for TE modes, the equations become

$$H_x = i\frac{1}{\omega\mu_0}\frac{\partial E_y}{\partial z} \tag{2.31a}$$

$$H_z = \frac{\beta}{\omega\mu_0}E_y. \tag{2.31b}$$

2.3.2 Surface plasmon polaritons at an interface

As was mentioned earlier, SPPs exist at the interface between a dielectric (with a real dielectric constant ϵ_2 for the infinite half space $z > 0$) and a metal (with a dielectric function $\epsilon_1(\omega)$ for the infinite half space $z < 0$), as shown in Figure 2.2. With the second medium being a metal, it implies that $\mathrm{Re}[\epsilon_1] < 0$, which occurs at frequencies below the bulk plasmon frequency ω_p (or conversely at wavelengths above the bulk plasmon wavelength). We will now derive the solutions confined to the interface with evanescent decay in the perpendicular z-direction, as pictorially depicted in the figure. The charge oscillation in the metal is also illustrated. Shown on the right of the figure is a finite element method (FEM) simulation result of SPPs implemented using COMSOL Multiphysics.

For TM modes, using (2.30) in both half spaces above and below the interface yield

$$H_y(z) = A_2 e^{i\beta x}e^{-k_2 z} \tag{2.32a}$$

$$E_x(z) = -iA_2\frac{1}{\omega\epsilon_0\epsilon_2}k_2 e^{i\beta x}e^{-k_2 z} \tag{2.32b}$$

$$E_z(z) = -A_2\frac{\beta}{\omega\epsilon_0\epsilon_2}e^{i\beta x}e^{-k_2 z}, \tag{2.32c}$$

for $z > 0$ and

$$H_y(z) = A_1 e^{i\beta x}e^{k_1 z} \tag{2.33a}$$

$$E_x(z) = iA_1\frac{1}{\omega\epsilon_0\epsilon_1}k_1 e^{i\beta x}e^{k_1 z} \tag{2.33b}$$

$$E_z(z) = -A_1\frac{\beta}{\omega\epsilon_0\epsilon_1}e^{i\beta x}e^{k_1 z}, \tag{2.33c}$$

for $z < 0$. $k_i \equiv k_{z,i}(i = 1, 2)$ is the wave vector component that's perpendicular to the interface in the two media. The reciprocal ($\delta = 1/|k_z|$) defines the evanescent

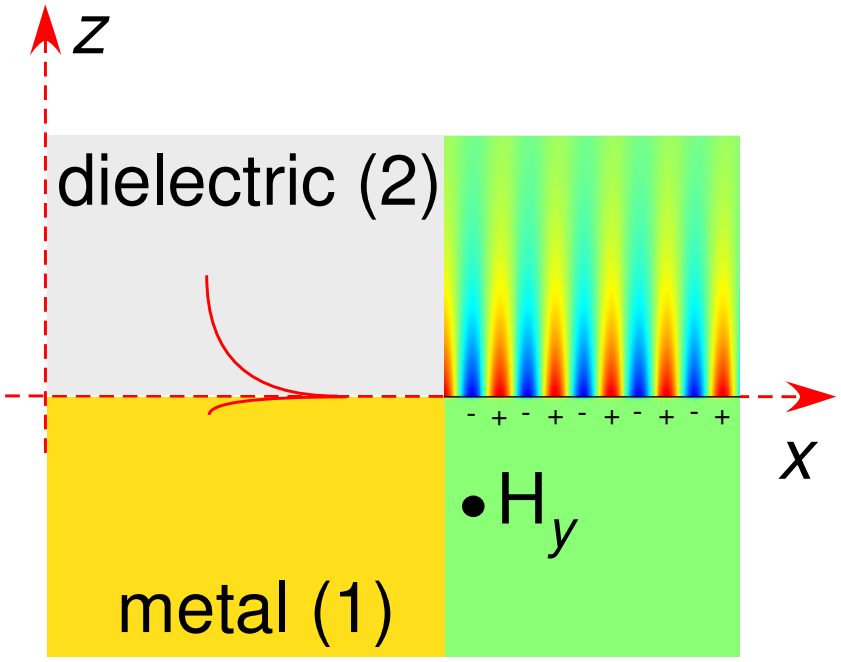

Figure 2.2: Schematic of a dielectric and metal interface that supports propagating SPPs is shown along with the evanescent decaying fields. Finite element method (FEM) simulation of the SPP fields is also shown.

decay length of the field that's perpendicular to the interface and is a measure of the field confinement. In order to satisfy the boundary condition of continuity of H_y and $\epsilon_i E_z$ at the interface requires the field amplitudes $A_1 = A_2$ and

$$\frac{k_2}{k_1} = -\frac{\epsilon_2}{\epsilon_1}. \tag{2.34}$$

With the sign convention of the exponents in (2.32) and (2.33), the requirement of confinement to the surface at the interface dictates that $\mathrm{Re}[\epsilon_1] < 0$ if $\epsilon_2 > 0$; therefore, surface waves only exist at the interface between media with opposite signs of the real part of their dielectric permittivities, i.e., between a conductor and an insulator. In addition, equation (2.32a) for H_y has to satisfy the scalar form of the wave equation (2.29b), yielding

$$k_1^2 = \beta^2 - k_0^2 \epsilon_1 \tag{2.35a}$$

$$k_2^2 = \beta^2 - k_0^2 \epsilon_2. \tag{2.35b}$$

By combining (2.34) and (2.35), the important result of the dispersion relation of propagating SPPs is shown [30]

$$\beta = k_0 \sqrt{\frac{\epsilon_1 \epsilon_2}{\epsilon_1 + \epsilon_2}}. \tag{2.36}$$

If we assume a real metal with a complex dielectric function $\epsilon_1 = \epsilon_1' + i\epsilon_1''$, then we obtain a complex $\beta = \beta' + i\beta''$, where

$$\beta' = \frac{\omega}{c} \left(\frac{\epsilon_1' \epsilon_2}{\epsilon_1' + \epsilon_2} \right)^{1/2} \tag{2.37a}$$

$$\beta'' = \frac{\omega}{c} \left(\frac{\epsilon_1' \epsilon_2}{\epsilon_1' + \epsilon_2} \right)^{3/2} \frac{\epsilon_1''}{2(\epsilon_1')^2}. \tag{2.37b}$$

The imaginary component, β'', characterizes the propagation loss of SPPs along the interface with a characteristic propagation length define as $L_{\text{spp}} = 1/(2\beta'')$. This propagation length results from the non-zero imaginary part of the metal dielectric constant.

No TE mode can satisfy the condition of $A_1(k_1 + k_2) = 0$, resulting from the continuity boundary condition of E_y and H_x and derived in a fashion similar to the TM case, starting with (2.31). Therefore, propagating surface plasmon polaritons can *only exist for TM polarization*.

Now, we will look closely at the dispersion equation (2.36) as shown in Figure 2.3 for a metal with negligible damping ($\text{Im}[\epsilon_1] = 0$) as described by the real part of the Drude model (2.18) for both an air ($\epsilon_2 = 1$) and fused silica ($\epsilon_2 = 2.25$) interface. The ordinate in the plot has been normalized with respect to the plasma frequency ω_{p}. The real part of the propagation wave vector β are plotted, as well as the light lines of air and fused silica. Notice that the SPP excitation curves lie to the right of the light lines ($\omega = ck_{\text{n}}$) due to their bound nature. Thus, phase matching condition would need to be met in order for light to couple to the SPP modes. Phase matching condition could be achieved using a prism, grating, or two-dimensional nanohole array (this will be discuss in the next section). Radiation into metal occurs in the transparency regime when $\omega > \omega_{\text{p}}$ (not shown in the figure). A forbidden band gap region exists between the bound and radiative state where the purely imaginary β prohibits propagation.

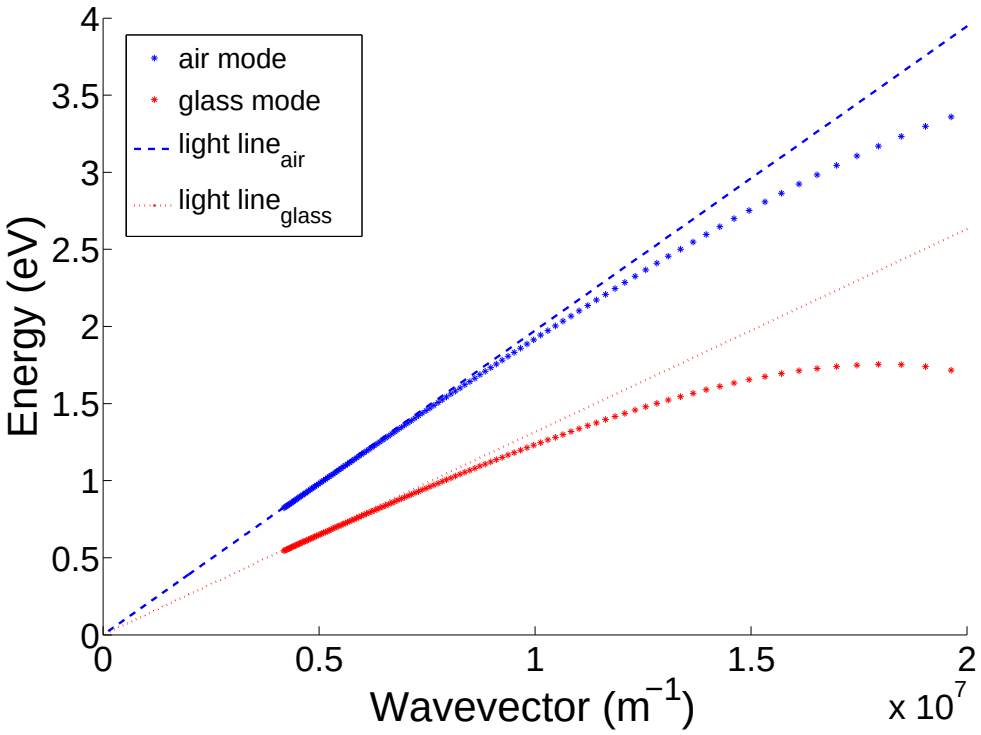

Figure 2.3: Dispersion relations of gold using the Drude model at the interface of air and BK7 glass. The respective light lines are also shown. There is a momentum mismatch between the light line and the respective SPP mode at any particular energy.

As seen in the figure, for small wave vector, the SPP propagation constant is close to k_0 at the light line and the waves propagate many wavelengths into the dielectric space. In the other extreme of large wave vectors, the frequency of the SPPs approaches the *surface plasmon frequency*, derived by inserting the free-electron dielectric function (2.16) into (2.36) to yield

$$\omega_{\mathrm{sp}} = \frac{\omega_{\mathrm{p}}}{\sqrt{1+\epsilon_2}}. \tag{2.38}$$

In the limit of negligible damping of the conduction electron oscillation (i.e., $\mathrm{Im}[\epsilon_1(\omega)] = 0$), β goes to infinity as the frequency approaches ω_{sp} and the group velocity $v_{\mathrm{g}} \to 0$. This mode acquires electrostatic characteristics and is called *surface plasmon*.

For the case of real metal with free-electron and interband damping, the propagating SPPs are damped with a propagation length typically between 10

and 100 µm in the visible spectrum depending on the material configuration. The bound SPPs now approach a finite, maximum wave vector β at the surface plasmon frequency. This finite β places a lower limit on both the wavelength $\lambda_{\mathrm{sp}} = 2\pi/\mathrm{Re}[\beta]$ of the surface plasmon and the degree of mode confinement at the interface since the field in the dielectric decays as $e^{-|k_z||z|}$ with $k_z = \sqrt{\beta^2 - \epsilon_2(\frac{\omega}{c})^2}$. Furthermore, now there is no bandgap region. Instead, transitions are allowed between ω_{sp} and ω_{p} in this quasibound, leaky state. For frequencies close to ω_{sp}, SPPs exhibit large field confinement at the interface and consequently, a small propagation distance into the dielectric due to increased damping. In plasmonics, this trade-off between localization and loss is inherent.

The high confinement of SPPs can occur as long as the fields oscillate at frequencies close to the intrinsic plasma frequencies of the metal and is limited to the visible and IR regimes for silver and gold. At lower frequencies, from the SPP dispersion relation, the confinement to the interface is no longer true as the propagation constant β decreases and approaches toward the wave vector of the dielectric. The SPPs then evolve into grazing light fields, extending many wavelengths distance into the dielectric above the interface as the frequency is lowered and propagate along the interface with the same phase velocity as unbound radiation. This occurs because at lower frequencies, the field penetration into the metal is smaller due to large (negative) real part and (positive) imaginary part of ϵ. Subsequently, the non-zero component of the electric field parallel to the surface that is essential to establish an oscillating spatial charge distribution in the metal starts to vanish and SPPs disappear in the limit of a perfect electric conductor.

In the metal itself, the decay length δ_{m} is around 20 nm over a wide frequency range from the visible to the infrared. The field confinement below the diffraction limit of half the wavelength in the dielectric is possible close to ω_{sp}. To summarize, field confinement is achieved since the propagation constant β is larger than the wave vector k in the dielectric, resulting in evanescent decay on both sides of the interface.

2.3.3 Excitations of SPP waves

As we have seen, SPPs cannot be excited at a metal/dielectric interface with only an incident EM field due to a momentum mismatch. There are several methods to excite SPP waves. In the 1950's, researchers used bombarding electrons to penetrate the metal to transfer momentum $\hbar q$ and energy ΔE_0 to the conduction electrons of the metal [31, 32]. The energy loss from the scattered electrons corresponds to the energy of the excited SPP waves. However, it is not convenient to access the small wave vectors with electrons since the aperture of the electron beam cannot be reduced sufficiently. More direct coupling with incident light beam had since been discovered.

Prism coupling

As was mentioned earlier, SPPs on a flat interface between a metal and a dielectric cannot be directly excited by light since $\beta > k$, where k is the wave vector of light on the dielectric side of the interface. Suppose the incident beam impinges with an angle θ with respect to the surface normal, then the projection of the wave vector along the interface is given by $k_x = k \sin\theta$, which is always less than β, even at grazing incidence. Another mechanism is needed to overcome this momentum mismatch. This can be achieved using either the Kretschmann-Raether [33] or Otto configuration [34], where attenuated total internal reflection inside a prism is used to couple to SPPs. Here, the prism configuration can be thought of as a three-layer system consisting of a thin metal film sandwiched between two dielectric layers (for the Kretschmann configuration), in which one of the dielectric layer is taken to be air. The incident beam is reflected from the interface between the dielectric of higher dielectric constant ϵ and the metal and will have an in-plane momentum of $k_x = k_0\sqrt{\epsilon}\, sin\theta$. While this momentum is insufficient to excite SPPs on the interface of the metal and the prism, but if the metal film on top of the prism is sufficiently thin, electromagnetic fields can evanescently couple to the surface mode on the other side of the metal interface (i.e., metal/air) and excite SPPs

when the incident angle satisfies the phase matching condition given by

$$k_x = k_0\sqrt{\epsilon}\, sin\theta = k_0 \left(\frac{\epsilon_1\epsilon_2}{\epsilon_1+\epsilon_2}\right)^{1/2} = k_{\text{spp}} \tag{2.39}$$

Now, SPPs with propagation constants β between the light lines of air and the higher-index dielectric prism can be excited. When this phase matching condition occurs, it manifests itself as a minimum dip in the reflected beam. Note that phase matching condition is still *not* achieved at the metal/prism interface. The SPPs excited using prism coupling process are leaky waves in that they lose energy not only to the inherent absorption inside the metal, but also to leakage of radiation into the prism with the excited propagation constants lying within the prism light cone. The reflection dip is a manifestation of the destructive interference between this radiation leakage and the reflected excitation beam [23].

Grating coupling

The phase matching condition can also be met by fabricating metal surfaces with shallow (20 nm or less) grating of grooves with a periodicity of Λ. Phase matching is then achieved whenever $\beta = k_x = k_0\, sin\theta \pm mK_g$ is met, where $K_g = 2\pi/a$ is the reciprocal vector of the grating and $m = 1, 2, 3\ldots$ [35]. That is, an integer number of the grating vectors, K_g, is added or subtracted from the projection of the incident wave vector. When phase matching is met so that the SPP dispersion relation, $k_{\text{spp}} = k_x$, excitation of SPPs is manifested by a dip in the reflectance, similar to prism coupling. For 1-D grating, if the depths are larger, then localized modes inside the grooves would lead to significant changes to the SPP dispersion. Distortions of the first higher-order band would fold back at a Brillouin zone boundary and enable coupling even for short pitches less than $\lambda/2$ with normal light incidence due to the lowering of the frequency of the modified SPP dispersion relation [36].

The grating coupling can be easily extended to the case of two-dimensional (2-D) nanohole array, Figure 2.4, offering more freedom in manipulating the SPPs. The phase matching condition now becomes

$$k_{\text{spp}} = k_{\parallel} \pm mK_g^x \pm nK_g^y, \tag{2.40}$$

where $k_{\parallel}$ is the in-plane component of the incident wave vector, K_g^x and K_g^y are the grating vectors in the x- and y-directions, respectively, and m and n are integers representing the diffraction order. The in-plane vector $k_{\parallel}$ is expressed as

$$k_{\parallel} = k_x + k_y = k_0(\hat{x}\, sin\theta\, cos\phi + \hat{y}\, sin\theta\, sin\phi), \tag{2.41}$$

for a square lattice structure.

The excitation of SPPs on metallic 2-D nanohole array induces enhanced optical transmission when the size of the holes is sub-wavelength [4]. This discovery as well as other resonant phenomena have been important in the field of plasmonics that have led to applications in numerous areas [37–40]. Nanohole array excitation of SPPs will be discussed more extensively in Chapter 3.

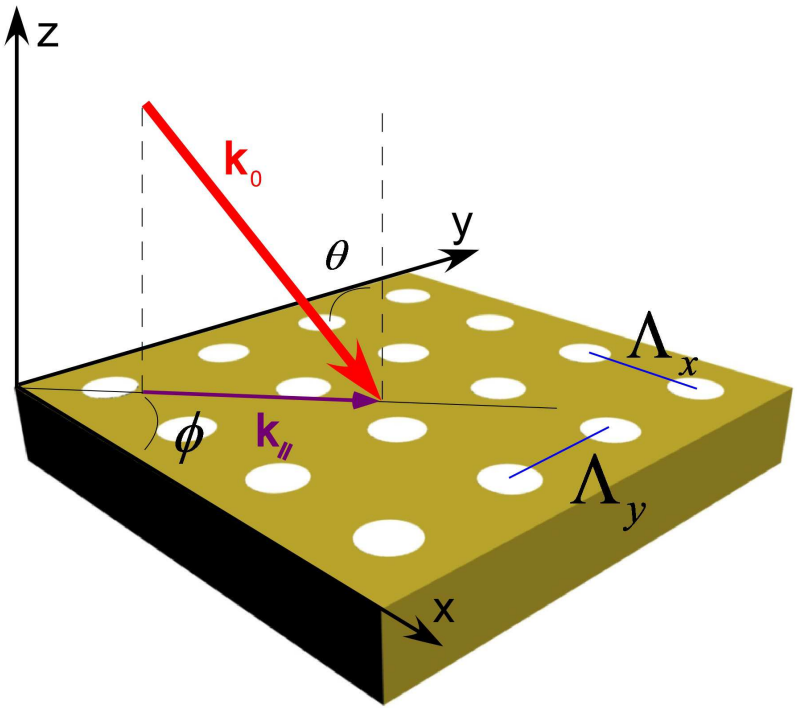

Figure 2.4: Schematic of two-dimensional sub-wavelength nanohole array to provide additional grating vectors for phase matching to excite SPPs.

The majority of surface plasmon biological sensing has been based on the interrogation of propagating SPP waves at the interface of metal/air interface. By using surface functionalization techniques, specific binding event can be analyzed

via wavelength or angular-interrogation due to the change in the refractive index. A more detailed discussion on the sensitivities of each interrogation method can be found in Ref. [41]. We will use surface functionalization techniques on our device to evaluate the sensitivity of protein binding in Chapter 4.

Other excitation methods

A variant of the prism coupling method is to use a microscopy objective with a high numerical aperture to provide a large angular bandwidth with a cone of focused beam to induce SPP excitation with a corresponding excitation angle of $\theta_{\text{spp}} = \arcsin(\beta/nk_0) > \theta_{\text{c}}$, where θ_{c} is the critical angle of total internal reflection at the substrate/air interface [42].

In addition, SPPs can also be excited on roughened surfaces or fabricated localized scatterers. Phase matching is then provided by the momentum components of Δk_x resulting from scattering, so that the phase matching condition becomes $\beta = k\,sin\,\theta \pm \Delta k_x$. However, the random surface roughness also contributes additional loss for SPP propagation via coupling to radiation and the coupling efficiency is lower than with either prism or grating coupling. Besides macroscopic coupling, another form of coupling is to use a near-field scanning optical microscope (NSOM) probe for the *local* excitation of SPPs over an area $a \ll \lambda_0$ to act as a single point source excitation of SPPs [43].

2.4 Localized surface plasmon

The second fundamental form of plasmonic excitation is localized surface plasmons (LSPs), which are non-propagating excitations of the electron charge oscillations of metallic nanostructure. These modes result naturally from the scattering of sub-wavelength metallic nanoparticles in an oscillating electromagnetic field. The curved surface of the particle exerts a restoring force on the driven electrons so that a resonant mode can give rise to field amplification both inside and on the surface of the outside of the particle. These localized surface plasmon (or sometimes for short, localized plasmon) resonances can be directly excited by light

unlike SPPs due to their curved (or structured) surfaces [44, 45]. For gold and silver nanoparticles, the LSP resonance falls within the visible spectrum regime and has been used for a few hundred years as evident by the bright colors exhibited by the stain glass windows of medieval churches and ornamental cups. These bright colors result from both transmitted and reflected light due to resonantly enhanced absorption and scattering.

The interaction of subwavelength partice of size d, where $d \ll \lambda$, with incident oscillating EM field can be discussed and analyzed with the simple quasi-static approximation when the size of the particle is much smaller than the wavelength of light in the medium. This situation allows the assumption of the EM field to be constant over the particle's volume so that electrostatic assumption is valid and simplifies the analysis of the problem. Once the field distribution solution is derived, the harmonic time dependence can then be added. This lowest-order approximation of the full scattering problem is valid for nanoparticle size less than 100 nm for most scenarios. As an illustrative example, we assume a homogeneous, isotropic sphere of radius a with a uniform static incident electric field $\mathbf{E} = E_0\mathbf{z}$ with an isotropic and nonabsorptive surrounding dielectric medium with ϵ_m. The incident EM field are parallel to z-direction at sufficient distance from the sphere. The dielectric function of the sphere is described by the complex ϵ_s. In the electrostatic approach, the solution can be derived from the Laplace equation. A detailed derivation can be found in Ref. [24]. It can be derived that the applied field will induce a dipole moment inside the sphere with a magnitude proportional to $|\mathbf{E}_0|$ and the dipole moment is given by

$$\mathbf{p} = 4\pi\epsilon_0\epsilon_m a^3 \frac{\epsilon_s - \epsilon_m}{\epsilon_s + 2\epsilon_m}\mathbf{E}_0, \tag{2.42}$$

where the polarizability α is

$$\alpha = 4\pi a^3 \frac{\epsilon_s - \epsilon_m}{\epsilon_s + 2\epsilon_m}. \tag{2.43}$$

The polarizability α is in resonance when the denominator term $|\epsilon_s + 2\epsilon_m|$ is at a minimum and occurs when

$$\mathrm{Re}[\epsilon_s(\omega)] = -2\epsilon_m, \tag{2.44}$$

for the case when $\mathrm{Im}[\epsilon_s]$ is small or slowly-varying. This condition is called the Fröhlich criterion and the resonant mode is called the dipole surface plasmon of the metal nanoparticle. For a Drude metal located in air, the Fröhlich criterion is met at the frequency $\omega_0 = \omega_\mathrm{p}/\sqrt{3}$ and is red-shifted as the medium dielectric ϵ_m increases. At resonance in α, the internal and dipolar electric field is also resonantly enhanced to

$$\mathbf{E}_\mathrm{in} = \frac{3\epsilon_m}{\epsilon_s + 2\epsilon_m}\mathbf{E}_0 \tag{2.45a}$$

$$\mathbf{E}_\mathrm{out} = \mathbf{E}_0 + \frac{3\mathbf{n}(\mathbf{n}\cdot\mathbf{p}) - \mathbf{p}}{4\pi\epsilon_0\epsilon_\mathrm{m}}\frac{1}{r^3}. \tag{2.45b}$$

It is this resonant local field enhancement (LFE) that has seen metallic nanoparticles used in optical devices, such as nanoparticle waveguide [46–48] and biological sensors [49–52].

As was mentioned previously, localized plasmon increases the efficiency of absorption and scattering of light. The corresponding cross sections for the absorption and scattering can be calculated via the Poynting vector to be [53]

$$C_{abs} = k\,\mathrm{Im}[\alpha] = 4\pi k a^3\,\mathrm{Im}\left[\frac{\epsilon_s - \epsilon_m}{\epsilon_s + 2\epsilon_m}\right] \tag{2.46a}$$

$$C_{scat} = \frac{k^4}{6\pi}|\alpha|^2 = \frac{8\pi}{3}k^4 a^6\left|\frac{\epsilon_s - \epsilon_m}{\epsilon_s + 2\epsilon_m}\right|^2. \tag{2.46b}$$

For small particle size with $a \ll \lambda$, the absorption efficiency dominates over the scattering efficiency as it scales with a^3. Once again, at the dipole plasmon resonance, the absorption and scattering (and extinction, which is the summation of the two) are resonantly enhanced when the Fröhlich condition is met. For larger particle size where the quasi-static approximation is no longer justified due to significant phase retardation effect of the incident field over the particle volume, the more rigorous electrodynamic approach is required. The Mie theory was developed [3] to expand the internal and scattered fields into a set of normal modes described by vector harmonics to complete the theory of the absorption and scattering of a sphere upon electromagnetic field interaction. The quasi-static solution described above can also be derived from Mie theory simply by retaining the first term of the power series expansion of the absorption and scattering coefficients. Details of the

Mie theory can be found in works such as [3, 53, 54]. Basically, inclusion of higher order terms will lead to occurrence of higher order resonances. Radiation damping results from the direct radiative decay of the coherent electron oscillation into photons and is the main culprit for weakening of the dipole plasmon resonance strength as the particle size increases [55]. A second damping process is non-radiative due to absorption resulting from the creation of electron-hole pairs via either intraband excitation within the conduction band or interband transistions from d bands to the sp conduction band for noble metallic particles [56]. The local field enhancement (LFE) and the resonance are highly dependent on the particle shape and size, as well as the surrounding medium.

2.4.1 Coupling between localized surface plasmons

When particles are close in vicinity, coupling between the localized plasmons of each will interact and modify its ensemble localized plasmon resonance. For small particles, these interactions are dipolar in nature so the particle ensemble can be treated as a collection of interacting dipoles to first order approximation. For example, for ordered, closely-spaced one-dimensional nanoparticle array, strong field localization in nano-shaped gaps between adjacent particles have been reported [57]. In this regime, where the interparticle spacing, $d \ll \lambda$, near-field interactions dominate with a distance dependency of $\frac{1}{d^3}$. Here, the particle size a is assumed to be much less than d so that dipolar approximation is valid. The field localization occurs due to a suppression of scattering into the far-field via excitation of the plasmon modes in particles along the chain axis. Besides interparticle plasmon coupling, intraparticle plasmon coupling of complex nanostructure is also utilized to increase the local field enhancement, such as the nanocrescent structure [58, 59]. We will return to this topic in Chapter 6. For larger particle spacing, far-field dipolar coupling dominates with a distance dependence of $1/d$ and greatly influences the plasmon lineshape both in terms of resonance wavelength and spectral width [60–62]. Lastly, an additional coupling mechanism is possible between localized surface plasmons and propagating SPPs. Metal nanoparticles fabricated

on metallic substrate can couple between these two types of plasmons [63]. We will further explore this type of coupling in the next chapter.

2.5 Surface-enhanced Raman scattering

Surface enhanced Raman spectroscopy or surface enhanced Raman scattering (SERS) was first discovered in 1977 [64, 65] and the large increase in Raman cross-section (and therefore Raman intensity) is attributed to surface plasmons [66]. Then, two decades later, single molecules detection was experimentally demonstrated by using chemically roughened surfaces with an enhancement factor of the scattering cross-section upto 10^{14} in the "hot spots" of the metal nanoparticle junctions arising from localized surface plasmon resonances [67,68]. Ever since, interests in SERS have increased dramatically because of its molecular fingerprint capability and its potential for single molecular detection.

2.5.1 What is Raman scattering?

When incident light are scattered from an atom of molecule, most of the photons are elastically scattered, called Rayleigh scattering, such that the scattered photons have the same kinetic energy and frequency as the incident photons. However a very small percentage (approximately 1 in 10 million photons) is scattered by another form of excitation, such that those scattered photons have a different frequency (inelastic scattering) from the incident photons. This process is called the Raman effect, first observed by Chandrasekhara Venkata Raman in 1928 [69], which describes the inelastic scattering process between a photon and a molecule and corresponds to the absorption and subsequent emission of a photon via an intermediate quantum state having a virtual energy level. The possible transitions are 1) no energy exchange between the incident photons and the molecules, i.e., no Raman effect; 2) energy exchange between the incident photons and the molecules, such that the energy difference is equal to the differences of the vibrational and rotational energy-levels of the molecule. Within the second scenario, it could further be separated into 2a) molecule absorbs energy (excitation of a vibrational mode)

from the incident photon, called Stokes scattering. The net photon energy is lower and generates a Stokes line that is red-shifted relative to the incident photon; 2b) molecule loses energy to the incident photon, called anti-Stokes scattering. The net photon energy is higher and generates an anti-Stokes line that is blue-shifted relative to the incident photon.

Unlike fluorescence, Raman transitions are much sharper, thus allowing for distinct molecular fingerprint of each molecule. In general, the photons involved in Raman transitions are non-resonant with the molecule and the excitation occurs in virtual levels. No absorption or emission of photons occurs, but rather the transition is purely a scattering process. This is also the case even when the incident photon is in resonance with an electron transition. Although this resonant Raman scattering is stronger than normal Raman scattering, the efficiency is still much weaker than those of fluorescent transitions. The typical Raman cross-sections σ_{RS} are between 10^{-31} cm^2/molecule and 10^{-29} cm^2/molecule, depending on whether the process is non-resonant or resonant, and is more than ten orders of magnitude smaller than those of fluorescence. Raman scattering is a spontaneous rather than stimulated scattering process and thus it is a linear process. The total power of the inelastic scattered photon scales linearly with the intensity of the incident light.

2.5.2 The electromagnetic theory of SERS

The electromagnetic theory used to explain the excitation of surface plasmons into enhancement factor increase of SERS can be found in Ref. [70]. The enhancement effect occurs by placing Raman-active molecules within the near-field of a metallic nanostructure that exhibits localized surface plasmons. Incident light can induce various excitations including interband transitions and for a nanostructure much smaller than the incident wavelength of light, only the dipolar plasmon is of significance. Free or almost free electrons can induce such excitation and the freer the electrons, the shaper and more intense the dipolar plasmon resonance. When the laser light is in resonant with the dipolar plasmon resonance, the metallic nanostructure will radiate light that is characteristic of the dipole radiation, which is a coherent process with the exciting field. It is characterized by a spatial

distribution of field magnitudes that reaches steady state only a few femtoseconds after the laser is on. The light intensity is highly concentrated near certain portion of the nanostructure while other areas are depleted. The nanostructure can be in the form of metal colloids, fabricated or self-assembled nanoparticle ensembles, or chemically roughened surfaces. The enhancement is due to two processes. The first results from a chemical or electronic contribution such that the Raman cross-section σ_{RS} is enhanced due to a change in the environment of the molecules so $\sigma_{\mathrm{SERS}} > \sigma_{\mathrm{RS}}$. From theoretical modeling, this chemical enhancement has a maximum contribution on the order of 100. The second, much more important contribution results from the increased local field enhancement (LFE) due to excitation of localized surface plasmons and the lightning rod effect [70]. Both the incident and emitted light fields are enhanced.

The electromagnetic enhancement can be expressed as

$$L(\nu) = \frac{|\mathbf{E}_{\mathrm{local}}(\nu)|}{|\mathbf{E}_0|}, \tag{2.47}$$

where $\mathbf{E}_{\mathrm{local}}$ is the local field at the Raman molecule. The total power of the Stokes beam is given by [23]

$$P_s(\nu_s) = N\sigma_{\mathrm{SERS}} L(\nu_L)^2 M(\nu_S)^2 I(\nu_L). \tag{2.48}$$

The difference in frequency between the incoming and scattered photons, ν_L and ν_S, respectively, is much smaller than the linewidth Γ of the localized surface plasmon; therefore, $|L(\nu_L)| \approx |L(\nu_S)|$. Now, the electromagnetic contribution to the SERS enhancement of the Stokes shift can strictly be written as [70, 71]

$$EF_{EM} = \frac{|\mathbf{E}_{\mathrm{loc}}|^4}{|\mathbf{E}_0|^4}. \tag{2.49}$$

So, the enhancement factor is strictly proportional to the local field to the fourth power. This enhancement as two physical bases: the first is from the resonant excitation of localized surface plasmons; the second is from the lightning rod effect [72, 73]. Only the former displays a strong frequency dependence while the latter is strictly due to the geometric sharpness that causes the field increase and the enhancement near sharp metallic features. The realization that localized surface

plasmons play such a major role in SERS enhancement has led researchers to fabricate nanostructures with tailored LSP in the forms of nanoparticle assemblies, roughen surfaces, and complex nanostructures, such as nanocrescent, nanorice, and nanovoid. We will investigate a variant of the nanocrescent, the nanotorch, in Chapter 6.

Chapter 3

Three-dimensional composite metallodielectric nanostructure for enhanced surface plasmon resonance sensing

In the preceding chapter, a primer to plasmonics was introduced. Now, we are prepared to delve into the applications of using the principles of plasmonics to solve real-world problems. As was mentioned, surface plasmon polaritons are confined to the interface between a metal and a dielectric interface and are sensitive to perturbation. As such, surface plasmon resonance (SPR) sensors utilize the properties of SPPs to detect minute changes in the refractive index of biochip due to biochemical bindings to the surface. They are useful since it's label-free and operate in real-time, while other techniques require fluorescent tags, which may affect the underlying binding events, involve additional processing steps, and are limited to detection of large molecules.

Although SPR sensors have been commercially available using prism coupling for sometime, now there has been an impetus to perform SPR sensing on hundreds or even thousands of active spots simultaneously using highly-parallel, two-dimensional nanohole array. In this chapter, a new three-dimensional mush-

roomlike metallodielectric nanostructure is introduced that shows improved characteristics for surface plasmon resonance sensing applications with an enhancement of the normal electric field compared to the conventional nanohole structure. A fabrication method is introduced to give controllable linewidth by an oblique metal deposition process. A sensor built with the composite nanostructure was then used to determine the hydrophilicity of its surface by monitoring the resonant wavelength shift and computing the corresponding adsorption thickness.

3.1 Introduction

Since the discovery of extraordinary transmission through sub-wavelength nanohole arrays [4], researchers have been exploring its applications in surface plasmon resonance sensing as an alternative to the prism-based Kretschmann-Raether configuration [33,74] and the diffraction grating approach [75–77], with special emphasis on high-throughput [78–82]. Recently, both the sensitivity [79, 82, 83] and the minimum resolution [84] in two-dimensional (2-D) nanohole array SPR sensors have improved significantly. To further increase sensitivity, researchers have also investigated coupling between localized surface plasmon resonances (LSPRs) and propagating surface plasmon polaritons (SPPs) of double-hole arrays [83], coaxial metallic arrays [85], and nanoholes with embedded nanoparticles [86]. In this chapter, we present a three-dimensional (3-D) composite mushroom-like metallodielectric nanostructure as an alternative approach for coupling these two types of plasmonic phenomena and exploit them for a wide range of practical applications.

3.2 3-D mushroomlike nanostructure

The proposed geometry is a layer of structured gold film on top of a perforated substrate, as shown in Figure 3.1. The size of the voids between the gold can be controlled independently of the underlying cylindrical perforations. When SPPs reflect between gold barriers, they interfere with each other and form localized standing waves [87]. Field localization also occurs near sharp apexes and

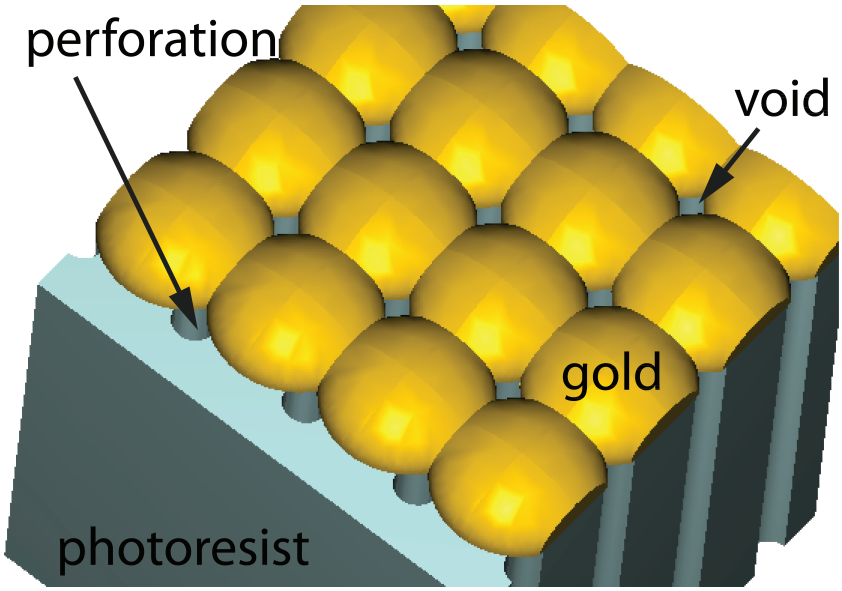

Figure 3.1: Schematic of the proposed structure utilizing coupling between LSPRs in the voids and SPPs on the gold surface.

the coupling between these two mechanisms is used to enhance the normal electric field. The LSPRs exist in the voids, while the SPPs exist on the gold surface.

3.3 Simulation

From the discussion of Chapter 2 on grating coupling of SPPs, phase matching can be achieved using 2-D nanohole array provided that the periodicity of the array is designed correctly. From the SPP dispersion relation for a 2-D nanohole structure with a periodicity of 1.2 µm and a laser center wavelength of 1.55 µm, the required plane-wave incidence angle to excite the (-1, 0) air-metal (AM) mode occurs at 17.3 °, as shown in Figure 3.2a. The first diffraction order is chosen because of its higher efficiency. Higher order modes are also shown as a reference, as well as for the case when the nanohole array is embedded in a water medium. Considering an incident beam illuminating the array from air at an angle of 17.3 °, rigorous coupled wave analysis (RCWA) was used to calculate the transmission in Figure 3.2b for an array with a periodicity of 1.20 µm, a gap size of 200 nm, and a gold film thickness of 100 nm. The experimental frequent-dependent dielectric

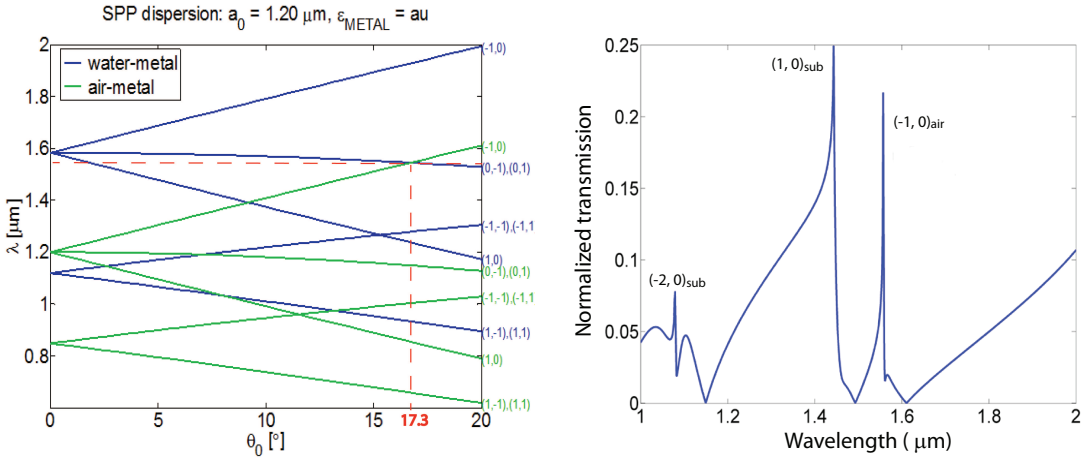

(a) (b)

Figure 3.2: (a) Phase matching conditions for a 2-D gold nanohole array with a periodicity of 1.2 µm with different diffraction orders are shown for both metal/air and metal/water interface. (b)Far-field RCWA simulation of nanohole array excited at 17.3 ° with a periodicity of 1.20 µm and a gap size of 200 nm using a gold thickness of 100 nm.

function of gold was used [27]. It can be clearly seen that the (-1, 0) AM mode can be excited around 1.55 µm, which matches well with the estimation from the dispersion relation. Figure 3.2b also reveals the excitation of substrate-metal modes with a substrate index of 1.5.

The near-field distribution of the electric fields at the SPP resonance was then simulated using finite element method (FEM) implemented with COMSOL Multiphysics. Figure 3.3a shows a unit cell of the 3-D model of the near-field distribution for the composite mushroomlike metallodielectric nanostructure. Periodicity boundary conditions are used to simulate a 2-D periodic array. The incident plane wave is in the $+x$-direction at an incidence angle of 17.3 ° in order to satisfy phase matching condition as discussed in Chapter 1. The perforation is embedded in a medium with a refractive index of 1.57 to simulate the photoresist material. Perfectly matched layer is used adjacent to the substrate to prevent non-physical reflection. The maximum electric field of the mushroomlike nanostructure in Figure 3.3a is 40% higher than conventional nanohole shown in Figure 3.3b without an underlying perforated photoresist layer.

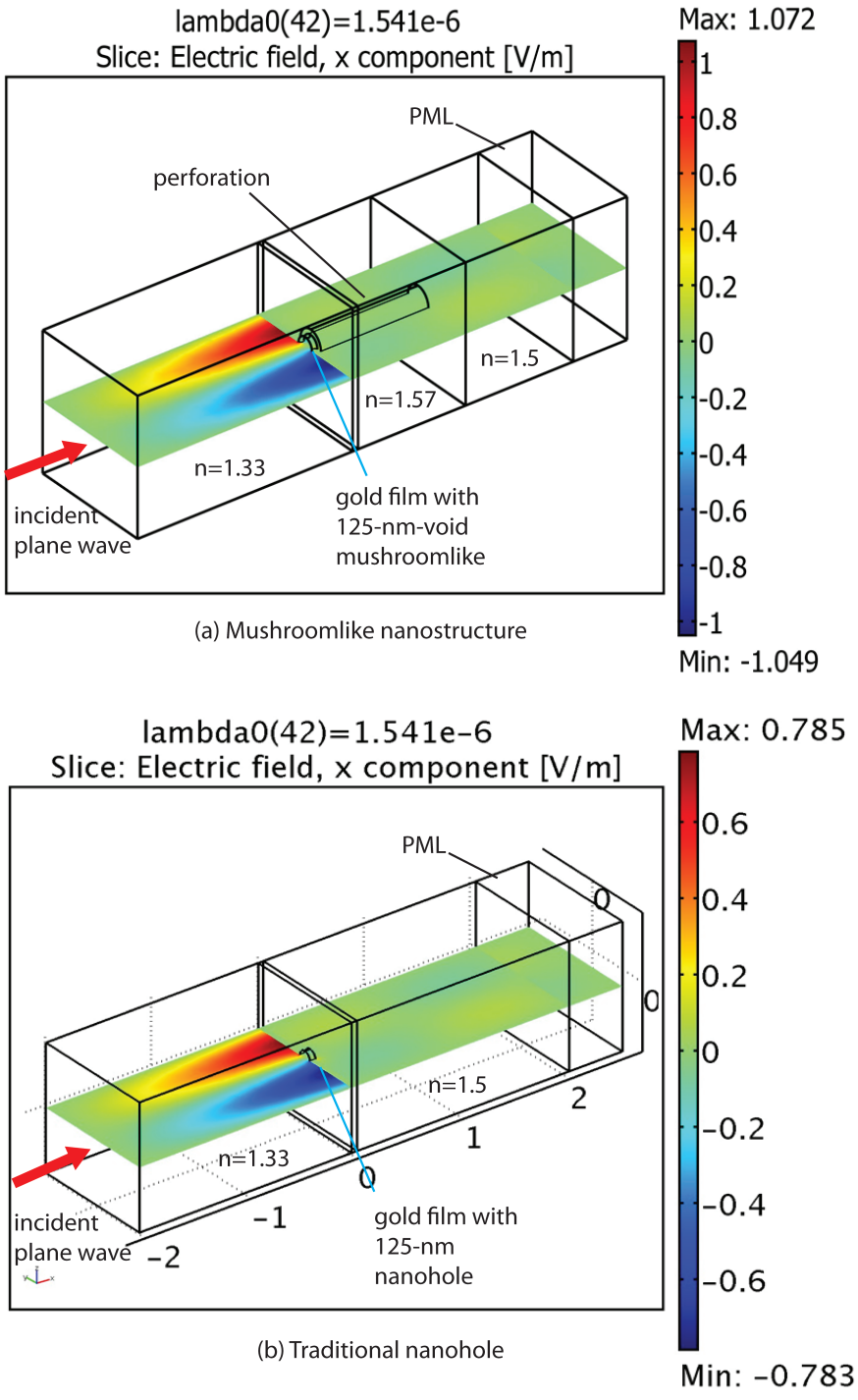

Figure 3.3: Unit-cell of 3-D FEM simulation of periodic (a) Mushroomlike nanostructure with 125-nm-void on top of SU8 perforation. (b) 125-nm nanohole using traditional fabrication method involving RIE etching process. Perfectly matched layer is used at the output to absorb non-physical reflections.

The field enhancement is due to coupling between the edges of the mushroom-like shape as well as localized and propagating plasmons. Furthermore, a 25-nm-thick subdomain integration of the normal electric field immediately above the gold material also reveals a factor of 1.4 enhancements for the mushroom composite nanostructure compared to the nanohole structure.

3.4 Fabrication

To fabricate these 3-D composite nanostructures over an area of more than $1\,\mathrm{cm}^2$, holographic lithography based on two-beam interferometry was used, as shown in Figure 3.4. A standard microscope glass substrate was cleaved and divided into four smaller pieces and then cleaned using piranha solution at $300\,^{\circ}\mathrm{C}$ for an hour. An antireflection coating (WiDE-15B, Brewer Science) was then spun at 3000 rpm for 30 s onto the substrate and baked for 30 min at $185\,^{\circ}\mathrm{C}$. SU8-2002 photoresist (from MicroChem) was spun at 3000 rpm for 30 s and baked for 20 min in an oven at $95\,^{\circ}\mathrm{C}$. The nanohole pattern was then exposed using two-beam interferometric holographic lithography technique. A continuous wave (CW) Argon ion laser (Innova 300, Coherent Corp.) with an output wavelength of 364 nm and an average power of approximately 40 mW is first expanded and spatially filtered to obtain a large, good-quality beam [88]. The beam is split into two optical paths in a Mach-Zehnder interferometric setup with a beamsplitter, BS. Two mirrors, M1 and M2, redirect the beams onto the photoresist-coated sample, which is mounted on a stage that can be rotated, tilted, or moved longitudinally. A LabVIEW program controls an aperture shutter that blanks the beam to control the exposure time and changes the angles of the mirrors and the sample stage, as well as the tilt and rotation of the stage. The periodicity of the nanohole is defined by $\lambda/(2\sin\alpha)$. The two interfering beams will form a 1-D grating after the first exposure, Figure 3.5a. To create a 2-D grating, the sample is then tilted $90\,^{\circ}$ before the second exposure of equal amount of time. The resulting sinusoidal intensity pattern is shown in Figure 3.5b and after performing post exposure bake (PEB) and developing the SU8 negative photoresist, a large-area, 2-D nanohole array is

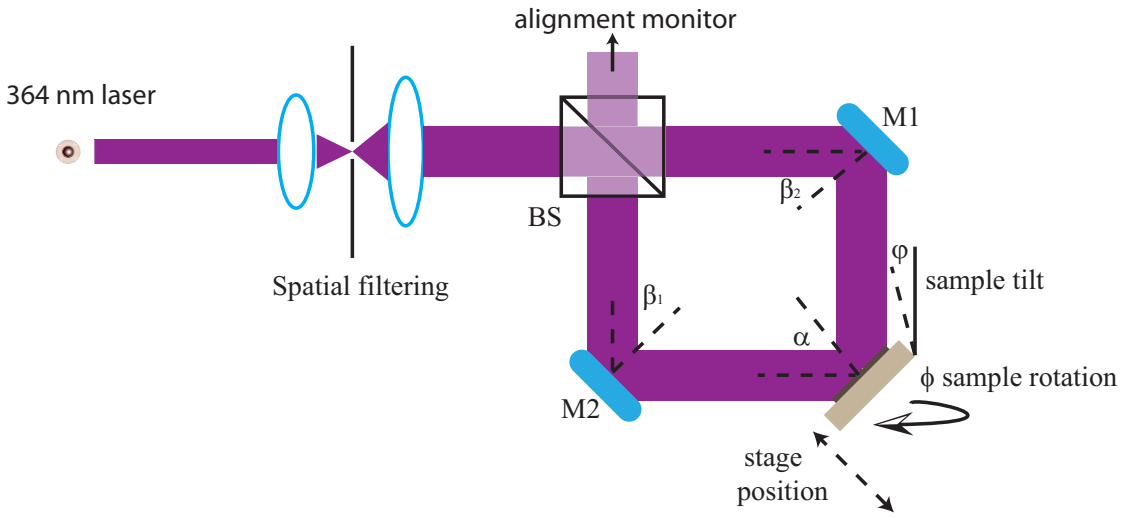

Figure 3.4: An Argon ion laser (364 nm) is expanded and spatially filtered. The beam is split into 2 beams by the beamsplitter (BS) and redirected onto the sample with two mirrors (M1 and M2). The two interfering beams on the sample will create a pattern on the photoresist of the sample. The sample stage can be tilted and rotated by computer control.

seen in Figure 3.5c.

However, with traditional fabrication methods, which require a dry etching step, the nanohole size cannot be reduced after the initial exposure; moreover, the mushroom-like shape in the metal film cannot be achieved to yield the higher localized electric fields. Here, we present a paradigm shift, introducing a straightforward fabrication method in which the void size can be controlled and changed even after holographic exposure. This new technique offers simplicity in fabrication and controllable linewidth by varying the void size. It also offers the ability to reconfigure the nanostructure array by stripping away the gold layer and sputtering another film with a different thickness. The fabrication consists of the formation of the nanohole array in polymer and an oblique metal deposition step. The nanohole array is formed in a thick photoresist by using holographic lithography, as described above. The deposition is achieved by sputtering a controlled layer of gold from an oblique angle as the substrate is rotated on the deposition stage as

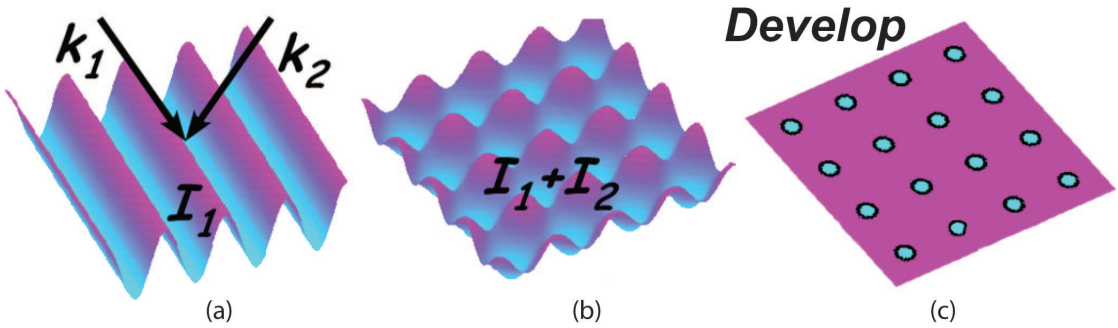

Figure 3.5: (a) For the first exposure, the two beams, k1 and k2, create a 1-D grating pattern. (b) The sample is then tilted 90 ° in the z-plane and a second exposure produces a 2-D sinusoidal pattern. (c) After developing the negative SU8 photosresist, large area 2-D nanohole array is fabricated.

shown in Figure 3.6a. The thickness of this layer is given by:

$$t = R \cdot T \cdot sin\theta, \tag{3.1}$$

where R, T, and θ are the deposition rate, time, and the incidence angle of the sputter ion beam, respectively. The void size is determined by

$$g = d - 2R \cdot T \cdot cos(\theta)\, f, \tag{3.2}$$

where d is the periodicity in the resist and f is a filling factor, empirically calculated to be between 1.1 and 1.3. As the thickness increases, the void size decreases; thus, the size can be precisely controlled by merely adjusting the sputtering time. Figure 3.6b shows a scanning electron microscope (SEM) image of the sideview of the mushroomlike nanostructure after the sample was carefully diced with a laser-cutter to reveal its cross-section profile.

Figure 3.7a shows the uniformity of the holographic exposure technique in fabricating large-area array. In this SEM image, the periodicity is 600 nm. With oblique gold sputtering, the void size can be controlled and Figure 3.7b reveals the complete sealing of the voids with sufficient deposition time.

3.5 Linewidth versus void size

Since the void size determines the scattering rate (and hence, the lifetime) of the SPP mode, decreasing the size gives a narrower transmission linewidth

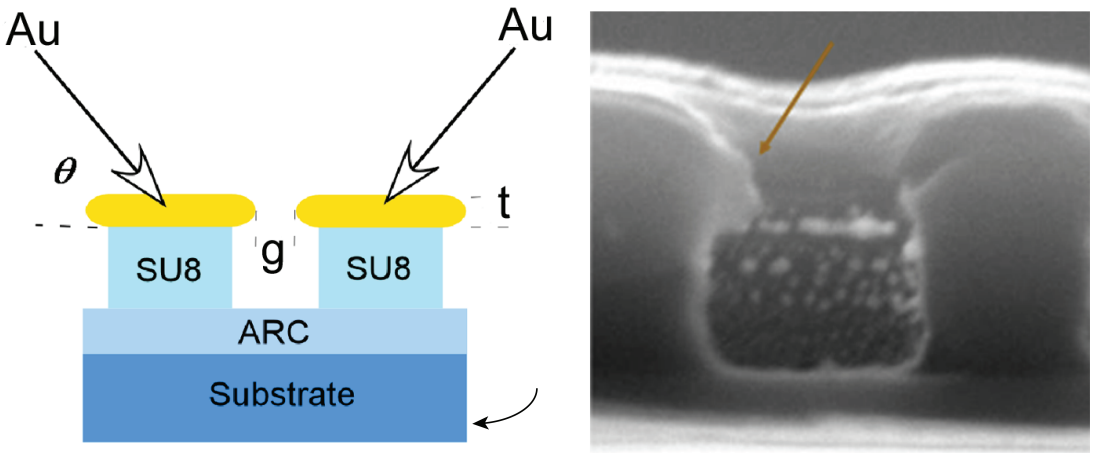

(a) (b)

Figure 3.6: (a) Fabrication setup showing oblique deposition of gold as the stage is rotated. (b) Sideview SEM image of mushroomlike nanostructure. The arrow points to the gold that is protruding out over the photoresist pillar.

[89, 90]. The full-width-half-maximum (FWHM) of the resonant linewidth, Γ, directly dictates the SPR sensor's minimum resolution and resolving power, with a figure of merit defined by $\chi = S/\Gamma$, where S is the sensitivity defined as the derivative of the monitored resonant parameter with respect to the refractive index unit. Hence, a narrower linewidth yields a higher figure of merit.

The transmission spectrum was characterized using the setup described in Ref. [79]. A comparison of the measured spectra is shown in Figure 3.8a for void diameters of 400 nm and 250 nm, with corresponding FWHM linewidths of 0.315 ° and 0.220 °, respectively. These two void sizes were obtained from the same sample by stripping the original gold layer and then depositing another layer of a different thickness onto the same SU-8 photoresist array. The linewidth's dependence on the void size is plotted in Figure 3.8b, verifying that with this oblique sputtering technique the linewidth, indeed, can be controlled by controlling the void size via the sputtered gold thickness. The measurements correspond reasonably well to RCWA simulations with a small discrepancy due to the effects of directly transmitted background, which were included in the simulation but suppressed in the experiment by a polarizer-analyzer arrangement [79]. For void diameters of 150 nm, 200 nm, 250 nm, 300 nm, 350 nm, and 400 nm, the corresponding FWHMs

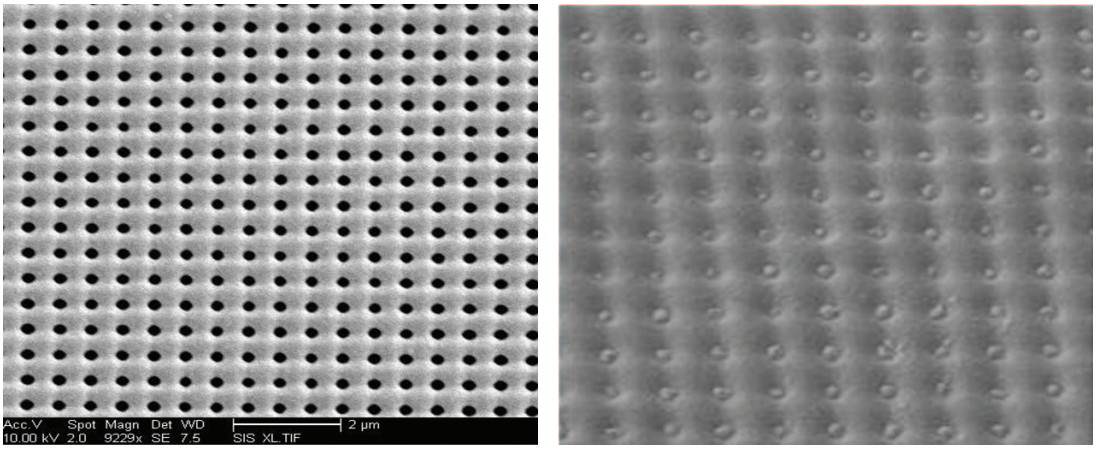

(a) (b)

Figure 3.7: (a) A SEM showing excellent uniformity of the holographic exposure technique. (b) Using oblique gold deposition, the voids had been sealed after prolong deposition time. The image is taken at an angle

are 0.135°, 0.175°, 0.220°, 0.260°, 0.300°, and 0.315°, respectively.

3.6 Hydrophilicity of a surface

In many applications ranging from mechanical engineering to biological science, determining the surface hydrophilicity is very important. Current method measures the contact angle between the solid-liquid-vapor interface. However, this method requires expensive imaging equipments and long image processing time [91, 92]. Instead, we introduce using SPR sensing techniques and the fabricated composite nanostructure array to determine the surface hydrophilicity by measuring the resonant wavelength shift of the laser beam transmitted through the 3-D nanostructure array, which was bonded to a polydimethylsiloxane (PDMS) chamber (See Appendix A for discussion and fabrication of PDMS fluidic channels). The experimental setup consists of a tunable laser with a resolution of 1 pm, an orthogonal polarizer-analyzer pair in between the sample to minimize the linewidth, and a thermoelectric cooler (TEC) for temperature stabilization, as shown in Figure 3.9a. Liquids were flown over the sample delivered using fluidic

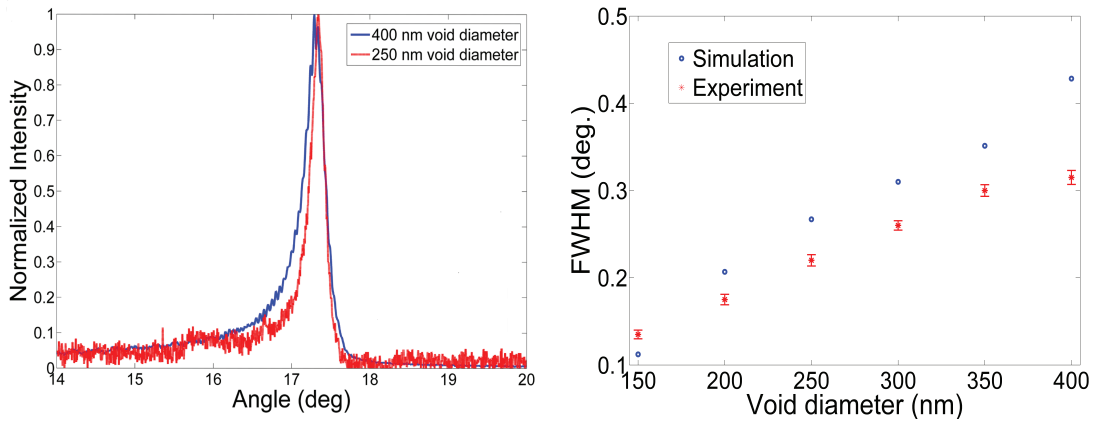

(a) Measurements (b) Measurements vs. simulations

Figure 3.8: (a) Transmission spectra at a wavelength of 1550 nm with void diameters of 250 nm and 400 nm with corresponding FWHMs of 0.220 ° and 0.315 °, respectively. (b) A comparison of the angular FWHM versus the void diameter for both simulation and experimental data.

tubes connected to the inlets and outlets of a PDMS chamber. Figure 3.9b shows a PDMS chamber with four 200-µm-channels bonded to the nanostructure chip.

Only the AM mode was monitored because the required wavelength to excite the liquid-metal mode is outside of the wavelength range of the laser. The surface properties of a clean, unfunctionalized gold surface were investigated. Using a computer-controlled acquisition system, a baseline was established for the resonant wavelength when the PDMS chamber was filled with air. The real-time resonant wavelength shift is given in Figure 3.10a. After 35 minutes, methanol was injected into the chamber and data acquisition began once all the methanol had flowed over the gold surface and exited the 200-µm-wide PDMS channel. The adsorption thickness is related to the resonant wavelength shift by [93]

$$thickness = \frac{l}{2}\frac{R}{S(n_a - n_s)}, \tag{3.3}$$

where l is the field decay length, R is the resonant wavelength shift, S is the sensor sensitivity, n_a is the refractive index of the adsorbed material, and n_s is the refractive index of the surrounding medium. The dynamic adsorption thickness is plotted on the right side of Figure 3.10a. The adsorption thickness decreases

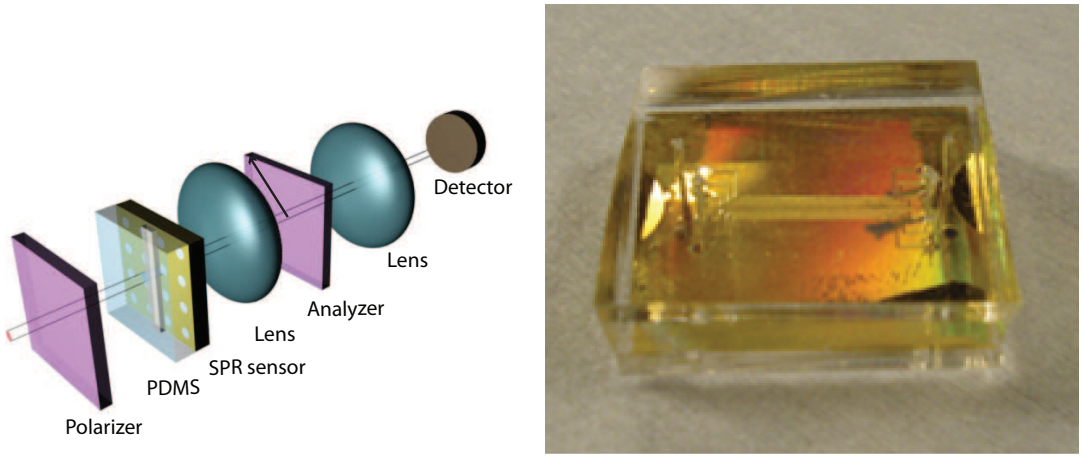

(a) (b)

Figure 3.9: (a) The experimental setup. (b) The fluidic PDMS polymer channels bonded to nanostructure chip.

from 10.7 nm to 6.3 nm over a 6.2-minute span after the initial methanol rinse. Following water rinsing, however, the resonant wavelength shifts instantaneously with a relatively constant adsorption thickness of 0.2 nm over a 5.8-minute span. The shift in the resonant wavelength was monitored for a longer period after the second methanol rinse; an adsorbed methanol layer remains on the gold surface even after 60 minutes. This implies that a clean, unfunctionalized gold surface can be wetted by methanol but is hydrophobic to water molecules. The adsorption thickness returns to baseline when measurement was performed a day later with air in the channel.

In order to modify the surface properties, 3-mercaptopropyl-trimethoxysilane was injected into the PDMS chamber and the chemical solution was left to evaporate overnight. This produced a self-assembled monolayer (SAM) on the gold surface, as evident by the increasing absorption thickness as shown in Figure 3.10b. A similar procedure was conducted to determine the hydrophilicity of the Au-SAM surface to water and methanol molecules. The adsorption thickness after water rinsing has no significant change over a 10-minute span, staying around 22.7 nm. After methanol rinsing, however, the adsorption thickness decreases to only 2.0 nm. From Figure 3.10a and b, it can be seen that the adsorption thickness increases

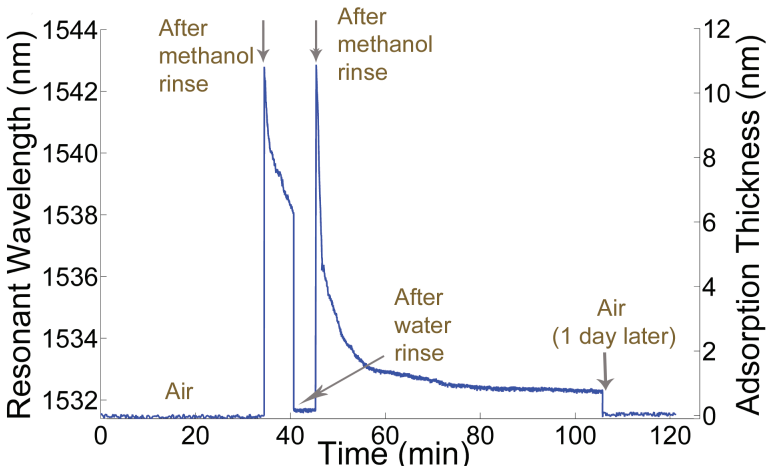

(a) Without SAM

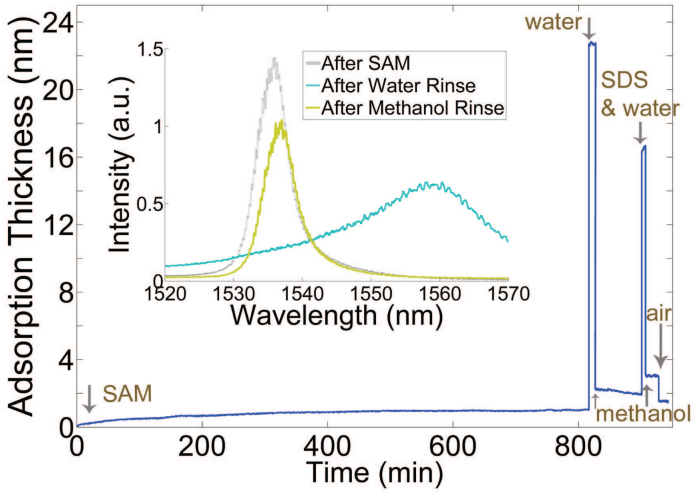

(b) With SAM

Figure 3.10: (a) Without SAM: The measured resonant wavelength shifts and the calculated adsorption thicknesses for the SPR sensor integrated with a PDMS channel for aqueous delivery of water and methanol. The surface is hydrophobic to water molecules but is wetted by methanol molecules. (b) With SAM: The calculated adsorption thickness shows that the SAM has modified the hydrophilicity property for water molecules from hydrophobic to hydrophilic while the surface now resists the wetting by methanol molecules. The insets show three spectra measured after SAM binding, water rinsing, and methanol rinsing.

from 0.2 nm to 22.7 nm, which reveals that the SAM layer had modified the surface from hydrophobic to hydrophilic for water. The modified surface, however, resists the wetting by methanol, where the adsorption thickness drops to 2.0 nm from 10.7 nm for the unmodified gold surface. In Figure 3.10b, the decaying behavior is not observed after water rinsing within the measurement time due to water's low vapor pressure in the chamber. Similar behavior occurs when the sensor was rinsed with a solution of 2% sodium dodecyl sulfate (SDS). The inset shows spectra after SAM formation, water rinsing, and methanol rinsing, with the highest relative intensity of the former indicating the lowest adsorption thickness. This SPR method is being further investigated for quantitative hydrophilicity determination and comparison with the traditional contact angle approach.

3.7 Summary

A composite mushroom-like metallodielectric nanostructure was presented to enhance the normal electric field by coupling between localized plasmons and propagating SPPs. Although an enhancement factor of 1.4 is not extraordinary, the coupling approach shows promise. Optimized design employing LSPR coupling to propagating SPP modes and multiple SPP mode couplings are being studied. The fabrication method introduced here is a low cost and mass-producible technique to construct 3-D composite nanostructures in which samples are reusable and reconfigurable. Tradeoffs between FWHM linewidth and deposition thickness, in terms of its effect on the transmission intensity, will create an optimized design in yielding the best resolution for the SPR sensor. Moreover, other SAM materials can also be used in order to engineer the material's surface properties for applications in biosensing, such as detection of protein interactions on the gold surface, which is discussed in the next chapter.

3.8 Acknowledgement

Chapter 3, in part, is a reprint of the material as it appears in Applied Physics Letters 2009. The dissertation author was the primary investigator and author of this paper. The co-authors listed either helped or supervised the research.

Chen, H. M.; Pang, L.; Kher, A.; Fainman, Y., *Applied Physics Letters*, 94, 073117, 2009.

Chapter 4

Controlled detection in composite nanoresonant array for surface plasmon resonance sensing

The composite mushroomlike, nanoresonant structure introduced in the previous chapter is used to improve the sensor sensitivity of biological recognition reactions via the coupling between the localized surface plasmons and the propagating surface plasmon polaritons. The metallodielectric nanostructure was assembled with microfluidic channels and examined for specific binding events between ligand and analyte and showed pronounced improvement in the limit of detection compared to conventional nanohole array sensing configurations. The temperature influence on the binding affinity and the effectiveness of the control channel were also investigated to demonstrate the capability of the proposed composite nanoresonant surface plasmon resonance array sensor.

4.1 Introduction

Since the discovery of extraordinary transmission through subwavelength nanohole arrays [4], nanohole arrays have been used in surface plasmon resonance (SPR) sensors as an alternative to the prism-based Kretschmann-Raether configuration [74,94] and the diffraction grating approach [77]. While operating at normal

or near-normal illumination, the nanohole array sensing configuration leads to a high packing density with a large number of parallel channels, which enables high resolution imaging with a wide field of view and a large space-bandwidth product [78, 79]. Regular SPR and nanohole array sensing configurations possess well defined sensitivities that are determined by their excitation configurations and the corresponding propagating plasmonic mode dispersion relationships [41,82]. Alternative approaches utilize nanoparticle-based SPR, whose sensitivity depends on the near-field amplitude of the electric fields that are created by the excited localized surface plasmon resonances (LSPRs) used to detect the binding effects [51, 95–97]. Although nanohole array based sensing configuration holds great advantage of potential high-throughput, the achieved limit of detection is still below the well-developed thin film based SPR sensor [82]. In order to improve the limit of detection by increasing the sensitivity of the nanohole array based sensor configuration, the coupling between the LSPRs and propagating surface plasmon polaritons (SPPs) was investigated [85], and its potential to further increase sensitivity was proposed [83]. Additionally, suppression of the influences from environmental variations is also crucial. SPR sensor configurations detect a change in the refractive index, which is an overall manifestation of specific bindings, nonspecific binding events on the sensor surface, variations in the bulk concentration, and temperature fluctuations in the environment. Therefore, the improved sensing technique would also be susceptible to the background, making it impossible to accurately identify the biological recognition reaction in low concentrations. In this chapter, the composite mushroom-like metallodielectric nanostructure (MMN) is presented as an alternative approach to couple these two types of plasmonic phenomena and exploit them for practical applications such as recognition reactions. The enhancement of the electric field amplitude due to the LSPR is combined with the propagating SPP in the composite nanoresonator design. With this approach, instead of nanoparticles, nanovoids are used to create nanoresonators to excite LSPRs. The MMN was integrated with microfluidic channels to examine biological recognition reactions, showing more than one order of magnitude improvement in the limit of detection in comparison to that achieved with conventional sensor configuration

exploiting SPP in metal film perforated with a 2-D nanohole array.

4.2 Method

The concept of a nanoresonant array structure where nanoparticles are integrated into the 2-D metal film perforated by a nanohole array is shown in Figure 4.1. The period is designed to satisfy the phase matching condition (i.e., momentum conservation) for excitation of SPP wave propagating along the metal surface. The excited SPP wave couples into the nanoparticles to excite LSPRs around the nanoparticles, enhancing the amplitude of the electric field on the surface of the nanoparticles, thereby increasing the sensing ability of the resonant structure. However, since the practical realization of such a structure on a large area will be challenging (see Figure 4.1a), we introduce a close alternative, its complementary arrangement, consisting of nanovoid to replace the nanoparticle for excitation of LSPRs (see Figure 4.1b). This configuration can be easily realized as was outlined in Chapter 3. The proposed geometry is a layer of structured gold film on top of a perforated substrate, in which the film protrudes out over the perforated substrate, forming nanovoids. The size of the nanovoids can be controlled independently of the underlying cylindrical perforation. When SPP waves propagate, they are reflected by the gold barriers, interfering with each other and forming localized standing SPP waves. The LSPRs are also excited near apexes; since the propagating SPP resonance and the LSPR are coupled, these two mechanisms can be utilized to enhance the amplitude of the electric field.

The period of the MMN sensor chip is designed for operation at near normal incidence angle for excitation of SPP resonance, facilitating operation with large size arrays with parallel detections, while avoiding the interference of SPP modes at normal incidence [98]. To satisfy the phase matching conditions for excitation of propagating SPP (1,0) mode on a water-metal interface, we use a period of 1.20 µm for operation at a wavelength of 1.55 µm at an incidence angle of 1.5 degrees. The excitation of the water-metal SPP mode is further validated using rigorous coupled wave analysis (RCWA) to calculate the far-field transmittance and validated with

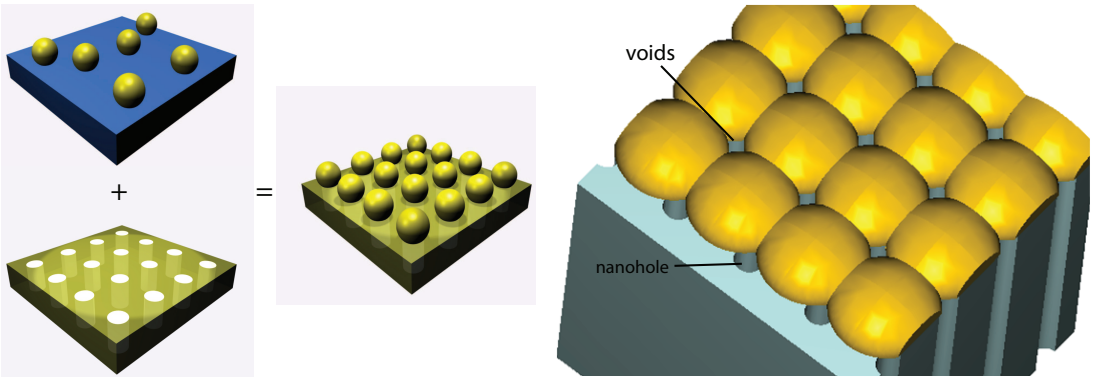

(a) (b)

Figure 4.1: (a) Conceptual diagram of a 3-D nanoresonator array structure combining LSPRs and SPP in a metal film perforated by 2-D nanohole. (b) Schematic diagram of the proposed nanovoid geometry for practical realization of LSPRs coupled with SPP in a 2-D metal film perforated with nanohole.

2-D finite element method simulations.

The MMN void size is 25 nm to excite the localized resonant LSPR as shown in Figure 4.2a. For comparison, Figure 4.2b show the near-field distribution with the same scale for a conventional nanohole structure in a gold film with the same parameters as the resonant void in the MMN substrate. The incident electric field from the top is set at $E_x = 1\,(\mathrm{V/m})$ for both the MMN and the nanohole substrates in the FEM simulations. As we know, the resonant conditions for the nanoparticle depend on its size and shape [97]. Our calculation reveals that the excitation of LSPR in the nanovoid also depends on the size of the void (or the gap) and the curvature of the apexes of the void edge. As shown in Figure 4.2a, a LSPR is excited in the nanovoid with a 25-nm gap and a 25-nm apex radius of curvature with an opening of 200 nm for the resist pillar, whereas no resonance is excited in the regular nanohole with a diameter of 200 nm as shown in Figure 4.2b. The intensity of the electric field is about $1\,(\mathrm{V/m})^2$ in most of the nanohole area. In both cases, the propagating (1,0) water-metal SPP mode along the interface is excited as indicated in Figure 4.2c and d, in which the intensity of the electric field decays exponentially away from the metal surfaces. The enhancement factor for the maximum intensity, $\frac{|E_y|^2_{MMN}}{|E_y|^2_{nanohole}}$, is about 7.5 times. In order to compare the

electric field enhancement of our MMN substrate, amplitudes of the total electric field, $E_{norm} = \sqrt{|E_x|^2 + |E_y|^2}$, are calculated, which gives an enhancement for the maximum electric field of about 5.7. For sensing application, resonant shift relies on the average response of the attached molecules interacting with the electric field in certain region above the metal surface. Therefore, a 50-nm-subdomain integration of the electric fields above the gold surface and the gap space in between the gold rods were performed. It gives an enhancement factor of 2.6 over the subdomain integration for the MMN structure compared to the nanohole structure. This near field electric field enhancement is due to the excitation and coupling between localized SPR and propagating SPP mode; therefore, the enhancement would affect SPR sensing activities as shown below.

The near field electric field enhancement is due to the excitation and coupling between localized SPR and propagating SPP mode; consequently, the enhancement may affect the SPR sensing activities through the sensitivity enhancement by the effective index shift and a decrease in the penetration depth of the electric field. The sensitivity for a sensor is defined as the derivative of the monitored resonant parameter (e.g., angle, wavelength, magnitude, or phase of the field) with respect to the parameter that needs to be detected (e.g., refractive index or concentration). The sensitivity depends on the method of the SPR excitation, interrogation configuration, and metal and dielectric properties. For biosensor, the sensitivity corresponds to surface refractive index change near the metal sensing surface, referred to as the surface sensitivity. The verification of the sensitivity relies on the knowledge of the thickness and the effective index of the bio-layer above the sensing surface, which usually can not be well defined in the experiment. Instead the limit of detection is used to characterize the sensor's capability. The limit of detection corresponds to the minimum change in the refractive index or concentration that can be detected with reasonable certainty. In the semi-infinite metal and dielectric plasmonic sensor configuration, the surface sensitivity [99] can be expressed as

$$S_{surf} = S_{bulk}\frac{2h}{L_{pd}} \sim \left(\frac{\partial n_{eff}}{\partial n}\right)_{bulk}\frac{2h}{L_{pd}}, \tag{4.1}$$

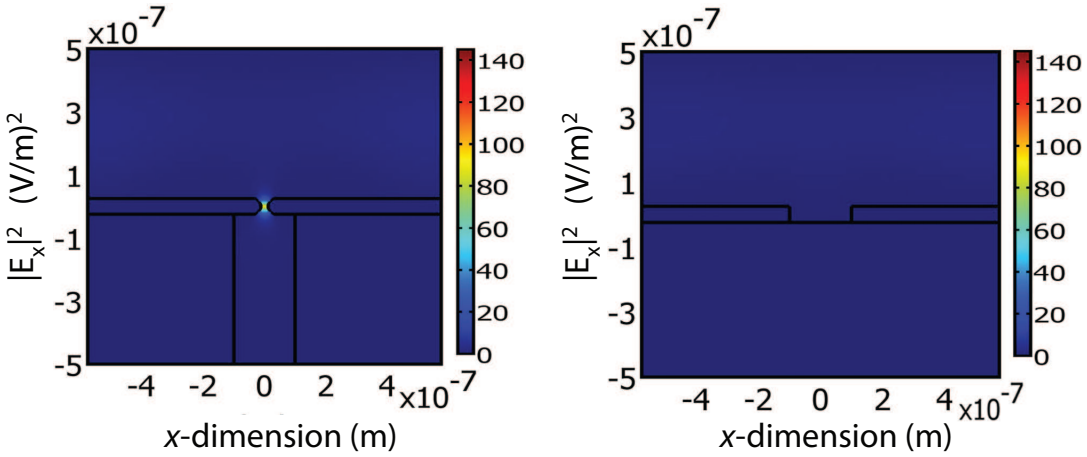

(a) Mushroomlike array E_x intensity

(b) Nanohole array E_x intensity

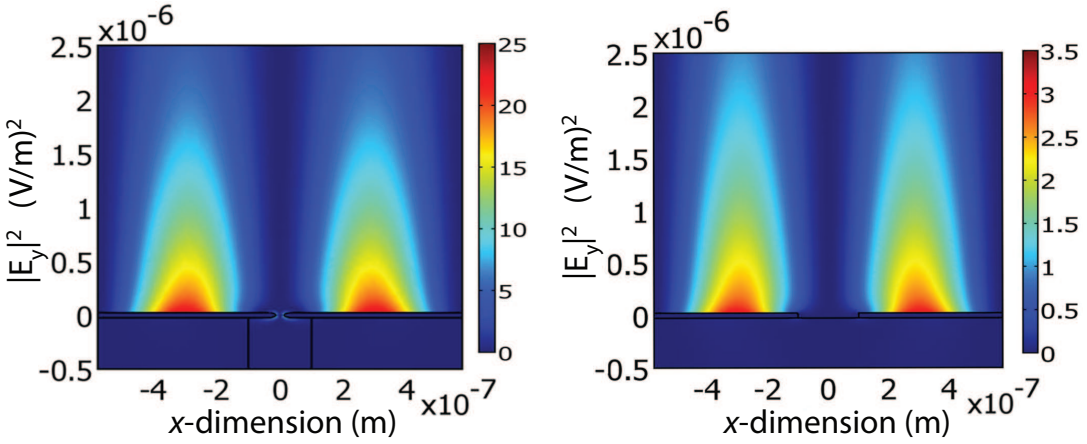

(c) Mushroomlike array E_y intensity

(d) Nanohole array E_y intensity

Figure 4.2: (a) The E_x intensity distribution for the MMN structure. (b) The E_x intensity distribution for the nanohole structure. (c) The intensity distribution of the electric field in the MMN substrate on the water-metal interface. (d) The intensity distribution of the electric field in the nanohole substrate on the water-metal interface. Notice the shorter evanescent tail of the SPPs in (c) and the higher intensity scale compare to (d). Periodic boundary conditions were used, so only one unit cell is shown.

where S_{surf} and S_{bulk} denote the surface and bulk sensitivity, respectively, h is the limited distance from the metallic surface whose index would change, n_{eff} is the effective index of the plasmon, and L_{pd} is the penetration depth, which is defined as the distance from the interface at which the amplitude of the field decreases by a factor of $1/e$. For the sensing configurations presented here, equation (4.1) may still hold, which means that the surface sensitivity is proportional to the bulk sensitivity and inversely proportional to the penetration depth of the electric field. From Figure 4.2, the evanescent tails of the SPPs are shorter in the MMN substrate than that in the regular nanohole substrate, that is, shorter penetration depth. The reduction factor of the penetration depth is about 3.1/2.2 = 1.4. In addition, the effective index may also be affected due to the enhanced surface electric field originating from the excitation and coupling of the LSPR. The surface sensitivity enhancement was simulated by monitoring the peak resonant wavelength shift when the refractive index of a thin layer was changed from the surface of metal film. In this simulation, the peak resonant wavelength in the far field S-parameter was monitored when a 50-nm-thick adlayer with a refractive index of 1.37 was added onto the gold surface to simulate a biosensing binding event. Both the MMN and the nanohole array substrates were simulated and the calculated surface sensitivities, defined by the ratio of resonant peak wavelength shift to the surface index change, were 30 and 6 nm/RIU, respectively, where RIU denotes refractive index unit. The surface sensitivity is about 5 times higher for the MMN structure compared to the nanohole structure.

4.3 Proteins binding results

Next we integrate the MMN substrate with a microfluidic delivery chip to investigate the binding event between immobilized receptor and analyte in a flowing solution by real time monitoring of the resonant transmission wavelength through the MMN device. The microfluidic delivery chip is fabricated in poly-dimethylsiloxane (PDMS) using soft lithography method. A chamber consisting of six $2000\times100\times50\,\mu m^3$ channels with 100-μm separation walls was then bonded

to the composite MMN substrate by applying oxygen plasma bonding. In order to overcome the poor adhesion between PDMS and the MMN gold surface, the bonding was accomplished through an additional lithographic processing step where patterned channel of thin SiO_2 film was deposited directly onto the MMN surface before attaching the PDMS channel. The upper left inset in Figure 4.3 shows the assembled device, where the color illustrates the diffraction from the perforated array. Tubes connected to needles were inserted into the ports of the corresponding PDMS channels for on-chip optofluidic control and measurements. The assembled device was mounted on a precision rotation stage, where three channels can be seen connected with tubes. The measurement setup layout also consists of the microfluidic delivery system, which includes a microcontrolled pump (VICI Valco Instruments, M6 CP-DSM) with adjustable flow rate and a mechanism to control the flow rate using height adjustable syringes. The optical setup is illustrated in Figure 4.3, where the assembled chip is mounted on a rotational stage (Physik Instrumente, M-037.PD) and illuminated by a polarized monochromatic laser beam (Newfocus Venturi Tunable laser TLB 6600), while directly transmitted background is filtered out by an orthogonally oriented analyzer [79]. The SPP resonant transmission signal is acquired by a power meter (Newport 818-IR).

The dispersion relation of the water-metal SPP modes was measured by scanning both the wavelength and the angle of incidence (see Figure 4.4a). We observe that for operation at semi-normal incidence of 2 to 4 degrees with an array period of 1.2 µm, the operating wavelength range will be 1520 - 1570 nm. The slight angle discrepancy from the simulation is due to the accuracy of the indices used in the simulation. The incident angle was set to be 3 degree to excite the water-metal (1,0) mode with a resonant wavelength around 1536 nm.

This setup was used for real-time monitoring of the interaction between immobilized biotinylated bovine serum albumin and flowing streptavidin by observing the SPP resonant wavelength shift while keeping the incidence angle fixed. The experiment was designed to block the nonspecific binding and eliminate environmental variations (i.e., temperature or pressure). Experiments were conducted in the signal and control channels. In the calibration experiment, the same reac-

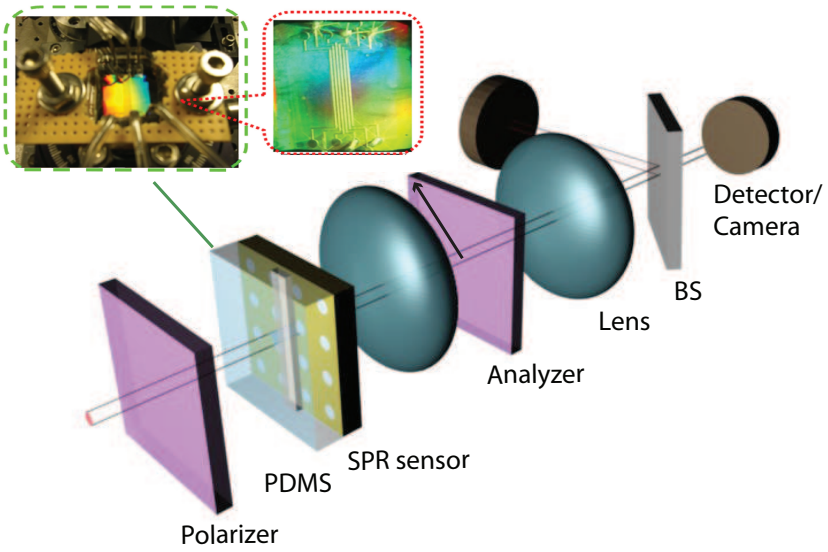

Figure 4.3: Schematic of the optical setup utilizing two channels. The upper left inset shows an assembled sensor chip with three channels connected with tubes and shows the microfluidic channels on the nanoresonant gold surface.

tion data were obtained in the signal and control channels when they were filled with the same solution from phosphate buffered saline (PBS) buffer solution to biotinylated bovine serum albumin (BSA) immobilization to streptavidin interaction. A series of experiments on recognition reactions with different streptavidin concentrations were also conducted in both channels to ensure identical response, as shown in Figure 4.4b.

After the sensor chip was assembled, the signal channel was filled with biotinylated BSA of 50 g/ml in PBS with 1% 2-mercaptoethanol for more than 2 hours. The control channel was filled with BSA of the same concentration for the same time duration. Then both channels were connected to a single input afterward to experience the same flow rate. First, 50 g/ml of BSA solution was introduced into both channels for twenty minutes to cover any possible bare Au surface, blocking any possible streptavidin nonspecific binding sites. Both channels were then washed with PBS and then real-time monitoring commenced as shown in Figure 4.5. The red and blue curves correspond to the control and the signal channels, respectively, which exhibit 0.6 nm resonant bias. The sensor chip was mounted on a custom ordered thermo-electric cooler (TEC) module. The center

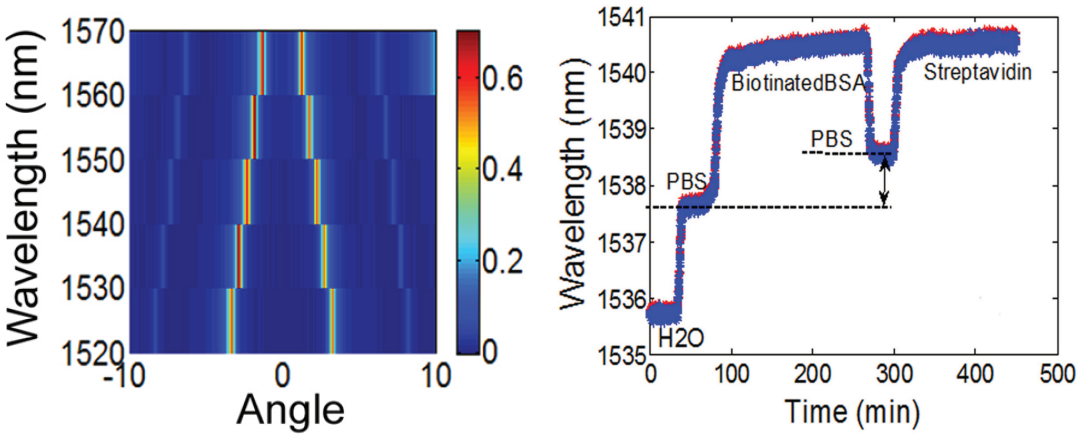

Figure 4.4: (a) Angular spectra of the nanoresonant array sensor with water inside the channel; the two weak resonant spectra in the larger angle of incidence correspond to PDMS-Au SPP modes. (b) Calibration of signal and reference channels to ensure identical responses from both channels for identical solution flow.

portion of the TEC was removed and the substrate of the sensor chip was mounted onto the edge of the TEC module. First, the temperature was set at a room temperature of 23.5° C. After about 40 min, the temperature was raised to 55° C, and then reduced back to 23.5° C. The change in the environmental temperature is clearly evident in the real-time detection as shown in Figure 4.5a. When the temperature increased, the resonant response dropped rapidly due to the decrease in the refractive index of PBS. After the temperature was reset back to 23.5° C, the resonant response restored slowly.

After about 140 min, the resonant response had shown very slow change. Then 50 ng/ml of streptavidin was introduced into both channels. The resonant shift in the signal channel (blue curve) started increasing relatively quickly, while the control channel (red curve) exhibited constantly slow change. After about 60 min, PBS was introduced into both channels for about 30 min, followed by 500 ng/ml of streptavidin for additional binding test. The resonant response in the signal channel started to shift more rapidly until it reached saturation, whereas the control channel maintained the same pace. Finally, PBS was introduced into both channels, washing away the unbound streptavidin in both channels. In or-

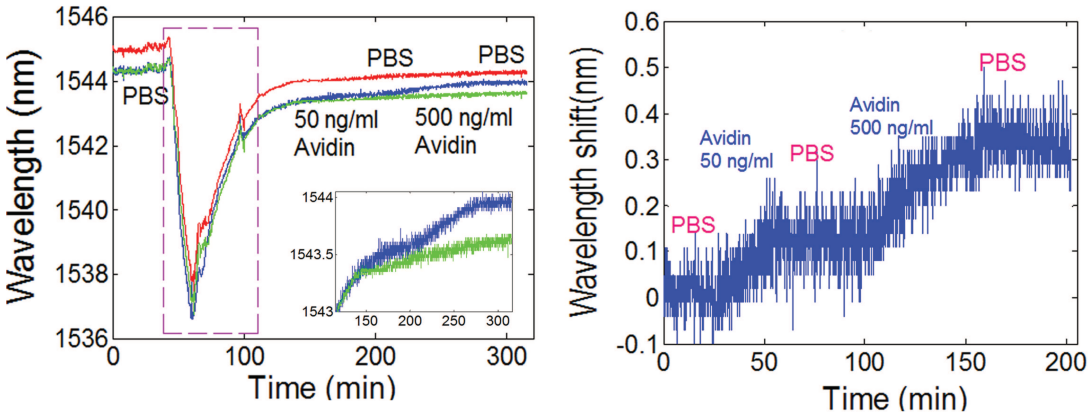

(a) (b)

Figure 4.5: (a) Real-time monitoring of binding between biotinylated BSA and streptavidin following the immobilization of biotinylated BSA in the signal channel and BSA in the control channel. Red, green, and blue curves correspond to control, shifted control, and signal channels, respectively. The inset in (a) is a close-up in signal and shifted control channels after they reached the same temperature. (b) Relative wavelength shift for the binding reactions by subtracting the shifted control (green) from the signal channel (blue).

der to clearly see the biochemical reactions in the control and signal channels, the bias between the two channels was removed by shifting the control channel response by -0.6 nm, which resulted in the green curve in Figure 4.5a. Compared with the shifted control curve, the specific binding in the signal channel can now be seen more clearly. Comparing the shifted control (i.e., green curve) and the signal (i.e., blue curve) channel, the two curves almost overlap before the introduction of streptavidin, except for the rapid temperature change as indicated by the dotted box in Figure 4.5a. The difference in the resonant response in the box indicated the non-uniform temperature distribution in the two channels, which resulted from the relative position difference of the two channels on the TEC module and could be resolved by prolonging the heating or cooling cycle for uniform heat distribution. The ripples on the two curves appeared as a result of the rapid pressure shift in the pump system. The consistency of these ripples in the two curves confirmed them to be a systematic error. When the temperature of the sensor chip slowly decreases, reaching room temperature, the two curves (blue and green)

overlapped again. As seen in the inset, which is a zoom-in of the blue and the green curves in Figure 4.5a after reaching room temperature, the slow evolution of the control curve indicates nonspecific binding and temperature drift in both channels. These environmental influences can be eliminated by subtracting the control response from the signal channel as shown in Figure 4.5b, whose origin was reset. Figure 4.5b clearly shows the different reaction stages from PBS base line, 50 ng/ml streptavidin binding, PBS washing, 500 ng/ml streptavidin binding, and final PBS washing. The 50 ng/ml streptavidin binding gives 0.13 nm resonant shift. Considering the standard deviation of 15 pm for the current setup, obtained from monitoring the resonant drift of PBS, with 3 times the standard deviation, the limit of detection would be 17 ng/ml (0.3 nM), which is much lower than 3 g/ml (26 nM) achieved with regular nanohole array sensor [82]. The improvement in the limit of the detection arises from the surface sensitivity enhancement due to the excitation of LSPRs and the improvement in the signal acquisition by the use of a control channel for eliminating nonspecific binding reactions.

From Figure 4.5b, we can see that the data is noisy, which will affect the accuracy of the limit of detection calculation. In general, the sensor noise originates from the optical source and electronic readout. Dominant sources of noise are fluctuations in the light intensity, scanning wavelength repeatability of the laser source, and photocurrent noise in converting light intensity into photoelectrons by the detector and the supporting circuitry. In the measurement, we scanned the wavelength of the laser, defined the resonant peak wavelength through a basic centroid method, and plotted the wavelength versus time. Averaging among multiple wavelength scans was not employed before tracking the peak wavelength. By averaging multiple wavelength scans, we can reduce the noise resulting from the laser intensity fluctuation and the wavelength variation. We used a power meter head as a detector, whose shot noise is higher compared to either a cooled low-noise PIN or APD detector, which we plan to use in the future. We believe that the above measures would lower the standard deviation of the system and improve the limit of detection of our sensing system even further.

As evident from Figure 4.5a, both the resonant response in the control

and the signal channel are shifted by about 1 nm after they "recovered" from the temperature change. This could have resulted from a mechanical error of the rotation stage. This issue will be resolved in our future prototype system. Another possible reason for the partial shift could be due to the disassociation of immobilized biotinynated BSA and BSA. Nevertheless, these shifts did not affect the final experimental result because these factors occurred in both channels and were eliminated to obtain only the specific binding events by subtracting the control response from the signal channel.

4.4 Summary

A composite nanoresonant structure with nanovoids in metallic film was presented and demonstrated to have enhanced sensitivity in biorecognition reactions. The enhancement is realized by coupling the LSPR from the propagating SPP, resulting from the periodic perforation under the phase matching condition. The fabrication method introduced here represents a cost-effective way to build the composite nanostructures in which the chips are reusable and reconfigurable, since the metallic layer can be stripped away and re-deposited with a different nanovoid diameter. Although the control channel concept was introduced for prism-based sensing configurations [100–102], here the control channel was employed to improve the limit of detection of nanoresonant SPR sensor by taking advantage of its potential for large amount of parallel detection characteristics. Nonspecific binding and environment vibrations were eliminated by the extraction of the control channel from the signal channel. Moreover, specific binding was verified to be still efficient after certain heating process. By using the nanoresonant, the limit of detection is improved to sub-nM, a substantial improvement to the tens of nM in conventional nanohole array SPR sensor. A prototype setup with various concentration arrangements is being built for comprehensive evaluation based on hundreds of detection spots using a CCD camera or detector array.

4.5 Acknowledgement

Chapter 4, in part, is a reprint of the material as it appears in Optics Express 2009. The dissertation author performed the simulations and helped with the experiments and writing of the publication.

Pang, L.; Chen, H. M.; Wang, L. L.; Beechem, J. M.; Fainman, Y., *Optics Express*, 17, 14700-14709, 2009.

Chapter 5

Real-time template-assisted manipulation of nanoparticles in a multilayer nanofluidic chip

The ability to control dynamically the flow and placement of nanoscale particles and biomolecules in a biocompatible, aqueous environment will have profound impact in advancing the fields of nanoplasmonics, nanophotonics, and medicine. Here, we demonstrate an approach based on electrokinetic forces that enables dynamically controlled placement of nanoparticles into a predefined pattern. The technique uses an applied voltage to manipulate nanoparticles in a multilayer nanofluidic chip architecture. Simulations of the nanoparticle's motion in the nanofluidic chip validate our approach and are confirmed by experimental demonstration to produce uniform 200-nm-diameter spherical nanoparticle array. The results presented here are important as they provide a new method that is capable of dynamically capturing and releasing nanoscale particles and biomolecules in an aqueous environment which could lead to creation of reconfigurable nanostructure patterns for nanoplasmonic, nanophotonic, biological sensing, and drug delivery applications.

5.1 Introduction

With the advancement of nanotechnology, chemically synthesized nanocrystals and quantum dots in an aqueous environment have become essential nanomaterials for biolabeling and biosensing for single molecule detection [17, 67, 68, 103–105]. Now, with the introduction of novel synthesis techniques, high quality nanocrystals and nanoparticles of various sizes and shape distributions are possible [17, 104], which are far beyond what traditional lithographic methods can achieve. However, the colloidal nature of these nanostructures makes it difficult to control their position to form highly symmetric nanostructures for nanophotonic or nanoplasmonic applications; hence, immense attentions need to be devoted into making nanoparticle-based photonic materials and devices a reality. Materials with such shape and scale can hardly be fabricated with electron beam lithography due to their ultra-small scale and spherical, three-dimensional geometry. Although self-assembly techniques [106, 107] have made great strides by using biomimetic antibody-antigen recognition [108], biopolymeric scaffolding and DNA motif [109, 110], and Langmuir-Blodgett technique [111, 112] to form highly packed structures, the real-time manipulation of nanoparticles into a regular pattern has not been demonstrated in an aqueous, biocompatible environment, where it has been shown theoretically that the sensitivity of a coherently-spaced, periodic nanoparticle array is nine times higher than that of a single nanoparticle in an aqueous environment [62]. Furthermore, precise nanoparticle manipulation is highly desired when using nanoparticles as carriers to deliver drug into specific position within an organism [113] or in single molecule detection scheme. Although the optical tweezers can manipulate particles at the micrometer scale [114, 115], it is presently impractical to use optical field for manipulation at the nanoscale due to the force decay dependence on the particle's size and the diffraction limit of focusing light down to the nanometer scale. Instead, several methods have been demonstrated for placement of nanostructures by exploiting the electrostatic potential gradient between patterned strips of chemically modified surfaces with positively and negatively charged characteristics [116], by combining microfluidic with surface patterning technique to align nanowires [117], and by using capil-

lary forces to trap nanoparticles into lithographically predefined trenches after the drying process [118, 119]. However, all these techniques are static and cannot be monitored in real-time nor *in vivo*, where the ability to reconfigure nanophotonic structure with freshly functionalized nanoparticles would greatly benefit *in vivo* sensing. In this work, we present a new synergetic combination of colloidal nanostructures with lithographic pattern, electrical field, and micro- and nanofluidics to control nanoparticles into a predefined pattern by applying a voltage to realize real-time, nanophotonic system in an aqueous, biocompatible environment. We envision that our process can be extended to biomolecules and quantum dots in a solution-based platform where various nanostructure patterns can be realized by designing the corresponding nanochannel pattern.

5.2 Schematic of multilayer nanofluidic chip

As shown in Figure 5.1, our concept is a multilayer fluidic platform with both microfluidic and nanofluidic channels, where the top and bottom layers consist of microchannels and an intermediate layer consists of nanochannels fabricated from nanoholes. The size of the nanochannel can range from a few nanometers to hundreds of nanometers, depending on the application requirements. The nanoparticles in suspension are delivered into the device from the inlet on the top microchannel (Figure 5.1a). Electrokinetic forces were ultimately used to control the flow of nanoparticles onto the nanochannel rather than pressure gradient, since the fluid speed is largely independent of the channel size for the former while the pressure gradient must increase inversely to the square of channel size to maintain a given flow speed [120]. At the nanoscale, the required pressure gradient becomes so high that leakage becomes problematic for the polymer channels. Moreover, electrokinetic forces can potentially control individual nanoparticles. Both lateral flow (across the individual microchannel) and transverse flow (from the top microchannel, through the nanochannel, and out of the bottom microchannel) can be controlled by changing the direction of the electrostatic field resulting from applying voltages to the different electrodes. The charged ions in the solution will drag

the solution through the channels from the inlet to the outlet. V1 and V2 electrodes are used for lateral control; while for transverse control, either V1 and V4 or V2 and V3 are used (see Figure 5.2a or Figure 5.5a). Figure 5.2a illustrates the simulated particle flow for a negatively charged nanoparticle when V4 is connected to a positive potential, V1 is grounded, and V2 and V3 are disconnected. With an applied electric field to induce 'nanoflow', the nanoparticles are captured onto the opening of the nanochannels and assemble themselves according to the underlying nanochannel pattern, forming a real-time nanophotonic structure. The functionality of the assembled structure depends on the designed nanochannel pattern and its effective index of refraction as determined by the size of the nanochannels, the nanoparticle's properties, such as its index of refraction, and the depth in which the nanoparticles are trapped into the nanochannels. For example, the shifting of the transmission peak can be observed when nanoparticles are captured onto the nanochannels, analogous to a recent paper that used photonic crystal for detection of bio-organism simulants [121].

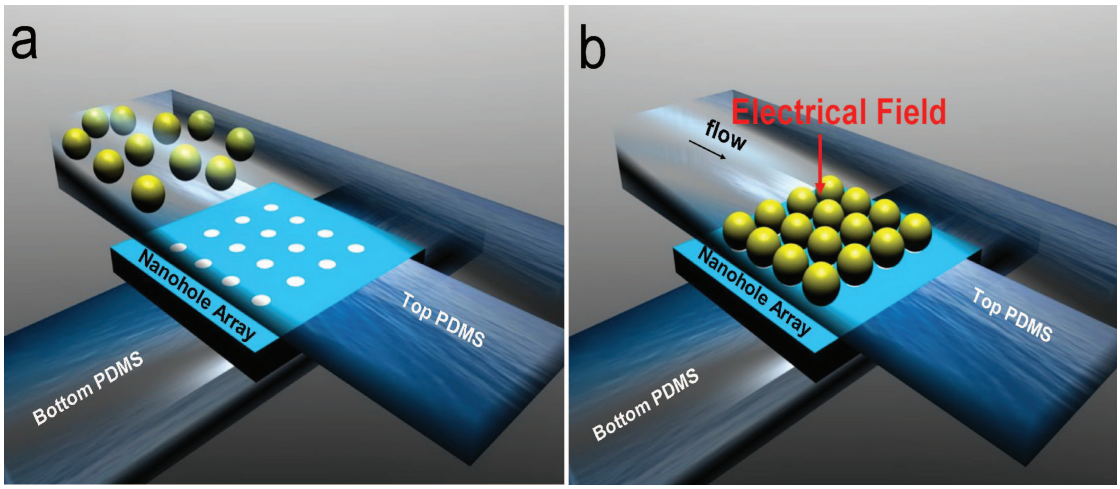

Figure 5.1: Schematic diagram of the multilayer nanofluidic architecture (a) Nanoparticles are flown in from the left inlet on the top PDMS chamber. (b) When an electric field is applied, the nanoparticles are captured onto the underlying nanochannel membrane defined by the nanohole pattern, connecting the top PDMS to the bottom PDMS.

5.3 Theory and simulation of nanoparticle fluidic flow

The mechanisms for manipulating nanoparticles through micro and nanochannels are well developed, in which two main phenomena can drive the flow of a saline solution with an applied electric field [120, 122–125]. The first effect arises from an electroosmotic flow, in which charged liquids are formed close to the channel wall's surface and the particle's surface, creating electrical double layers whose polarities are material dependent. The applied electric field displaces the charged liquids in the electrical double layers to generate this electroosmotic flow. The second effect (electrophoresis) occurs as water molecules are dragged along by the ions, which are either propelled or repelled by the electric field depending on their polarity. First, the fluid-particle interaction was simulated to understand the exact behavior of the particle dynamics in the fluid medium. A generalized Galerkin finite element method was chosen to incorporate both equations of the fluid flow and of the particle motion into a single variational equation, allowing the hydrodynamic interactions to be eliminated and rendering the explicit evaluation of the hydrodynamic interactions unnecessary [122]. To track the position of the particle, the moving mesh method was chosen and implemented in finite element method (FEM) simulation since the fluid-particle interface is clearly defined at each time step. It considers the relative position of the particle as a boundary of the fluid domain and uses an arbitrary Lagrangian-Eulerian (ALE) technique to create the mesh grid at each time step [126]. The particle surface and its interior are considered as a single entity that moves with the particle. The fluid velocity is computed using Laplace's equation. The mesh grid is updated based on the motion of the particle and is checked for element degeneration at each time step. If the detected distortion in the mesh is beyond a pre-defined threshold, a new mesh is generated and the fluid flow fields are projected from the old grid onto the new grid. To validate our concept, simulations were done for a two-dimensional structure with one nanoparticle and one nanochannel to reduce computational complexity. A transient model was used to study the simultaneous translation and rotation of

the particle. In order to readily solve the electrophoretic problem, a coordinate transformation was performed. The particle is fixed and its translational velocity after nondimensionalization, V_p^*, is transferred to the channel walls. The transient boundary conditions are

$$\mathbf{v}^* = \gamma(\mathbf{I} - \mathbf{nn}) \cdot \nabla^* \phi^* \tag{5.1a}$$

$$\mathbf{v}^* = \mathbf{V}_p^* + \omega_p^* \times (\mathbf{x}_p^* - \mathbf{X}_p^*) + (\mathbf{I} - \mathbf{nn}) \cdot \nabla^* \phi^* \tag{5.1b}$$

where $\gamma = \zeta_w/\zeta_p$ is the ratio of the zeta potential of the channel wall to that of the particle, $(\mathbf{I} - \mathbf{nn}) \cdot \nabla^* \phi^*$ defines the nondimensionalized electric field tangential to the surface where $\mathbf{I}$ is the identity tensor and $\mathbf{n}$ is the unit vector in the x-direction across the fluidic channel, V_p^* is the nondimensionalized translational velocity of the particle in the x-direction, ω_p^* is the nondimensionalized rotational velocity, $\mathbf{x}_p^*$ is the nondimensionalized position vector of the particle boundary, and $\mathbf{X}_p^*$ is the nondimensionalized position vector at the center of the particle [123–125]. The system of equations is nondimensionalized using the following parameters: the particle's radius a, the applied electric voltage ϕ_o, and the electrophoretic velocity of the particle in an unbounded flow defined as $V_\infty = (\epsilon\epsilon_\mathrm{o}\zeta_p/\mu)(\phi_\mathrm{o}/a)$, where ϵ is the dielectric constant of the electrolyte solution, ϵ_o is the permittivity of vacuum, and μ is the fluid viscosity. In these calculations, time is nondimensionalized as $t^* = (V_\infty/a)t$. The fluid velocity $\mathbf{v}$ on Γ_in and Γ_out (the inlet and outlet) was solved using the coupled Navier-Stokes and electrical DC conductive application mode in the FEM software, with fluid velocity boundary conditions applied on Γ_wall and Γ_particle.

For each time step, Newton's second law is solved for the translational and rotational velocities using

$$\mathbf{F}^* = \int \sigma^* \cdot \mathbf{n}\, d\Gamma_p^* = m^* \frac{d\mathbf{V}_p^*}{dt^*} \tag{5.2}$$

$$\mathbf{T}^* = \int (\mathbf{x}_p^* - \mathbf{X}_p^*) \times (\sigma^* \cdot \mathbf{n})\, d\Gamma_p^* = I^* \frac{d\omega_p^*}{dt^*}, \tag{5.3}$$

where σ^* is the nondimensionalized stress tensor, m^* is the particle's nondimensionalized mass and I^* is the moment of inertia of the particle.

5.3.1 Moving mesh simulation of nanoparticle in fluid

Figure 5.2a shows the time evolution of the particle when a voltage is applied between terminal V1 and V4. Simulations show that the particle is manipulated by the applied electric field and is captured onto the nanochannel. Figure 5.2b shows the normalized velocity of the particle versus the simulated time. As the particle nears the surface of the nanochannel, the velocity increases dramatically as the particle is pulled onto the nanochannel. The values used in the simulation

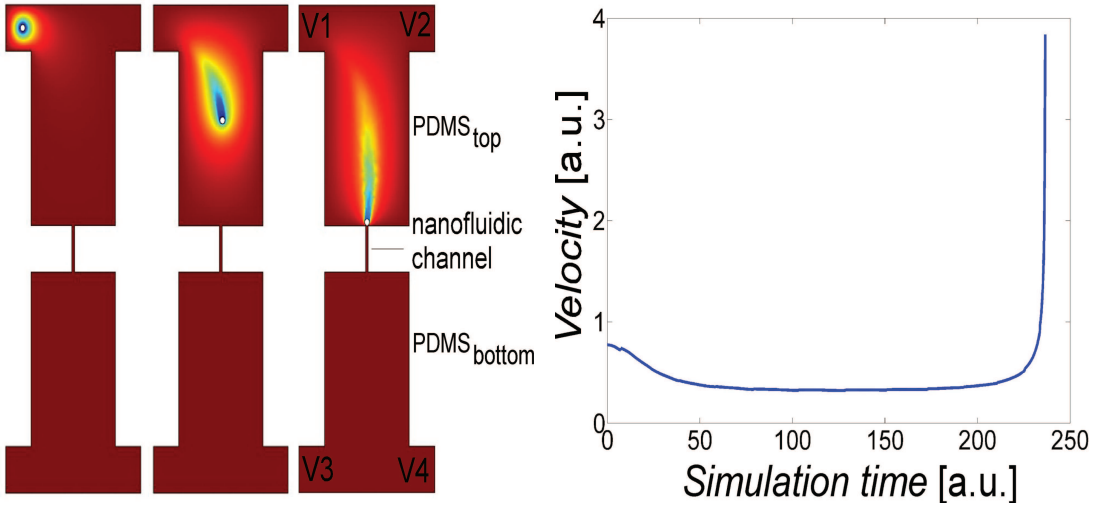

(a) (b)

Figure 5.2: (a) A moving mesh FEM simulation of the particle motion when V4 is connected to a positive voltage, V1 is grounded, and V2 and V3 are disconnected. (b) The normalized (to the unbounded medium) particle velocity of a 200-nm diameter particle with experimental parameters.

correspond to those used in the experiment: the radius of the nanoparticle was 100 nm; the radius of the nanochannel ranged from 25 nm to 75 nm; the zeta potentials of the nanoparticle and PDMS are -30 mV and -82 mV, respectively[1] [127]; the density of the fluid and nanoparticle are 1000 kg m^{-3} and 1050 kg m^{-3}, respectively; the conductivity of the 10 mM phosphate buffer saline (PBS) solution is 1.59 S m^{-1}. (A higher molarity of the PBS solution will result in a higher conductivity with a subsequent decrease in the required voltage to control the flow of

[1]Although negative charged particles were used in the experiment, positive charged particles could easily have been used. The only change would be reversing the polarity of the electrodes.

the nanoparticle. However, for most biological applications, 10 mM (or 1X) PBS is used since a higher molarity may not be biocompatible; therefore, 10 mM was used in the experiments. Although we only used 200-nm nanoparticles in our experiments, the new concept can work with sizes smaller than 100 nm as verified with simulations.)

5.4 Fabrication of multilayer architecture

In order to realize the above simulated platform and the schematic concept illustrated in Figure 5.1a and b, a multilayer fabrication process was created, in which the nanochannel layer is sandwiched between the microchannel layers made of polydimethylsiloxane (PDMS) polymer that are patterned using standard soft lithography with channel widths ranging from 50 - 150 µm and a channel depth of approximately 40 µm. The nanochannels are made from a photoresist layer, SU8, through a cost-effective holographic lithography technique, in which the nanochannels are formed by multiple laser exposures. The size of the nanochannels can be controlled by changing the exposure dosages or oblique sputtering after photoresist development [128, 129]. For the multilayer platform, the seamless bond between adjacent layers need to be guaranteed. PDMS can firmly bond to a Si-based material due to the -Si-O-Si- bond. Since SU8 does not adhere well to PDMS, a silicon dioxide adhesion layer (∼1 nm) was first deposited onto the nanochannel array at an oblique angle. Silicon dioxide was chosen since not only does it adhere well to SU8, but also it is a dielectric and will not affect the electrostatic fields applied across the layers to control the flow of the nanoparticles.

Figure 5.3 illustrates the fabrication procedures of our platform. A standard microscope glass substrate was cleaved and divided into four smaller pieces and then cleaned using piranha solution at 300 ° C for an hour. An antireflection coating (WiDE-15B, Brewer Science) was then spun at 3000 rpm for 30 s onto the substrate and baked for 30 min at 185 ° C. A sacrificial layer, Omnicoat (from MicroChem), was next spun and baked. SU8-2002 photoresist (from MicroChem) was then spun at 3000 rpm for 30 s and baked for 20 min in an oven at 95 ° C (Fig-

ure 5.3a). The nanohole pattern was then exposed using two-beam interferometric holographic lithography technique, as was discussed in Chapter 3. An UV laser beam (Innova 300, Coherent Corp.) was spatially filtered, expanded, and beam-splitted into two paths. The two identical beams were incident at an angle onto the photoresist-coated substrate, which was mounted onto a computer-controlled piezoelectric stage. The periodicity of the nanohole pattern is determined by the angle of incidence of the two beams and the laser wavelength. Two exposures are needed to fabricate the nanohole pattern: the first exposure creates a 1-D grating, then the stage is rotated 90 degree before the second exposure of equal time to form the 2-D nanohole pattern. The substrate was post-exposure baked (PEB) for 1 min at 95 °C and then developed with SU-8 developer (from MicroChem) for 3 min. The nanohole size is determined by the exposure time as well as the development time.

Figure 5.3b shows the deposition of SiO_2 as an adhesion layer at an oblique angle using the RF cathode of Discovery 18 (from Denton Vacuum LLC) as the stage was rotated. The SiO_2 surface was then bonded to the bottom PDMS microfluidic chamber (Figure 5.3c). Subsequently, in Figure 5.3d, the device was put into Microposit MF319 developer solution (from Rohm Haas) to remove the sacrificial Omnicoat layer from the glass substrate to form the nanochannel membrane. Next, SiO_2 is deposited onto the top surface of the nanochannel membrane before bonding it to the top PDMS microfluidic chamber (Figure 5.3e), where a concave aperture is made to fit a microscope objective in a multi-step PDMS curing process. The microchannels in the top PDMS layer are aligned orthogonal to the microchannels in the bottom layer (Figure 5.3f).

The cross-section of the multilayer device was taken with a scanning electron microscope (SEM) after it had been cut in halves to expose the nanochannel membrane connecting the microchannels from the top to the bottom layer. Figure 5.4a shows the four microchannels on the top PDMS layer, while Figure 5.4b is a close-up of the membrane in one of the microchannel, revealing completely developed nanochannels. Figure 5.4c shows one of the bottom horizontal microchannels orthogonal to the four top channels, while Figure 5.4d shows the suspended

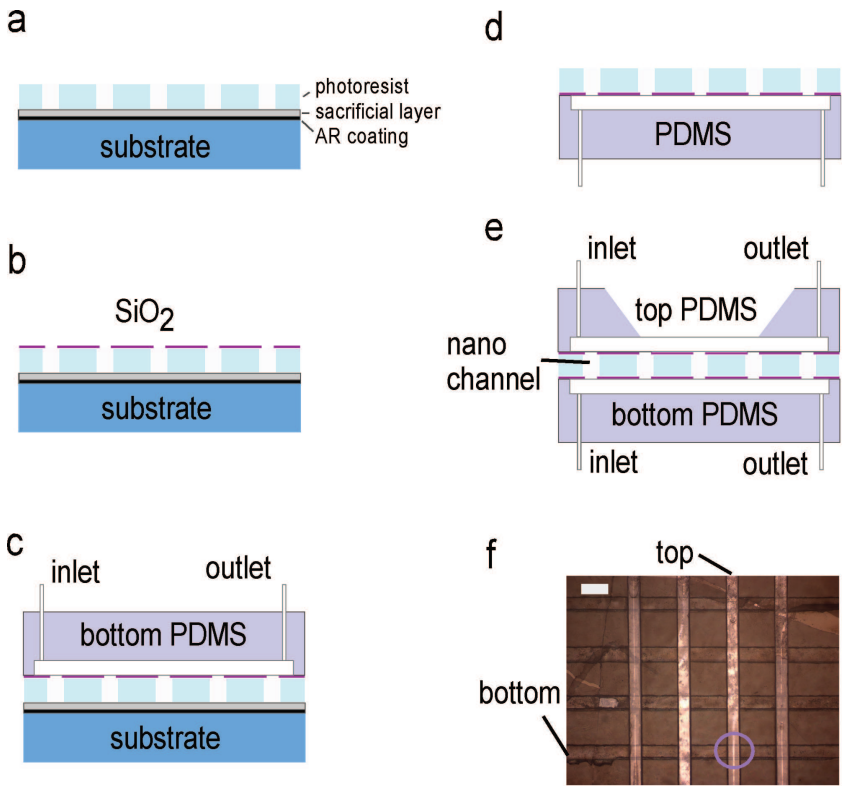

Figure 5.3: Fabrication Process Overview: (a) Nanochannel fabrication involves spinning a antireflection (AR) coating, a sacrificial layer, and SU8 photoresist on a clean microscope slide before using holographic interferometric lithography to expose the nanoholes. (b) SiO_2 is then sputtered at an oblique angle as an adhesion layer (c) The surface is then bonded to the bottom PDMS microfluidic chamber with inlet and outlet. (d) The sacrificial layer is then developed to release the nanohole pattern from the glass substrate to create the nanochannel membrane with thickness of 2 µm. (e) Another adhesion layer is sputtered on the top membrane surface before bonding the top PDMS microfluidic chamber (with a concave aperture for the microscope objective) to the membrane. (f) In the center of the multilayer device, four microchannels (vertical) are in the top layer and four microchannels (horizontal) are in the bottom layer. The circled area denotes a node of this intersection between the top microchannel, the nanochannels in the membrane, and the bottom microchannel. The scale bar shown is 200 µm.

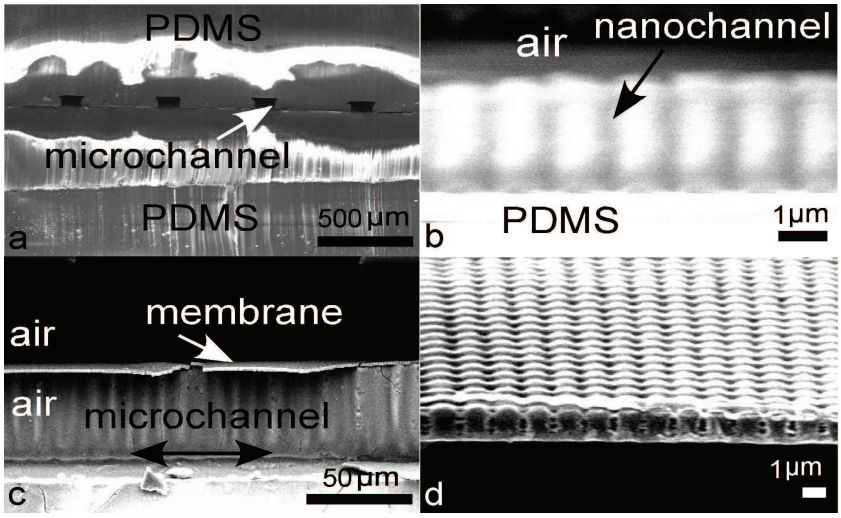

Figure 5.4: Cross-sectional SEM of the multilayer chip (a) shows the 4 microchannels on the top PDMS layer. (b) shows the nanochannel membrane inside one of the microchannel on the top layer. (c) shows one of the microchannel on the bottom layer with horizontal channel length in the diagram. (d) shows the membrane suspended in air with visibility of the cross-section of the nanochannel.

nanochannel membrane with its cross-section revealing the nanochannels.

5.5 Fluidic experiment

Low concentrations of beads (2.285 x 10^9 particles / mL of 10 mM phosphate buffered saline (PBS) solution, pH level of 7.0) were used during the experiment. Our experimental setup is shown in Figure 5.5a. The microscope objective fits inside the concave aperture on the top PDMS chamber whose thickness at the center was made as thin as possible (thin enough to be within the working distance of a 40X objective) as shown in Figure 5.5b. Figure 5.5c depicts the nanochannel membrane after being transferred onto the bottom PDMS layer. Initially, the nanoparticle solution and PBS solution were flown into the inlets of the top and bottom PDMS chambers, respectively, using electrical syringe pumps (Nanojet N5000, Chemyx Corp.). The pressure difference between the top and bottom microchannels was kept the same to ensure that no significant pressure was applied on the nanochannel membrane to prevent membrane deformation. First, large bead

(1-2 µm) solution (from Duke Scientific) was introduced into the top microfluidic chamber and monitored via a CCD camera to check the integrity of the multilayer platform. The flow rate was set such that a single particle flow could be observed with a 40X microscope objective by adjusting the pumping pressure. After confirming the integrity of the multilayer platform, pressure pumping was replaced with voltage control on the inlets and outlets for both lateral and transverse flow by adjusting the voltage potential between the inlet and the outlet, V1 versus V2 and V3 versus V4. Nanoflow was generated by applying a voltage between the inlet on the top channel (V1) and the outlet on the bottom channel (V4). The microparticles were observed to have slowed down, captured onto the nanochannel membrane, or released from the membrane by adjusting the strength of the voltage potential. Then, the reservoir connected to the top microchannel was changed to 200-nm carboxylated fluorescent nanoparticle solution (FluoSpheres, Life Technologies). We used fluorescent beads as nanoparticles for ease of observation. The nanoparticle's motion was captured using a high-speed camera (iXon, Andor Corp.). The fluorescent beads were excited using an argon laser (Innova 70, Coherent Corp.) under transmission mode. A long-pass filter (HQ545LP, Chroma Corp.) was used in the microscope turret to allow only the fluorescent emission wavelength to reach the camera. The thickness of the top PDMS layer within the concave aperture precluded the use of a higher magnification microscope objective to observe the movement of these 200-nm nanoparticles except for blurry out-of-focus images. It was difficult to fabricate the top PDMS layer to be sufficiently thin such that it would be within the working distance of a higher magnification objective while simultaneously be sufficiently thick to support fluidic flow when the PDMS layer is bonded onto the surface of the nanochannel membrane.

Thus, in order to evaluate the performance of real-time manipulation of these nanoparticles, high-resolution images of the manipulated nanoparticle pattern need to be taken. Thus, the multilayer device must be dismantled while keeping the trapped nanoparticle pattern intact. This process involves slightly increasing the pumping pressure in the top microchannel while maintaining the voltage between V1 and V4 until all the solution in the reservoir is out of the top

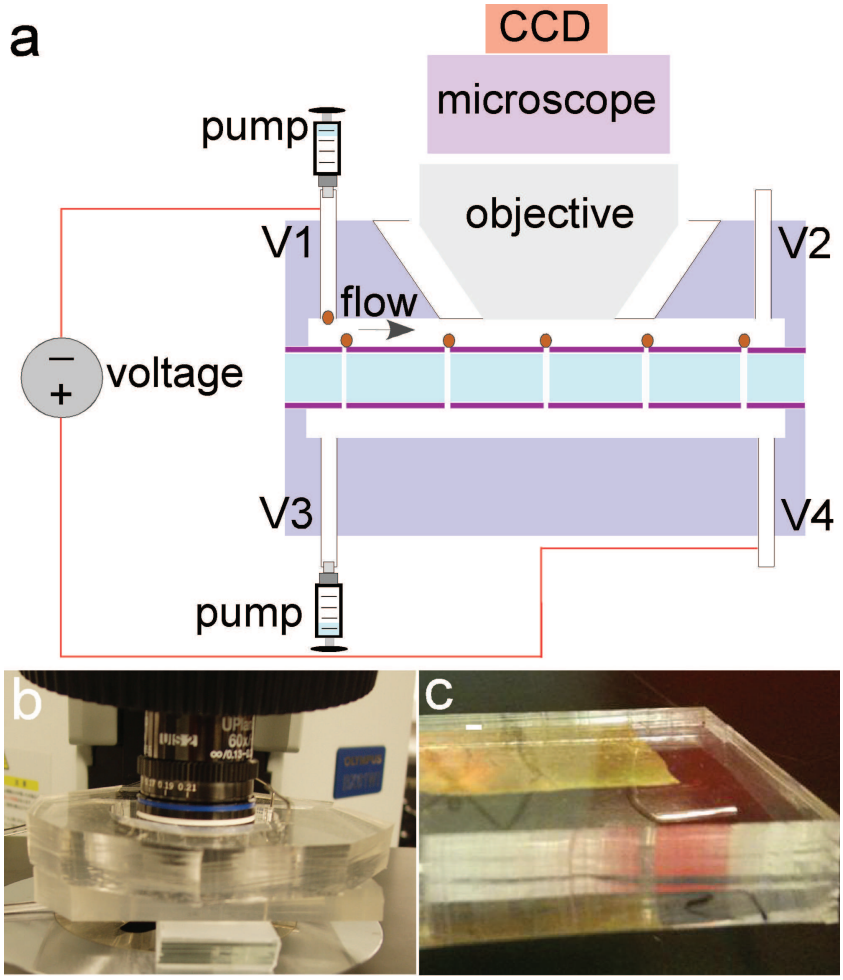

Figure 5.5: (a) Experimental setup of the multilayer nanophotonic chip using electrical syringe pumps initially for microflow, then switching to voltage control for nanoflow. The electrodes are labeled as V1, V2, V3, and V4. (b) The microscope objective fits inside a concave aperture in the top PDMS chamber, where the thickness at the center is within a 40X objective's working distance. (c) The nanochannel membrane after it has been transferred onto the bottom PDMS chamber is very smooth and uniform.

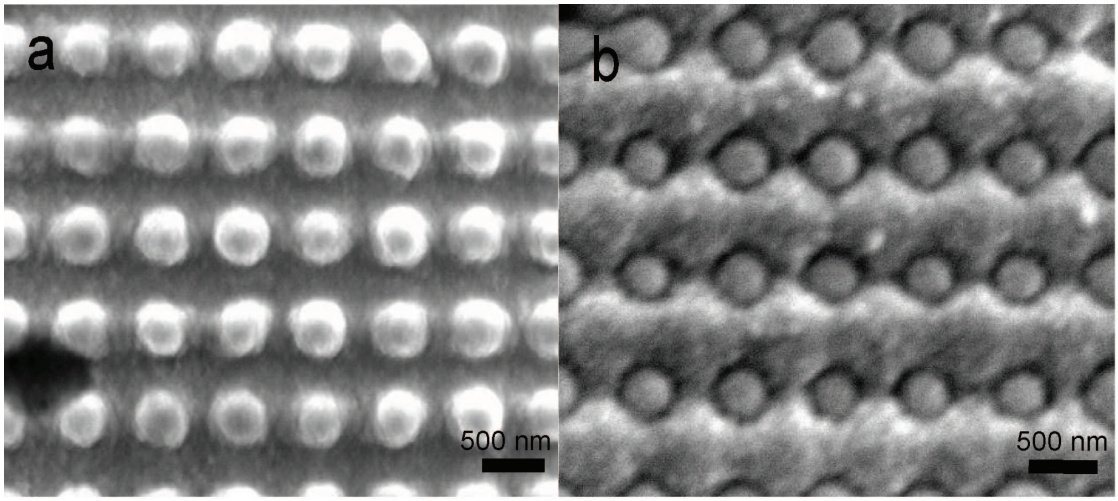

Figure 5.6: (a) 200-nm nanoparticles were captured onto the underlying 600-nm-pitch nanochannel array after a voltage was applied to form a 2-D nanophotonic nanoparticle array. The size of the nanochannels is estimated to be approximately 50 nm so the nanoparticles are on the surface of the nanochannels. (b) The size of the nanochannels is estimated to be approximately 150 nm so the 200-nm nanoparticles are mostly inside the nanochannels.

channel outlet. Then the inlets and outlets were disconnected and the top PDMS layer was carefully peeled off. Gold was sputtered onto the nanochannel membrane with the trapped nanoparticles prior to SEM imaging. Figure 5.6a and b depict the manipulated 200-nm nanoparticles onto the underlying two-dimensional (2-D), 600-nm periodic nanochannel pattern, yielding a periodic nanoparticle array.

The above results demonstrate the feasibility of our multilayer, nanophotonic chip approach in an aqueous environment, whose properties (e.g. transmission peak, effective index) can change depending on the underlying nanochannel pattern, the size and the number of nanoparticles or biomolecules, and their refractive indices. For example, in Figure 5.6a, the nanoparticles are on the surface of the nanochannels, whose size is approximately 50 nm in diameter; while in Figure 5.6b with nanochannel size of approximately 150 nm in diameter, the nanoparticles are trapped mostly inside the nanochannels. Consequently, the effective index is different for these two nanoparticle arrays. Analogous to the design of photonic crystal structure with defect states to tailor the effective index to produce photonic bandgap, the same concept can be applied in designing complex nanoparticle

structures.

The real-time manipulation depends on the effective control of the nanoflow into the nanochannel with an applied electric field and the microflow into the microchannels with pressure gradient. To clearly observe the real-time manipulation of nanoparticles (200 nm or smaller), an advanced soft fabrication process of the top PDMS layer needs to be developed to accommodate higher magnification objectives (e.g., 100X). In this study, 2-D nanohole was chosen to form a 2-D nanoparticle array, yet the technique described here can be used to design other functional patterns such as plasmonic nanoparticle clusters for tailored electric and magnetic resonances [130], efficient nanolenses with progressively decreasing nanosphere size and separation [131], 1-D nanoparticle structures for biosensing and electromagnetic propagation applications [46, 62, 132] and individually addressable nanoparticle array.

5.6 Summary

In this chapter, a fabrication process of a multilayer, nanofluidic platform for real-time manipulation and assembly of nanophotonic structure was presented. We employed electrokinetic forces to induce nanoflow in the nanochannel of the suspended membrane to self-align nanoparticles onto the underlying nanochannel pattern. To demonstrate the feasibility of the concept, we have manipulated and captured 200-nm nanoparticles to form a 2-D nanoparticle array with a 600-nm periodicity. The size of the nanochannel dictates what percentage of the nanoparticle's surface area is inside the nanochannel and thus, it will affect the effective refractive index of the structure. It is envisioned that this concept can be extended to control individual nanoparticle, biomolecule, or quantum dot underneath a more complex nanochannel and electrode pattern to form functional nanophotonic and nanoplasmonic structure. Thus, unlike previous static techniques, the approach described in this work can be used to monitor and control nanostructures in an aqueous, biocompatible environment in real time and *in vivo*, for applications ranging from targeted drug delivery to construction of nanophotonic devices.

5.7 Acknowledgement

Chapter 5, in part, is a reprint of the material as it appears in Small 2011. The dissertation author was the primary investigator and author of this paper. The co-authors listed either helped or supervised the research.

Chen, H. M.; Pang, L.; Gordon, M. S.; Fainman, Y., *Small*, 7, 2750-2757, 2011.

Chapter 6

Controllable orientation of nanotorch structures leading to uniform surface enhanced Raman scattering detection

As was introduced in Chapter 2, surface enhanced Raman scattering (SERS) substrates can increase the Raman signals by a few orders of magnitude so ultra-low concentration of analyte can be detected. Even single molecule detection has been reported, although its practical implementation still has not been proven. For successful commercialization, the SERS substrates not only need to produce high enhancement factor, but more importantly, produce uniform and consistent Raman signals across their surface areas over many measurements. In this chapter, we introduce a variant of the nanocrescent structure.

Nanocrescent-like structures have become important SERS structures because instead of relying on a few nanometer gap inter-particle plasmonic coupling to achieve local field enhancement, intra-particle plasmonic coupling between the cavity modes and the tip edges are utilized to achieve high local field enhancement at the tips. Unlike previous efforts, our fabrication approach creates 'nanotorch' structures with controllable cavity rim opening and deterministic ori-

entation to yield uniform Raman measurements, consisting of three-dimensional upright-oriented nanocrescent structures resting on nanopillars. Each structure serves as a single SERS substrate. We demonstrate that a nanotorch with a smaller rim opening results in a higher enhancement factor compare to one with a larger opening. More importantly, the uniformity of all the analyzed Raman modes of benzenethiol is better than 80% due to the consistent, upright orientation of each single nanotorch SERS substrate.

6.1 Introduction

Surface enhanced Raman scattering detection has gradually become a powerful tool from material identification to single molecule detection. However, fabrication of new SERS substrates is still heavily investigated due to two unsolved issues: achieving high local field enhancement (LFE) while simultaneously giving high repeatability. Solving this will be crucial for commercialization of SERS substrates. Nanoparticle was first used as a SERS substrate, but was soon replaced by nanoparticle assembly offering higher LFE at the interstitial sites due to coupling between particles. However, the random locations of the hot spots made the substrate impossible for quantitative analysis of the reagents. Other approaches were pursued; electron beam lithography and focused ion beam were employed to fabricate finely defined nanostructure, such as the bowtie structures for high LFE at the tips [133], but high cost and the planar methodology would prohibit successful commercialization. Subsequently, researchers have studied multiple resonance coupling of nanocrescent or half-shell structure [58, 59, 134–139] (where coupling among tip-to-tip, tip-to-cavity, cavity-to-body are involved), of the ring and disc structure [140] (where coupled multiple dipoles are involved), and of the composite nanocrescent and disc structure [141] (where dipole to quadruple coupling are involved). Nanocrescent has become a useful SERS structure because it is one of the most structurally and optically tunable anisotropic metal nanostructure. Unlike structures that rely on a few nanometer gap inter-particle plasmonic coupling to achieve high LFE, the nanocrescents are fabricated from relatively large sacrificial

nanoparticles with diameters of a few hundred nanometers. The nanoparticle size can be used to tune the plasmonic resonance.

It was shown in two-dimensional (2-D) nanocrescents that decreasing the tip distance will localize the field to a smaller volume and therefore increase the value of its complex amplitude [134, 135]. However, such field localization and enhancement have not been demonstrated experimentally for three-dimensional (3-D) nanostructure to fully realize the different types of coupling, especially the tip-to-tip coupling of a small gap. Most importantly, the orientation control of 3-D nanocrescent that is required for high SERS repeatability has not been demonstrated, especially when used as a single SERS substrate.

Here, we demonstrate a new variant of the nanocrescent, the 'nanotorch' structure, yielding smaller tip-to-tip spacing (in 3-D, smaller rim diameter) with higher LFE. Furthermore, unlike previous 3-D nanocrescent fabrication method that yielded randomly oriented nanocrescent structure, we demonstrate a fabrication method where the nanotorches are upright on their carrier substrate with controllable rim diameter and deterministic orientation. These nanotorch structures are beneficial for biosensing application, because they induce the maximum LFE for normal photon incidence and yield repeatable Raman measurement with less than 20% standard deviation. This will not only improve the limit of detection, but also increase the spatial resolution of SERS detection when the nanotorches are arranged in a periodic array, greatly impacting applications ranging from single molecule detection to *in vivo* diagnosis.

6.2 Finite Element Simulation

We investigated the nanotorch structure with full 3-D finite element method (FEM) simulations. The time-harmonic Maxwell equations of the 3-D model are solved over the domain of interest, which reduce to the Helmoholtz equations. Low-reflection, absorptive perfectly matched layers (PMLs) were applied on the exterior layers to eliminate non-physical reflections at the boundaries [142]. The scattering boundary condition was used for the incident electric field with a magni-

tude of 1 V/m polarized along the x-direction. Adaptive meshing was employed to automatically reduce the mesh element size near geometric edges that are rapidly changing within the structure until the maximum field converged. The reported wavelength-dependent refractive index of bulk gold was used [27]. The enhancement factor is calculated from the amplitude ratio of the near-field of the nanotorch and the incident electric field, where the highest value occurs on the rim. Symmetry plane was used in the simulation to reduce the computation time. Only half of the nanotorch is shown in Figure 6.1 to better reveal the cross-section of the rim and the nanotorch shape. The pillar is depicted in the figure with dash lines. The nanotorch is composed of a nanocrescent structure on top of a pillar with a refractive index of 1.47. A planar nanocrescent model was first formed by subtracting an inner circle with a 150-nm radius, offset from the center by 50.5 nm, from an outer circle with a 200-nm radius, yielding a nanocrescent with a thickness of ∼100 nm. A fillet with a radius of curvature of 1 nm was used on the tip of the nanocrescent to better represent the fabricated structure. Only one half of the nanocrescent is used. A 100-nm wide by 200-nm tall rectangle was added below the halved planar nanocrescent to represent the pillar. The 2-D composite structure was then revolved 360 ° around the z-axis to form the 3-D nanotorch structure with a rim opening of 140 nm.

The plasmon resonance can also be tuned by varying the cavity offset of the inner dielectric sphere (i.e., air in the simulation). Changing the offset will invariably affect the rim diameter and the thickness. In planar 2-D nanocrescent structures, this translates to tip-to-tip distance and as the offset decreases, the dipole-like coupling increases between the tip, resulting in increased magnitude of the resonance as demonstrated experimentally [134, 135]. For our 3-D nanotorch simulations, the offset and thickness were keep constant. To introduce larger rim opening, the planar nanocrescent was truncated before the 360 ° revolution in the model. The same 150-nm and 200-nm radii circles were used with the same offset. The planar structure was truncated to create an opening of 130 nm (in radius) and then 1 nm fillet was performed at the tip. After 360 ° revolution, a 3-D nanotorch with a rim opening of 260 nm was simulated using adaptive meshing. In the first

case of a nanotorch with a rim opening of 140 nm (as shown in Figure 6.1), a maximum electric field of 45 V/m at the rim was achieved with ∼400K meshing elements. This is in contrast to a lower value of 29 V/m for the 260-nm rim opening case with ∼610K meshing elements, as shown in Figure 6.1b. The 260-nm opening has smaller amplitude compare to the 140-nm opening due to less plasmonic coupling between the cavity and the edges. We have also investigated different nanotorch sizes and found that the resonance peak is red-shifted as the size increases and the resonance is broaden, which is consistent with the size-effect seen in gold nanoparticles [56]. We found in the simulations that the nanotorch and the nanocrescent behave similarly in terms of the location and the magnitude of the maximum electric field being concentrated on the rim of structure. The maximum near-field increases significantly as the fillet radius decreases, especially below 1 nm. Increasing the sharpness of the tip (rim) will increase the lightning rod effect but has little effect on the dipole-like coupling between the tips and cavity [139]. For a fillet radius of 0.25 nm and a correspondingly smaller rim diameter of 72 nm, the total adaptive meshing element count is ∼770K elements with a maximum electric field of 190 V/m. However, a fillet of 1 nm was chosen in

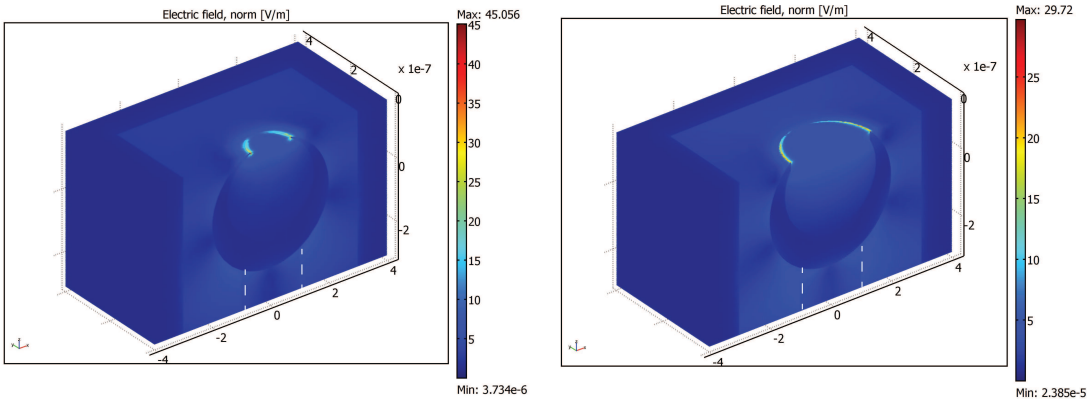

(a) (b)

Figure 6.1: 3-D FEM simulation of the nanotorch structure comprising of a 100-nm-thick gold nanocrescent on top of a 200-nm pillar (depicted with dash lines). A fillet with a 1-nm radius was applied to the tip. Only half of the structure is shown to better reveal its cross-section. (a) A smaller rim opening of 140 nm. (b) A larger rim opening of 260 nm.

our simulations to better represent actual fabricated structures instead of trying to report the highest maximum field with the unrealistic 0.25 nm fillet for fabricated structures.

The far-field absorption, scattering, and extinction cross-section of the nanocrescent was simulated in COMSOL Multiphysics in the spherical coordinate system. The absorption cross section is calculated from the time average resistive heating of the gold nanocrescent structure, $\frac{1}{2}\mathrm{Re}[\sigma\mathbf{E}\cdot\mathbf{E}^* - j\omega\mathbf{E}\cdot\mathbf{D}^*]$, normalized to the input power. The extinction cross-section is calculated through the imaginary part of the forward scattering cross section using the optical theorem represented by

$$-\frac{\pi}{4}k_{\mathrm{o}}\frac{\mathrm{Im}(E_x^{far})\cdot 1[\mathrm{m}]}{E_{\mathrm{o}}} \tag{6.1}$$

where E_x^{far} is the x-component of a 500-nm-radius spherical integration boundary surface and [m] is the unit meter to balance out the units. The far field can be calculated from the near field using the Stratton-Chu formula [143, 144]. The scattering cross-section is simply the subtraction of the absorption cross-section from the extinction cross-section. The boundary of the simulation domain is surrounded with a spherical perfectly matched layer (PML) to absorb non-physical scattered light and the scattering boundary condition was used to prevent reflections. Figure 6.2a and Figure 6.2b show the spectra for 140-nm opening and 260-nm opening, respectively. The peak of the extinction is slightly red-shifted for the larger opening.

Plots of the near-field versus wavelength at a single point on the rim of the nanocrescent are shown in Figure 6.3a and Figure 6.3b for the 140-nm opening and 260-nm opening, respectively, with the peak wavelengths are at 790 nm and 750 nm respectively. The surrounding media is taken to be air and the simulation was done in the spherical coordinate system. For the nanotorch structure with a 200-nm-diameter pillar with a height of ∼200 nm and a refractive index of 1.47 resting on a silicon substrate (n=3.69), the peak of the maximum near-field is blue-shifted and broadened for both 140-nm opening and 260-nm opening as shown in Figure 6.3c and Figure 6.3d, respectively. The dimension of the nanotorch would

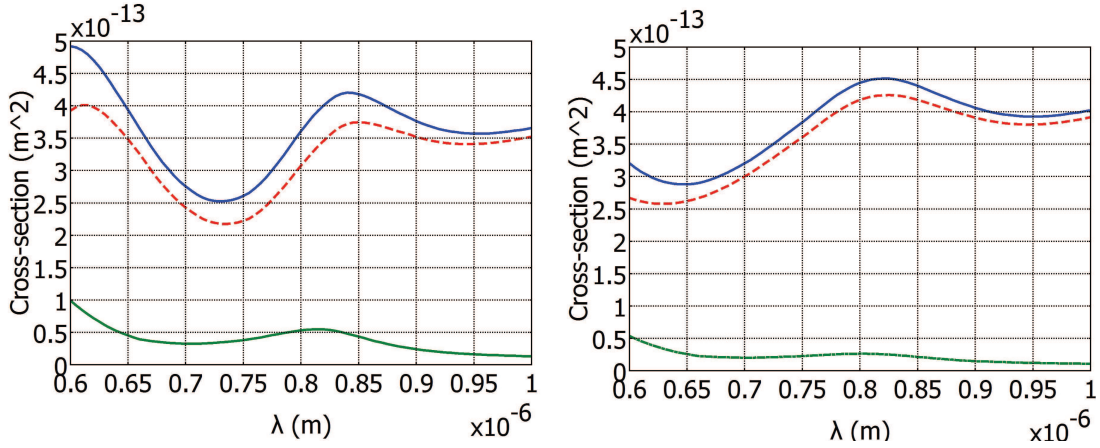

(a) 140-nm rim opening

(b) 260-nm rim opening

Figure 6.2: Cross-section calculations of the nanocrescent a) 140-nm-opening upright nanocrescent b) 260-nm-opening upright nanocrescent. Blue solid line is extinction, red dash line is scattering, and green solid line is absorption.

need to be changed in future design to better align the peak wavelength to the excitation wavelength of the laser.

6.3 Proposed concept

Lu *et al.* had previously fabricated nanocrescents with the substrate placed above the sputtering cathode at a tilt angle of ∼30 degree as the substrate was rotated [58]. Here, we analyze two sputtering setups for our sputtering machine. The first is analogous to their setup except that the substrate was placed on a horizontal rotating stage below the sputtering cathode at an angle of $\theta \sim 30$ degree, as shown in Figure 6.4a. The opening of the nanocrescent is calculated to be $d = r \cdot (sin\beta)$, Figure 6.4b, where for a 150-nm-radius nanoparticle and β of 60 degree, the rim opening is 2d = 260 nm. In this setup, as well as in Ref. [58], the nanoparticles rest on top of a horizontal planar surface and because of the shadowing effect of the sputtering cathode onto the nanoparticles, it is not possible to fabricate nanocrescents with small rim opening.

The second fabrication setup is shown in Figure 6.4c with the nanoparticles resting on nanopillars. The substrate is secured on a custom-made, rotating

plate mounted onto a motor that is secured onto a goniometer to control the relative angle of incidence between sputtering cathode and the rotating stage. In the proposed setup, the goniometer is set to 45 ° so the entire surface area of the nanoparticles are coated with gold except for the small portion that are in contact with the nanopillars. The rim opening is dependent on the diameter of the nanopillar under the condition that the angle α is larger than θ, Figure 6.4d. By changing the goniometer angle, α, the ϕ angle is altered, which will affect the shape of the nanostructure. For $\phi = 0$, we could get nanoring-like structures, similar to

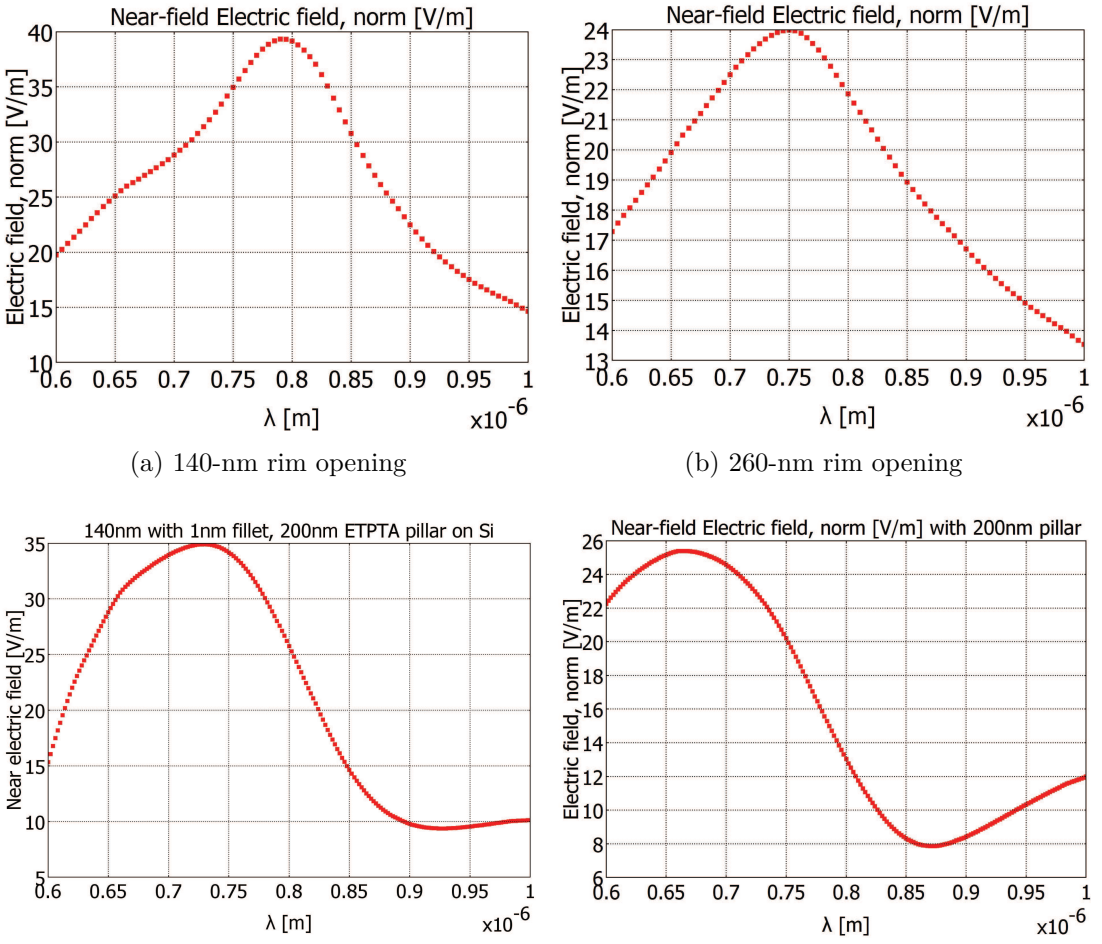

(a) 140-nm rim opening

(b) 260-nm rim opening

(c) 140-nm rim opening nanotorch

(d) 260-nm rim opening nanotorch

Figure 6.3: Near-field electrical field versus wavelength at a single point on the rim a) 140-nm opening nanocrescent b) 260-nm opening nanocrescent c) 140-nm opening nanotorch d) 260-nm opening nanotorch

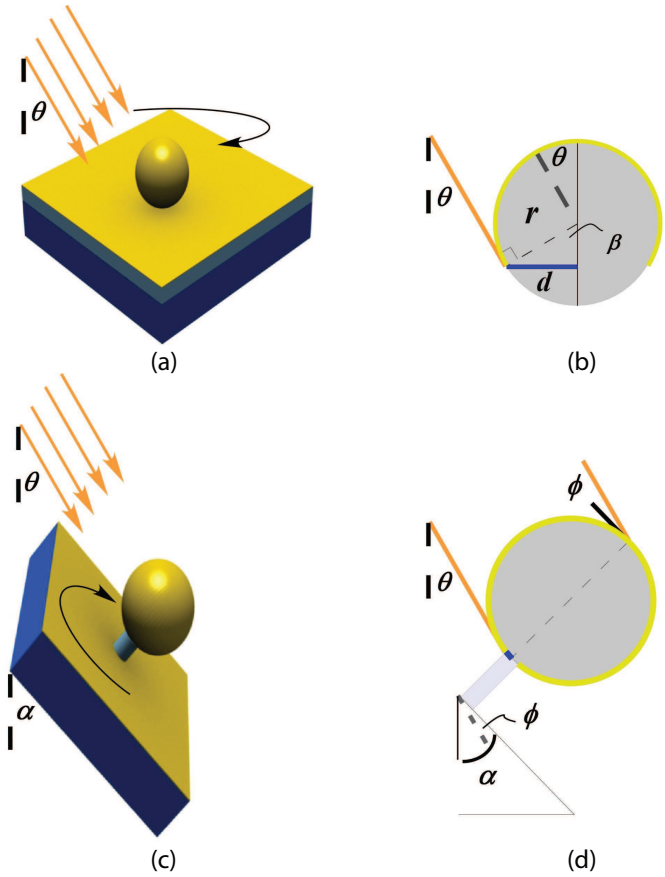

Figure 6.4: a) Metal deposition setup for nanocrescents with large rim opening. b) Geometrical schematic of the traditional fabrication method with the opening given by 2d. c) Metal deposition setup with a nanoparticle sitting on a nanopillar mounted on a goniometer for fabricating nanotorch structure with controllable rim opening and deterministic orientation. d.) Geometric schematic of the proposed deposition process where the opening is determined by the diameter of the nanopillar.

Ref. [145].

6.4 Fabrication process

Silica nanoparticles were used as sacrificial templates for fabricating these upright nanotorches. Specifically, 310-nm silica nanoparticles (from Bangs Laboratory) were made into 0.002% solution with 18 MOhm purified water (from ThermoScientific Barnstead Nanopure System) with a 0.001% of surfactant (Tween 20,

from SigmaAlrich) to prevent coagulation. The nanoparticle solution was diluted to ensure isolated nanoparticle in order to analyze the SERS effect on an individual nanotorch. BK7 microscope slides (or silicon wafers) were diced, cleaned with piranha solution and DI water, and then dried with nitrogen. Subsequently, poly-(methyl methacrylate) (PMMA) A4 photoresist (from MicroChem) was spun at 4000 rpm for 45 sec onto the sample substrate and baked for 1 min at 180 ^{o}C on a hotplate. The sample was then dipped vertically into the silica nanoparticle solution for 30 sec and then brought up slowly. As water molecules evaporate from the surface, randomly distributed and isolated nanoparticles were dispersed onto the substrate (Figure 6.5a). It was found experimentally that this technique provided much better dispersity than spin coating technique. The samples were then mounted onto a custom-made rotating stage which was secured onto a goniometer stage as discussed previously. Reactive ion etching (RIE) was then used to create nanopillars in which the silica nanoparticles act as the etching mask, as shown in Figure 6.5b and also in Figure 6.6a of a scanning electron microscopy (SEM) image. The girth of the nanopillar can be adjusted by varying the etching condition. Nanopillars as small as 50-nm-diameter have been demonstrated using the Oxford PlasmaLab 80 RIE machine. The nanopillar will subsequently dictate the opening of the nanotorch together with the sputtering setup. An adhesion layer of chromium ($\sim$1 nm) was then sputtered onto the nanoparticles with a goniometer angle (α) of 45 ^{o} using the Denton Discovery 18 sputter. Subsequently, gold thickness of 100 nm was sputtered, followed by another sputtering step of chromium ($\sim$2 nm) to protect the gold material during a later RIE etching process to create the nanotorch pillar (Figure 6.5c).

Diluted ethoxylated trimethylolpropane triacrylate (ETPTA) monomer (SR-415, Sartomer Inc.) was then mixed with 20% (2-hydroxy-2-methyl-1-phenyl-1-propanone) photoinitiator (Darocur 1173, BASF Corp.) and then spun onto the metal-coated silica nanoparticles and slowly ramped up to embed the nanoparticles inside this monomer layer. The sample was then polymerized with the UV light source of a mask aligner (MA6, Karl Suss), as shown in Figure 6.5d. A clean silicon substrate was then primed with (3-acryloxypropyl) trichlorosilane (APTCS) from

Gelest Corporation for adhesion to the nanoparticle-embedded ETPTA sample. The two pieces were bonded and then baked on a hot plate at 60 °C for 30 min before peeling the two pieces apart (Figure 6.5e). After transferring to the silicon substrate, chromium and gold wet etchants were used to remove the metals on the surface of the monomer (Figure 6.5f). The metals on the nanoparticles are protected from this wet etching process since they are embedded inside the monomer. The sample was then RIE etched again to remove the ETPTA layer down to the nanoparticle-level to create nanocrescents (Figure 6.5g) by using the PlasmaLab 80 machine at 100 W with 40 sccm of O_2, 40 mTorr for 90 sec. To create the nanotorches, the etching time was prolonged to 3 min to form the nanopillars (Figure 6.5h). Lastly, the sample was dipped and agitated lightly for 3 min in a 4%

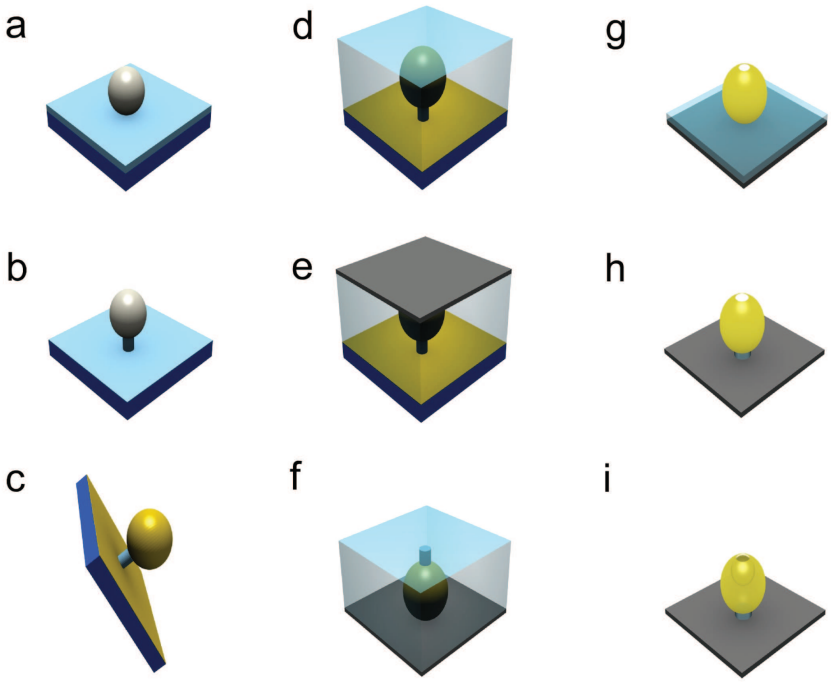

Figure 6.5: Fabrication Process. a) Silica nanoparticle on a photoresist-coated BK7 substrate. b) RIE etching to create nanopillar in order to fabricate nanotorch with small rim opening. c) Oblique metal sputtering using setup in Figure 2c. d) Embedding nanoparticle with ETPTA monomer. e) Binding to silicon wafer. f) After peeling and transferring to silicon wafer. g) RIE etching of ETPTA down to nanoparticle to create nanocrescent. h) Further RIE etching to create nanotorch structure. i) Dissolve silica sacrificial nanoparticle to create nanotorch.

diluted HF solution to dissolve the silica nanoparticles to produce these nanotorch structures (Figure 6.5i).

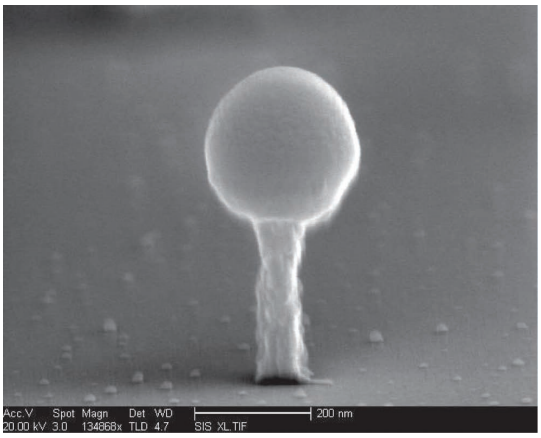

(a) nanoparticle on a nanopillar

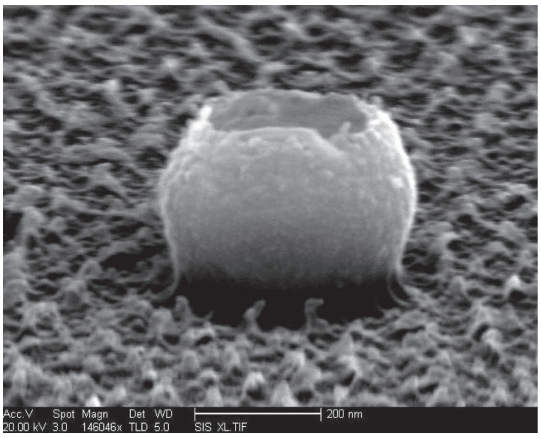

(b) 260-nm rim opening nanocrescent

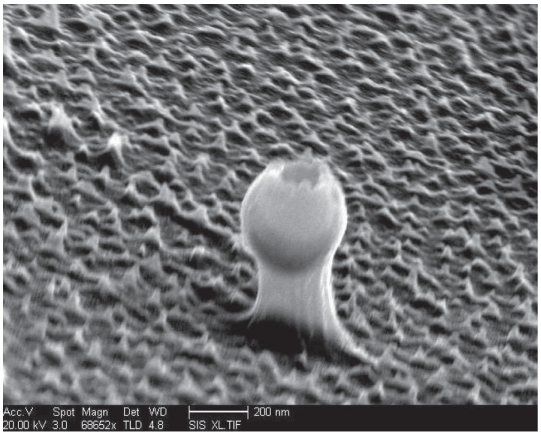

(c) 140-nm rim opening nanotorch

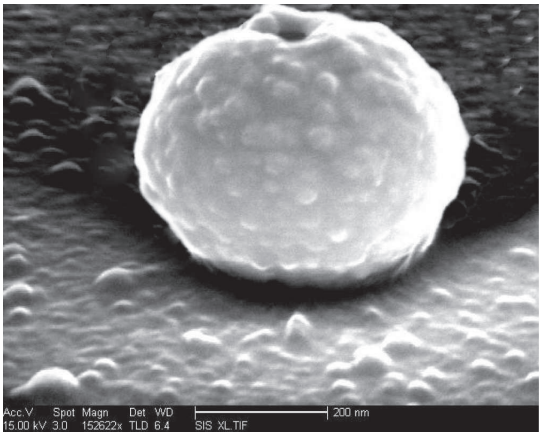

(d) 50-nm rim opening nanocrescent

Figure 6.6: a) After RIE etching of PMMA to create nanopillar where the silica nanoparticle acts as a etching mask. b) Upright nanocrescent structure with larger rim opening (∼260 nm) fabricated with the setup shown in Figure 6.4a. c) Upright nanotorch structure with smaller rim opening (∼140 nm) fabricated using the goniometer setup shown in Figure 6.4c. d) Even smaller rim opening (∼50 nm) has been demonstrated.

Before SERS characterization, chromium wet etching was done again to remove chromium from the nanotorch structure and expose gold to analyte adsorption. With the sputtering setup shown in Figure 6.4a, upright-oriented nanocrescents and nanotorches with large rim opening were fabricated as shown in Fig-

ure 6.6b with a nanocrescent with an opening of ∼260 nm. With the sputtering setup shown in Figure 6.4c and a goniometer angle α of 45 degree, upright-oriented nanocrescents and nanotorches with smaller rim opening were fabricated as shown in Figure 6.6c with a nanotorch rim opening of ∼140 nm. Using our new technique, we have demonstrated as small as ∼50-nm-diameter rim opening as shown in Figure 6.6d.

6.5 SERS measurements

For SERS characterization, a near infrared (NIR) 785-nm laser was used not only because it better matched the scattering resonance of the nanotorch but also because it can avoid the fluorescence from biomolecules. It has a deeper penetration depth in biological issues, and the low photon energy minimizes photothermal damage to biomolecules and cells [58, 146]. Moreover, by using a NIR source, it ensures that the detected SERS signal is from the nanotorch and not from a residual nanoparticle since the plasmon resonance of the nanoparticle can hardly be excited by a NIR source—a necessary condition for the effective near-field energy transfer to adsorbed molecules as manifested by the SERS enhancement phenomenon [147, 148]. Kneipp *et al.* had shown a SERS enhancement factor (EF) of $\sim 10^9$ by using a 830-nm laser on a cluster of nanoparticles [149]. However, due to the random particle aggregation, locating these hot spots in the interstitial spacing of the nanparticle cluster is unpredictable and non-uniform. In the case of the nanotorch, the SERS enhancement of each single nanotorch does not depend on the coupling between multiple nanoparticles but rather on the resonant coupling of the sharp tips, inner cavity edges and outer edges, making it an individual single SERS substrate.

Before SERS measurements, the substrates were treated with 5 mM of benezenethiol in 200-proof bioagent grade ethanol (from SigmaAlrich) for 3 hours and then rinsed copiously with ethanol three times and then carefully dried with nitrogen. Raman measurements were taken using the inVia Raman microscope system from Renishaw Inc. with a 785-nm excitation source. (Measurements were

also taken with a 532-nm source but no signal was detected, as expected, since there is no plasmonic resonance at that wavelength). At first, a coarse Raman image mapping was done on the sample using the built-in Raman imaging feature to ensure that we were looking at the nanotorch structure. Next, a 50X objective was positioned over the hot spot seen on the image mapping and several static measurements were taken on and around the hot spot by moving the position of the substrate incrementally to maximize the Raman signal to ensure that the laser beam is focused on the nanotorch. The SERS enhancement factor is given by

$$EF = \frac{I_{SERS}}{I_{neat}} \frac{N_{neat}}{N_{SERS}}, \tag{6.2}$$

where I_{SERS} and I_{neat} refer to the peak intensities from the surface-adsorbed and the neat (bulk) benzenethiol analyte, respectively, N_{neat} and N_{SERS} refer to the number of molecules interrogated on the neat benzenethiol and the SERS surface, respectively. N_{neat} is defined as

$$N_{neat} = \frac{\rho \cdot N_A \cdot n \cdot A \cdot h}{M_W}, \tag{6.3}$$

where ρ is the benzenethiol density, N_A is the Avogadro's number, M_W is the molecular weight of the compound, A is the waist of the interrogating beam and h is the confocal depth parameter [150]. The product of $A \cdot h$ represents the height of a cylindrical volume in which the signal generated by each neat benzenethiol molecule can be considered equal to the signal of a molecule found in the focal plane of the objective lens [151]. N_{SERS} is defined as

$$N_{SERS} = A \cdot F_{SERS} \cdot \mu_{SERS}, \tag{6.4}$$

where F_{SERS} is a ratio factor of the exposed SERS structure's surface area to the focused laser excitation. In our case, we assume that the exposed area is the hemisphere of a sphere with the equivalent radius of the nanotorch ($\sim$205 nm), where F_{SERS} is given by

$$F_{SERS} = \frac{2\pi}{\pi} \frac{r_{sphere}^2}{r_{beam}^2}. \tag{6.5}$$

If only one monolayer of benzenethiol exists on a flat gold surface, the surface coverage is equivalent to 0.6 nmol/cm^2 [152]. We have considered the Raman

intensities of the 1573 cm^{-1} band (C-C stretching mode) to calculate the approximate enhancement factor because of its appearance in both the neat and SERS spectra. It should be noted that for the neat spectrum, there is a slight shift for the neat Raman measurement to 1584 cm^{-1} [153]. The Raman spectra are shown in the bottom, middle, and top spectrum in Figure 6.7a for the neat benzenethiol (magnified 5 times), the nanotorch with a 260-nm opening, and the nanotorch with a 140-nm opening, respectively. The modes of the spectra correspond to those of published reports of benzenethiol adsorbed onto gold and the monolayer coverage of benzenethiol is confirmed by the absence of the C-S bond in the SERS spectra at around 2561 cm^{-1} (not shown) [154, 155]. No Raman signal was seen for measurement done on bare silicon sample sputtered with gold under the same sputtering condition. A conservative estimate of the enhancement factor is 8.2×10^6 for the 140-nm-opening nanotorch, which is ~6X higher than compare to the 260-nm-opening nanotorch with an enhancement factor of 1.5×10^6.

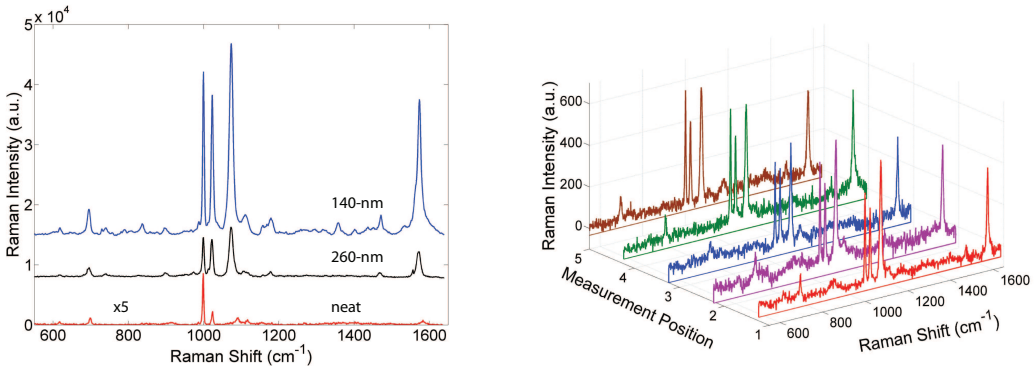

(a) (b)

Figure 6.7: a) The measured Raman signals for 140-nm opening nanotorch (top), 260-nm opening nanotorch (middle), and neat benzenethiol (bottom). b) A sample uniformity plot of 5 nanotorches at different locations within the same substrate.

More importantly, shown in Figure 6.7b is a waterfall plot of five Raman measurements of individual nanotorch at different locations within the sample. The standard deviations of the Raman intensity at each mode, shown in Table 6.1 corresponding to 1000 cm^{-1}, 1023 cm^{-1}, 1074 cm^{-1}, and 1573 cm^{-1}, are all calculated to be less than 20%. We attribute the uniformity of the Raman intensity to

the upright orientation of the nanotorches, and therefore, the consistent orientation of the incident field relative to the nanotorches. Previous fabrication method had yielded nanocrescents exhibiting different scattering spectra within the same substrate, in which the authors attributed to slight differences in the geometries and the orientations with respect to the incident light [58]. As a result of their fabrication method, the orientation of the nanocrescents varied. Since the near-field enhancement is largely influenced by the orientation of the incident field, the non-uniformity in their measurements was observed. Using our proposed fabrication method, the upright-oriented nanotorches yielded better than 80% Raman signal uniformity.

Table 6.1: The standard deviation of Raman intensity for benzenethiol adsorb onto gold nanotorch.

Peak [cm-1]	**Mode**	**Std. Dev.**
1000	ν(C-C-C)	20.0%
1023	(C-H)	12.3%
1074	ν(C-C-C) and ν(C-S)	12.6%
1573	ν(C-C-C)	16.5%

It is important to note that the enhancement factor calculation is a conservative estimate since it is assumed that the surface of the nanotorch is saturated with benzenethiol, which is probably not the case in the experiment. In addition, as can be seen from the FEM simulation, only the rim has high electrical field concentration and contributes to the enhancement effect. The percentage of concentrated electrical field on the rim relative to the total surface area of the nanotorch is 0.8 %. The total number of benzenethiol molecules contributing to the enhancement effect is estimated to be ∼15,000. (The surface area of the nanotorch with benzenethiol adsorbed onto gold is approximately that of an equivalent nanoparticle with a diameter 410 nm ($4\pi r^2 = 5.28 \times 10^{-9}\,\mathrm{cm}^2$). Assuming a decay length of 20 nm, the 140-nm rim diameter has an effective area of ($\pi[r_{outer}^2 - r_{inner}^2] = 4.4 \times 10^{-11}\,\mathrm{cm}^2$).

The total number of benzenethiol molecules contributing to the enhancement effect is estimated to be $4.4 \times 10^{-11}\,\mathrm{cm}^2 \times 0.6\,\mathrm{nmol/cm}^2 \times 6.02 \times 10^{23} =\sim 15,000$).

Further experiments are on-going to optimize the nanotorch geometry to yield even higher enhancement factor by changing the gold thickness, the rim opening, and the goniometer angle. As seen in Figure 6.3c and Figure 6.3d, the wavelength of the peak near-field is not exactly align to the laser wavelength. In the future, the nanotorch geometry should be designed to be better align to the laser wavelength.

Presently, we have fabricated 50-nm-diameter rim opening nanotorches, but challenges were encountered in keeping these structures upright consistently during the fabrication process as the nanoparticles tend to fall off the nanopillars during the fabrication process. Dip-coating and vapor deposition should be investigated to solve this issue to create even smaller rim diameter to achieve even higher enhancement factor. It is envisioned in the future that these nanotorch structures could be integrated into optofluidic chip such that biomolecules could be controlled onto the rims of the nanotorches via electrokinetic forces for maximum enhancement efficiency [156]. Furthermore, fabrication of periodic nanoparticle array have made significant progress recently [119, 156, 157]. By using these and other methods, fabrication of 3-D nanotorch array will yield even higher enhancement factor due to the coherent coupling effect of periodic array. Moreover, nanotorch array will increase the spatial resolution of SERS substrate, enabling SERS imaging and *in vivo* diagnosis.

6.6 Summary

Three-dimensional FEM simulations of nanotorch were performed and validated that smaller cavity rim opening will produce higher local field enhancement and thus higher SERS enhancement factor. We introduced a method of fabricating upright nanotorches with controllable cavity opening and deterministic orientation that yielded uniform Raman intensity of better than 80%, where each nanotorch serves as a single SERS substrate. Measurements confirmed that smaller rim open-

ing (140-nm diameter) yielded an enhancement factor of approximately 6 times higher than a larger rim opening (260-nm diameter). The higher enhancement factor of the fabricated 3-D nanotorch can be used for *in vivo* diagnosis to replace nanoparticle cluster for better limit of detection.

6.7 Acknowledgement

Chapter 6, in part, has been recently submitted for publication of materials, entitled, "Controllable orientation of nanotorch structures leading to uniform surface enhanced Raman scattering detection," H. M. Chen, L. Pang, A. King, G. M. Hwang, Y. Fainman. The dissertation author was the primary investigator and author of this paper. The co-authors listed either helped or supervised the research.

Chapter 7

Conclusion and future directions

7.1 Summary of contributions

Before my Ph.D. study, I have not even heard of plasmonics, let alone imagine that I would spend the next few years of my life being immersed in it and fascinated by its potential to impact our society. During the last few years, my main focus has been to combine different forms of plasmon resonances to improve the sensitivity of biological sensors, first through both finite difference time domain (FDTD) and FEM computer simulations. Then, the challenges came with bringing these concepts to life through cost-effective fabrication methods, hopefully without resorting to the expensive and serial process of electron beam lithography. As seen from the dissertation, we have introduced three unique platforms for surface plasmon resonance (SPR) sensing, nanoparticle control, and SERS detection.

In Chapter 3, I introduced a novel, low-cost and mass-producible fabrication method of large-area, composite three-dimensional metallodielectric nanostructure array, fabricated using two beam interferometric lithography and oblique gold sputtering. The ease of fabrication, reusablility, and reconfigurability are all advantages over conventional fabrication method of nanohole array. Furthermore, enhanced near-field resulting from coupling of SPPs and LSPs is beneficial to improving the limit of detection. As an application, the surface hydrophilicity of the gold nanostructure was analyzed experimentally using SPR technique by monitor-

ing the resonant wavelength shift in the absence and presence of a self-assembled monolayer.

In Chapter 4, the mushroom-like nanostructure was used for biological sensing, specifically the specific binding events between biotinylated-BSA and streptavidin protein was quantitatively measured and analyzed. Two channels were used in the setup for the signal and control channel to minimize environmental fluctuations. We quantified the limit of detection to be sub-nanomolar instead of tens of nanomolar with conventional nanohole array.

In Chapter 5, a fabrication process of a multilayer, nanofluidic platform for real-time manipulation and assembly of nanophotonic structure was presented. In addition, we introduced and employed electrokinetic forces, via voltage control, to induce nanoflow in the nanochannel of the suspended membrane to control and manipulate nanoparticles onto the underlying nanochannel pattern. To demonstrate the feasibility of the concept, we manipulated and captured 200-nm nanoparticles to form a 2-D nanoparticle array with a 600-nm periodicity. The size of the nanochannel dictates what percentage of the nanoparticle's surface area is inside the nanochannel and thus, it will affect the effective refractive index of the structure. It is envisioned that this concept can be extended to control individual nanoparticle, biomolecule, or quantum dot underneath a more complex nanochannel and electrode pattern to form functional nanophotonic and nanoplasmonic structure.

In Chapter 6, 3-D FEM simulations of nanotorch were performed and validated that smaller cavity rim opening will produce higher local field enhancement and thus higher SERS enhancement factor. We introduced a method of fabricating upright nanotorches with controllable cavity opening and deterministic orientation that yielded uniform Raman intensity of better than 80%, where each nanotorch serves as a single SERS substrate. Measurements confirmed that smaller rim opening (140-nm diameter) yielded an enhancement factor of approximately 6 times higher than a larger rim opening (260-nm diameter). The higher enhancement factor of the fabricated 3-D nanotorch can be used for *in vivo* diagnosis to replace nanoparticle cluster for better limit of detection.

7.2 Future directions

I hope that I have at least made a small contribution to this exciting field of plasmonics. Yet, this field is still at its nascent stage, so there are much more to be done to further improve the sensitivity and practicality of biological sensors. Here, I will briefly offer my outlooks.

7.2.1 Nanoresonator array with integrated fluidics

A potential sensor in the future could be an array of nanoresonators, such as the nanocrescent/nanotorch discussed in Chapter 6, integrated with a nanofluidic delivery system to co-localize molecules and particles onto the huge optical field of the nanoresonators' hot spots for single molecule detection or *in vivo* diagnosis. Furthermore, the molecules or nanoparticles could be controlled, such as with voltage potential as was demonstrated in Chapter 5. Manipulating and placing these molecules onto an area of maximum field intensity reliably and consistently will truly reap the benefits of the $|E|^4$ enhancement over the entire sensor area, which will lead to ultra-sensitive detectors, possibly down to single molecule identification. One possible solution would consist of a nanoresonator-nanotube array embedded in a membrane, as shown in Figure 7.1, in which the nanoresonators are constructed at the entrance of the nanotube. The membrane is integrated into microfluidic channels so molecules and particles can be manipulated and captured onto the rims of the nanoresonators. The integrated system consists of nanofluidic channels (nanotubes) sandwiched in between two layers of microfluidic channels. The nanotubes would act as conveyor belts to direct bioagents onto the rims of the nanocrescent/nanotorch nanoresonator structures. In order to take the next revolutionary step in SERS detection, it's important to co-localize the analytes onto nanometer-size volume of the active sites (hot spots) of the SERS substrate. By arranging the nanoresonator into a periodic array, the intensity and the spatial resolution of the SERS substrate will be greatly enhanced. The integrated nanoplasmonic-nanofluidic architecture would be truly a lab-on-a-chip solution.

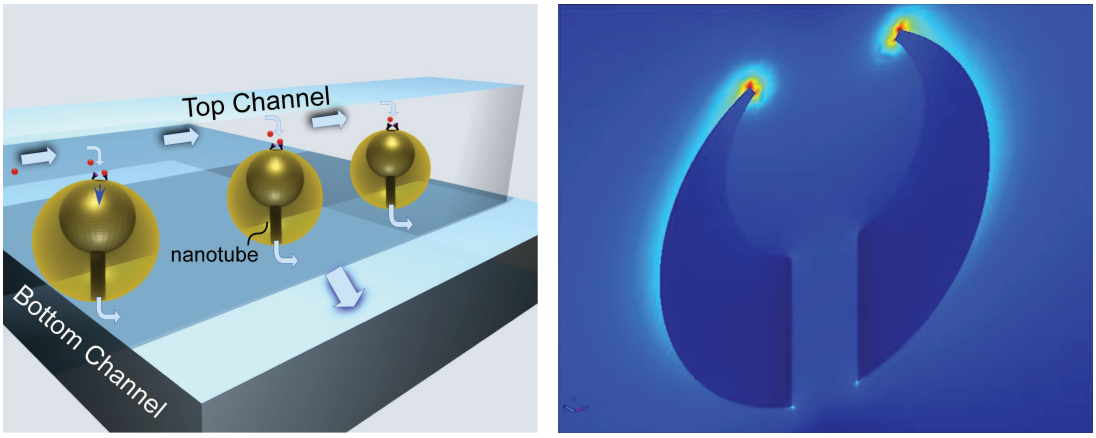

(a) (b)

Figure 7.1: a) Possible nanoresonator-nanotube plasmonic-fluidic structure to co-localize particles and molecules onto the hot spots of the plasmonic nanostructures b) FEM simulation of the nanostructure.

7.3 Concluding remarks

In the future, the inter-disciplinary collaborations between researchers in the plasmonics field and biological science will become even more important as they strive to solve many complex problems related to biology and medicine. Hopefully, new discoveries and inventions will make personalized medicine a reality and improve everyone's health and standard of living. Overall, plasmonics will undoubtedly improved everything ranging from photovoltaic solar panels on our rooftops, smaller transistor sizes due to sub-diffraction lithography and imaging, and smaller and more efficient LED lightings and lasers. The future is very bright and exciting for plasmonics.

Appendix A

Fabrication of fluidic channels

Fluidic channels are indispensable for biological sensing applications, like waveguides are indispensable to microwave engineering. They are conduits that transport the solvent and analyte onto the sensing sites. In this appendix, the fabrication process of microfluidic and nanofluidic channels are outlined.

The term soft lithography was coined in the late 1990's [160] to denote the process of using microelectronic fabrication processing techniques to fabricate large-area and non-planar, elastomeric polymer structures, primarily polydimethylsiloxane (PDMS), for transferring patterns from a master. Using PDMS is beneficial due to its fabrication simplicity, low-cost and reusability. This technique has been used to fabricate a host of devices, ranging from fluidic channels to microfluidic systems for bioassays and microreactors [161] to microelectromechanical systems (MEMS) [162].

A.1 Fabrication procedure for microfluidic channels

The fabrication procedure of using PDMS to make microfluidic channels are pretty straight-forward nowadays. First, it involves mixing Sylgard 184 (from Dow Corning) silicone elastomer with its corresponding curing agent with a weight ratio of 10:1. The mixing could be done by hand, but in our case, we put the mixture

into a capped plastic jar and placed it inside a centrifuge mixer machine (AR-250, Thinky Corp.) spinning at a high speed to mix the two. After the mixing cycle, the machine also defoams it to take out the bubbles. The second step consists of placing the silicon microfluidic pattern mask inside an enclosed box with a few drops of Chlorotrimethylsilane 97+% (from Sigma-Alrich), whose vapor will passivate the silicon surface so PDMS will peel off nicely during a subsequent step.

The microfluidic silicon mask was made from photolithography technique. Since these microfluidic channels were on the orders of 50 - 200 µm wide, high-quality (2400 dpi) transparency of the fluidic pattern was sufficient to use as mask. The transparency was taped to a quartz substrate before putting the quartz substrate into a mask aligner for UV exposure of the chemically amplified, negative SU8 photoresist (from MicroChem). The SU8 photoresist was then baked and developed with standard SU8 developer. Since SU8 is a negative photoresist, the portion of the resist that was exposed to UV radiation becomes insoluble to the developer, so the microfludic channels are actually SU8 ridges on the silicon wafer, which become air waveguides in the PDMS medium during the PDMS casting process.

The shape of a cup was made from aluminum foil around the silicon mask. Next, the PDMS mixture was then poured into the cup and degassed using a desiccator chamber to speed up the process, although it's not necessary. The sample was then left untouched for ∼10 min to ensure all the bubbles were out of the PDMS. Then the sample was placed inside a conventional oven and baked for 20 min at 90 °C. The sample was then cut at the edges of the fluidic mask to dislodge it from the aluminum foil. The PDMS peeled off easily from the silicon surface due to the monolayer of Chlorotrimethylsilane. Then, the inlets and outlets were created by punching into the PDMS with metallic tubing needles. The PDMS was laid flat on a surface and the needles were perpendicular to the PDMS surface. With one smooth motion, a firm pressure was applied to carve out a strain of PDMS. Care should be taken when punching these holes, otherwise leakage will occur if the pressure is too great or blockage will occur if the PDMS strain is not taken out cleanly.

A.2 Nanofluidic channels

To fabricate nanochannels, we first needed to make a mask consisting of 200-nm nanochannels using electron beam lithography. The process steps are shown in Figure A.1. The first step consists of spinning hydrogen silsesquioxane (HSQ) negative photoresist on a SOI wafer with a 3-µm-thick SiO_2 and a 250-nm-thick Si layer. Then the nanochannel pattern was exposed using e-beam and developed. Next, the silicon was etched using a RIE recipe mixture of SF_6 and C_4F_8, as shown in Figure A.1d. The rest of the photoresist was then removed. The other processing steps are similar to the fabrication of microfluidic channels: passivating the silicon surface with Chlorotrimethylsilane, casting the PDMS onto the mask, Figure A.1e, and peeling the PDMS mold from the silicon wafer, Figure A.1f. The only exception is the ratio of PDMS base to curing agent. It was determined experimentally to be optimal at a ratio of 5:1 and the bake time was 3 hrs.

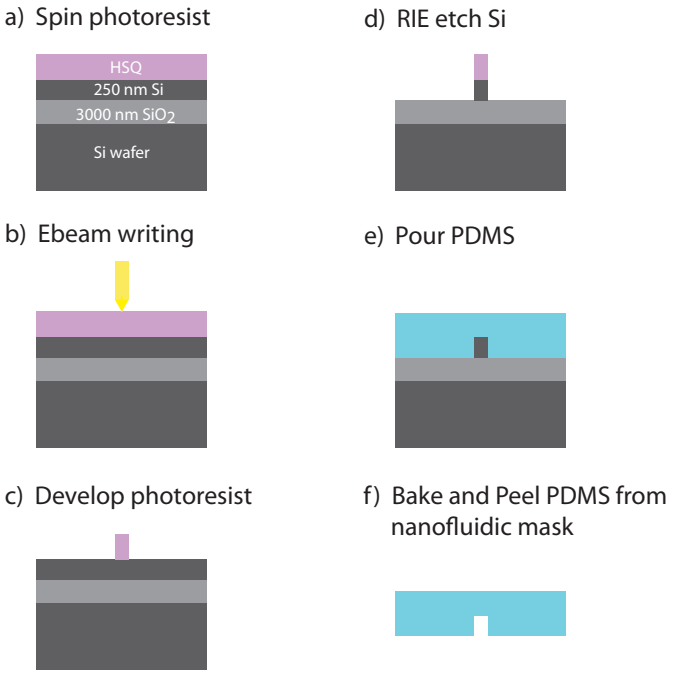

Figure A.1: Fabrication process of 200-nm fluidic channel using PDMS material: a) Spinning HSQ negative photoresist on SOI wafer. b) E-beam lithographical exposure. c) Baking and developing the photoresist. d) RIE etching and then surface treatment. e) Cast the PDMS by pouring it onto the SOI wafer. f) Bake and then peel PDMS from wafer.

Figure A.2a and b show SEM images of the bend and straight sections of the 200-nm nanochannel pattern, respectively.

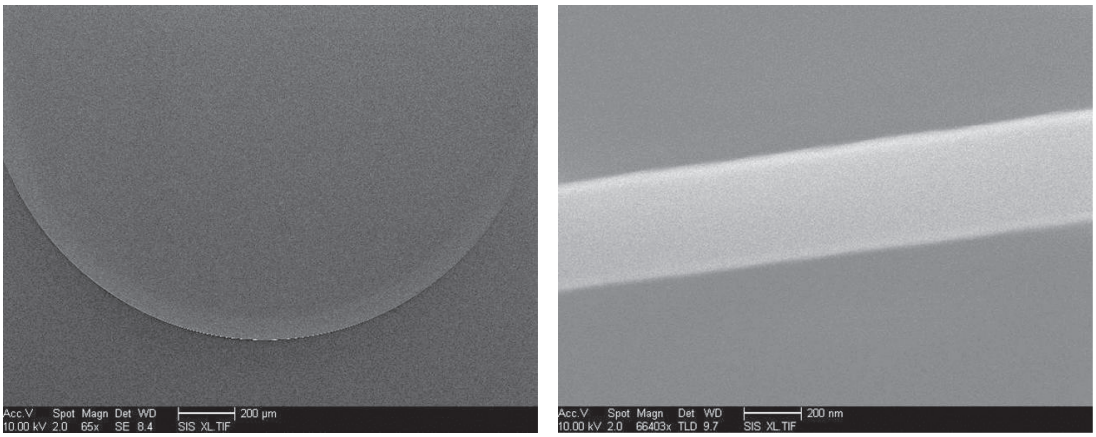

(a) (b)

Figure A.2: a) SEM of a curved 200-nm nanochannel silicon mask used to fabricate the PDMS nanochannel. b) Zoom-in of a straight 200-nm nanochannel silicon mask used to fabricate nanofluidic channel.

A.3 Integrating nanochannels into microchannels

In order to perform real bioassay experiments with the nanochannels, the liquid has to be delivered from the outside world into the nanochannels; therefore, we need to integrate the microchannels with the nanochannels, as shown in Figure A.3a, where the flow in the nanochannels is controlled by electrokinetic forces via voltage potential between the two electrodes of the two microchannels. Electrokinetic forces and their application in controlling nanoparticles are described in Chapter 5. The fabricated micro- and nanochannels are shown in Figure A.3b using a dark-field microscope. A zoom-in image of the nanochannel is shown in Figure A.3c. To ensure that fluid does not leak out from the sides of the nanochannels, it is important to treat the surface of the PDMS with oxygen plasma before binding it to a microscope slide. This step is shown in Figure A.3d after oxygen plasma and the binding process. It should be noted that the contrast is poorer in this case since the index difference between PDMS and the microscope slide is

less than the index difference between PDMS and air before the binding process as shown in Figure A.3c.

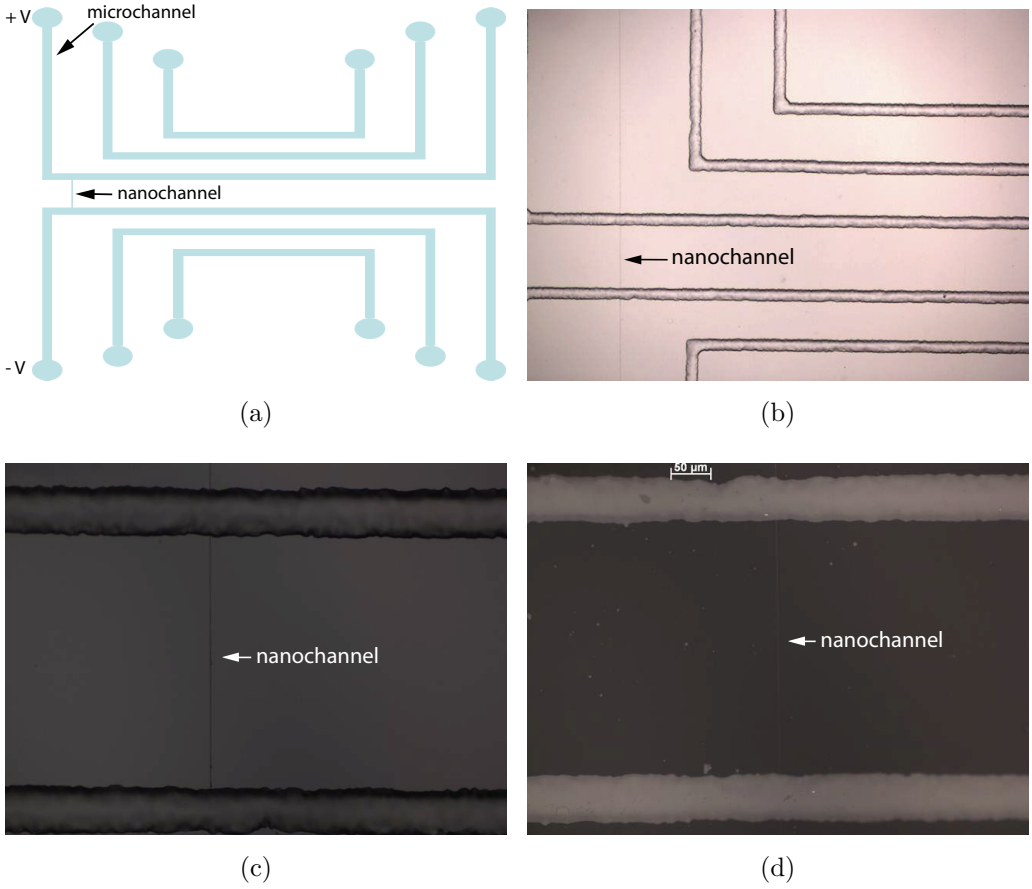

Figure A.3: a) Schematic of integrating the microchannels with the nanochannels when voltage is applied between two electrodes connected to the microchannels. The fluid in the nanochannel is then controlled by the voltage potential gradient. b) Dark-field image of the fabricated overlay of micro- and nanochannels. c) A zoom-in image of the channel before binding to microscope slide. d) After oxygen plasma treatment of PDMS surface and bonded to microscope slide.

A.4 Nanofluidic flow via voltage control

To test the integrity of the fluidic channels for any leak, phosphate buffered saline (PBS) solution with 40-nm fluorescent beads (from Life Technologies with excitation/emission wavelength at 505/515 nm) was injected into the microchan-

nels using a electrical pump. Figure A.4a shows a white light image of the fluidic channels, where the contrast of the channels with solution is low. The fluorescent beads were excited using a mercury lamp with the appropriate filters installed in the microscope. Figure A.4b shows the fluorescent image of the same channels. Now, the contrast of the channels with solution is high, while the channel without any solution is invisible. When voltage was applied between the two electrodes connected to the microchannels, fluidic flow in the nanochannel is seen as shown in Figure A.4c.

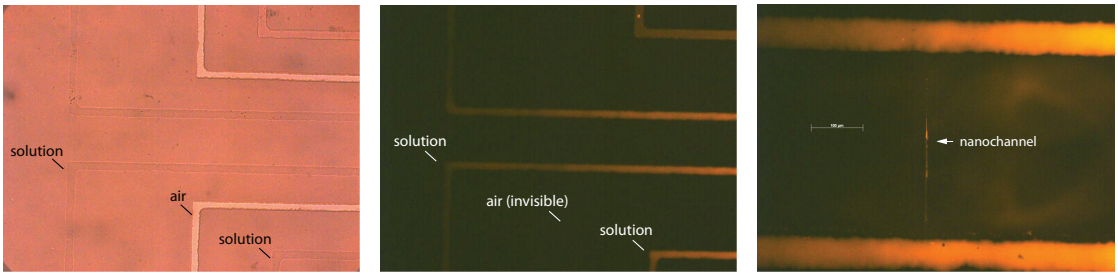

(a) (b) (c)

Figure A.4: a) White light image of solution in microchannels. b) Fluorescent image of microchannels. c) Fluorescent image of nanochannel when voltage is applied to the electrodes of the microchannels.

A.5 Summary

As seen in this appendix, nanofluidic flow was achieved via voltage control. Now, this concept can be used in conjunction with the nanotorch SERS substrate discussed in Chapter 6 so analyte can be delivered by the nanochannel onto the nanotorch structure for specific and isolated SERS detection. In the future, it may be possible to detect single molecule of a specific analyte at a specific active site.

Bibliography

[1] R. Wood, "On a remarkable case of uneven distribution of light in a diffraction grating spectrum," *The London, Edinburgh, and Dublin Philosophical Magazine and Journal of Science*, vol. 4, no. 21, pp. 396–402, 1902.

[2] P. Drude, "Zur elektronentheorie der metalle," *Annalen der Physik*, vol. 306, no. 3, pp. 566–613, 1900.

[3] G. Mie, "Beiträge zur optik trüber medien, speziell kolloidaler metallösungen," *Annalen der Physik*, vol. 330, no. 3, pp. 377–445, 1908.

[4] T. Ebbesen, H. Lezec, H. Ghaemi, T. Thio, and P. Wolff, "Extraordinary optical transmission through sub-wavelength hole arrays," *Nature*, vol. 391, no. 6668, pp. 667–669, 1998.

[5] D. Gramotnev and S. Bozhevolnyi, "Plasmonics beyond the diffraction limit," *Nature Photonics*, vol. 4, no. 2, pp. 83–91, 2010.

[6] E. Ozbay, "Plasmonics: merging photonics and electronics at nanoscale dimensions," *Science*, vol. 311, no. 5758, pp. 189–193, 2006.

[7] S. Bozhevolnyi, "Plasmonic nano-guides and circuits," in *Plasmonics and Metamaterials*, Optical Society of America, 2008.

[8] H. Atwater, "The promise of plasmonics," *Scientific American*, vol. 296, no. 4, pp. 56–62, 2007.

[9] A. Haes and R. Van Duyne, "A unified view of propagating and localized surface plasmon resonance biosensors," *Analytical and Bioanalytical Chemistry*, vol. 379, no. 7, pp. 920–930, 2004.

[10] T. Taton, C. Mirkin, and R. Letsinger, "Scanometric DNA array detection with nanoparticle probes," *Science*, vol. 289, no. 5485, pp. 1757–1760, 2000.

[11] A. Haes and R. Van Duyne, "A nanoscale optical biosensor: sensitivity and selectivity of an approach based on the localized surface plasmon resonance spectroscopy of triangular silver nanoparticles," *Journal of the American Chemical Society*, vol. 124, no. 35, pp. 10596–10604, 2002.

[12] A. Haes, S. Zou, G. Schatz, and R. Van Duyne, "Nanoscale optical biosensor: short range distance dependence of the localized surface plasmon resonance of noble metal nanoparticles," *The Journal of Physical Chemistry B*, vol. 108, no. 22, pp. 6961–6968, 2004.

[13] A. Haes, S. Zou, G. Schatz, and R. Van Duyne, "A nanoscale optical biosensor: the long range distance dependence of the localized surface plasmon resonance of noble metal nanoparticles," *The Journal of Physical Chemistry B*, vol. 108, no. 1, pp. 109–116, 2004.

[14] A. Haes, L. Chang, W. Klein, and R. Van Duyne, "Detection of a biomarker for alzheimer's disease from synthetic and clinical samples using a nanoscale optical biosensor," *Journal of the American Chemical Society*, vol. 127, no. 7, pp. 2264–2271, 2005.

[15] A. McFarland and R. Van Duyne, "Single silver nanoparticles as real-time optical sensors with zeptomole sensitivity," *Nano letters*, vol. 3, no. 8, pp. 1057–1062, 2003.

[16] J. Hulteen and R. Van Duyne, "Nanosphere lithography: A materials general fabrication process for periodic particle array surfaces," *Journal of Vacuum Science & Technology A: Vacuum, Surfaces, and Films*, vol. 13, no. 3, pp. 1553–1558, 1995.

[17] Y. Sun and Y. Xia, "Shape-controlled synthesis of gold and silver nanoparticles," *Science*, vol. 298, no. 5601, pp. 2176–2179, 2002.

[18] J. Love, B. Gates, D. Wolfe, K. Paul, and G. Whitesides, "Fabrication and wetting properties of metallic half-shells with submicron diameters," *Nano Letters*, vol. 2, no. 8, pp. 891–894, 2002.

[19] H. Wang, D. Brandl, F. Le, P. Nordlander, and N. Halas, "Nanorice: A hybrid plasmonic nanostructure," *Nano letters*, vol. 6, no. 4, pp. 827–832, 2006.

[20] J. Aizpurua, G. Bryant, L. Richter, F. De Abajo, B. Kelley, and T. Mallouk, "Optical properties of coupled metallic nanorods for field-enhanced spectroscopy," *Physical Review B*, vol. 71, no. 23, p. 235420, 2005.

[21] D. Fromm, A. Sundaramurthy, P. Schuck, G. Kino, and W. Moerner, "Gap-dependent optical coupling of single "bowtie" nanoantennas resonant in the visible," *Nano Letters*, vol. 4, no. 5, pp. 957–961, 2004.

[22] A. Kinkhabwala, Z. Yu, S. Fan, Y. Avlasevich, K. Müllen, and W. Moerner, "Large single-molecule fluorescence enhancements produced by a bowtie nanoantenna," *Nature Photonics*, vol. 3, no. 11, pp. 654–657, 2009.

[23] S. Maier, *Plasmonics: fundamentals and applications*. Springer Verlag, 2007.

[24] J. Jackson, *Classical electrodynamics*. John Wiley and Sons, 1999.

[25] M. Marder, *Condensed matter physics*. Wiley, 2000.

[26] C. Kittel, *Introduction to solid state physics*. Wiley New York, 1996.

[27] P. Johnson and R. Christy, "Optical constants of the noble metals," *Physical Review B*, vol. 6, no. 12, p. 4370, 1972.

[28] A. Vial, A. Grimault, D. Macías, D. Barchiesi, and M. de La Chapelle, "Improved analytical fit of gold dispersion: Application to the modeling of extinction spectra with a finite-difference time-domain method," *Physical Review B*, vol. 71, no. 8, p. 85416, 2005.

[29] S. Chuang, *Physics of optoelectronic devices*. Wiley New York, 1995.

[30] H. Raether, *Surface plasmons*. Springer-Verlag Berlin, 1988.

[31] R. Ritchie, "Plasma losses by fast electrons in thin films," *Physical Review*, vol. 106, no. 5, p. 874, 1957.

[32] H. Raether, *Excitation of plasmons and interband transitions by electrons*, vol. 88. Springer, 1980.

[33] E. Kretschmann and H. Raether, "Radiative decay of non radiative surface plasmons excited by light (surface plasma waves excitation by light and decay into photons applied to nonradiative modes)," *Zeitschrift Fuer Naturforschung, Teil A*, vol. 23, p. 2135, 1968.

[34] A. Otto, "Excitation of nonradiative surface plasma waves in silver by the method of frustrated total reflection," *Zeitschrift für Physik A Hadrons and Nuclei*, vol. 216, no. 4, pp. 398–410, 1968.

[35] R. Ritchie, E. Arakawa, J. Cowan, and R. Hamm, "Surface-plasmon resonance effect in grating diffraction," *Physical Review Letters*, vol. 21, no. 22, pp. 1530–1533, 1968.

[36] I. Hooper and J. Sambles, "Dispersion of surface plasmon polaritons on short-pitch metal gratings," *Physical Review B*, vol. 65, no. 16, p. 165432, 2002.

[37] W. Barnes, A. Dereux, and T. Ebbesen, "Surface plasmon subwavelength optics," *Nature*, vol. 424, no. 6950, pp. 824–830, 2003.

[38] H. Lezec, A. Degiron, E. Devaux, R. Linke, L. Martin-Moreno, F. Garcia-Vidal, and T. Ebbesen, "Beaming light from a subwavelength aperture," *Science*, vol. 297, no. 5582, pp. 820–822, 2002.

[39] H. Liu and P. Lalanne, "Microscopic theory of the extraordinary optical transmission," *Nature*, vol. 452, no. 7188, pp. 728–731, 2008.

[40] L. Martin-Moreno, F. Garcia-Vidal, H. Lezec, K. Pellerin, T. Thio, J. Pendry, and T. Ebbesen, "Theory of extraordinary optical transmission through subwavelength hole arrays," *Physical review letters*, vol. 86, no. 6, pp. 1114–1117, 2001.

[41] J. Homola, S. Yee, and G. Gauglitz, "Surface plasmon resonance sensors: review," *Sensors and Actuators B: Chemical*, vol. 54, no. 1-2, pp. 3–15, 1999.

[42] A. Bouhelier and G. Wiederrecht, "Surface plasmon rainbow jets," *Optics letters*, vol. 30, no. 8, pp. 884–886, 2005.

[43] B. Hecht, H. Bielefeldt, L. Novotny, Y. Inouye, and D. Pohl, "Local excitation, scattering, and interference of surface plasmons," *Physical Review Letters*, vol. 77, no. 9, pp. 1889–1892, 1996.

[44] J. Crowell and R. Ritchie, "Radiative decay of Coulomb-stimulated plasmons in spheres," *Physical Review*, vol. 172, pp. 436–440, 1968.

[45] E. Hutter and J. Fendler, "Exploitation of localized surface plasmon resonance," *Advanced Materials*, vol. 16, no. 19, pp. 1685–1706, 2004.

[46] M. Quinten, A. Leitner, J. Krenn, and F. Aussenegg, "Electromagnetic energy transport via linear chains of silver nanoparticles," *Optics Letters*, vol. 23, no. 17, pp. 1331–1333, 1998.

[47] M. Brongersma, J. Hartman, and H. Atwater, "Electromagnetic energy transfer and switching in nanoparticle chain arrays below the diffraction limit," *Physical Review B*, vol. 62, no. 24, pp. R16356–R16359, 2000.

[48] S. Maier, P. Kik, H. Atwater, S. Meltzer, E. Harel, B. Koel, and A. Requicha, "Local detection of electromagnetic energy transport below the diffraction limit in metal nanoparticle plasmon waveguides," *Nature Materials*, vol. 2, no. 4, pp. 229–232, 2003.

[49] A. J. Haes and R. P. Van Duyne, "A nanoscale optical biosensor: Sensitivity and selectivity of an approach based on the localized surface plasmon resonance spectroscopy of triangular silver nanoparticles," *Journal of the American Chemical Society*, vol. 124, no. 35, pp. 10596–10604, 2002.

[50] A. Haes, S. Zou, G. Schatz, and R. Van Duyne, "Nanoscale optical biosensor: short range distance dependence of the localized surface plasmon resonance of noble metal nanoparticles," *The Journal of Physical Chemistry B*, vol. 108, no. 22, pp. 6961–6968, 2004.

[51] A. Haes, S. Zou, G. Schatz, and R. Van Duyne, "A nanoscale optical biosensor: the long range distance dependence of the localized surface plasmon resonance of noble metal nanoparticles," *The Journal of Physical Chemistry B*, vol. 108, no. 1, pp. 109–116, 2004.

[52] K. Willets and R. Van Duyne, "Localized surface plasmon resonance spectroscopy and sensing," *Annu. Rev. Phys. Chem.*, vol. 58, pp. 267–297, 2007.

[53] C. Bohren and D. Huffman, *Absorption and scattering of light by small particles*. Wiley, 1983.

[54] U. Kreibig and M. Vollmer, *Optical properties of metal clusters*. Springer-Verlag, 1995.

[55] A. Wokaun, J. Gordon, and P. Liao, "Radiation damping in surface-enhanced Raman scattering," *Physical Review Letters*, vol. 48, no. 14, pp. 957–960, 1982.

[56] S. Link and M. El-Sayed, "Spectral properties and relaxation dynamics of surface plasmon electronic oscillations in gold and silver nanodots and nanorods," *The Journal of Physical Chemistry B*, vol. 103, no. 40, pp. 8410–8426, 1999.

[57] J. Krenn, A. Dereux, J. Weeber, E. Bourillot, Y. Lacroute, J. Goudonnet, G. Schider, W. Gotschy, A. Leitner, F. Aussenegg, and C. Girard, "Squeezing the optical near-field zone by plasmon coupling of metallic nanoparticles," *Physical Review Letters*, vol. 82, no. 12, pp. 2590–2593, 1999.

[58] Y. Lu, G. Liu, J. Kim, Y. Mejia, and L. Lee, "Nanophotonic crescent moon structures with sharp edge for ultrasensitive biomolecular detection by local electromagnetic field enhancement effect," *Nano Letters*, vol. 5, no. 1, pp. 119–124, 2005.

[59] J. Shumaker-Parry, H. Rochholz, and M. Kreiter, "Fabrication of crescent-shaped optical antennas," *Advanced Materials*, vol. 17, no. 17, pp. 2131–2134, 2005.

[60] B. Lamprecht, G. Schider, R. Lechner, H. Ditlbacher, J. Krenn, A. Leitner, and F. Aussenegg, "Metal nanoparticle gratings: influence of dipolar particle interaction on the plasmon resonance," *Physical review letters*, vol. 84, no. 20, pp. 4721–4724, 2000.

[61] C. Haynes, A. McFarland, L. Zhao, R. Van Duyne, G. Schatz, L. Gunnarsson, J. Prikulis, B. Kasemo, and M. Käll, "Nanoparticle optics: the importance of radiative dipole coupling in two-dimensional nanoparticle arrays," *The Journal of Physical Chemistry B*, vol. 107, no. 30, pp. 7337–7342, 2003.

[62] S. Zou and G. Schatz, "Narrow plasmonic/photonic extinction and scattering line shapes for one and two dimensional silver nanoparticle arrays," *The Journal of chemical physics*, vol. 121, p. 12606, 2004.

[63] N. Félidj, J. Aubard, G. Lévi, J. Krenn, G. Schider, A. Leitner, and F. Aussenegg, "Enhanced substrate-induced coupling in two-dimensional gold nanoparticle arrays," *Physical Review-Series B*, vol. 66, no. 24, pp. 245407–245407, 2002.

[64] D. Jeanmaire and R. Van Duyne, "Surface Raman spectroelectrochemistry: Part I. Heterocyclic, aromatic, and aliphatic amines adsorbed on the anodized silver electrode," *Journal of Electroanalytical Chemistry and Interfacial Electrochemistry*, vol. 84, no. 1, pp. 1–20, 1977.

[65] M. Albrecht and J. Creighton, "Anomalously intense Raman spectra of pyridine at a silver electrode," *Journal of the American Chemical Society*, vol. 99, no. 15, pp. 5215–5217, 1977.

[66] M. Moskovits, "Surface roughness and the enhanced intensity of Raman scattering by molecules adsorbed on metals," *The Journal of Chemical Physics*, vol. 69, p. 4159, 1978.

[67] S. Nie and S. Emory, "Probing single molecules and single nanoparticles by surface-enhanced Raman scattering," *Science*, vol. 275, no. 5303, p. 1102, 1997.

[68] K. Kneipp, Y. Wang, H. Kneipp, L. Perelman, I. Itzkan, R. Dasari, and M. Feld, "Single molecule detection using surface-enhanced Raman scattering (SERS)," *Physical Review Letters*, vol. 78, no. 9, pp. 1667–1670, 1997.

[69] C. Raman and K. Krishnan, "A new type of secondary radiation," *Nature*, vol. 121, no. 3048, pp. 501–502, 1928.

[70] M. Kerker, D. Wang, and H. Chew, "Surface enhanced Raman scattering (SERS) by molecules adsorbed at spherical particles: errata," *Applied Optics*, vol. 19, no. 24, pp. 4159–4174, 1980.

[71] M. Moskovits, "Surface-enhanced spectroscopy," *Rev. Mod. Phys.*, vol. 57, pp. 783–826, 1985.

[72] J. Gersten and A. Nitzan, "Electromagnetic theory of enhanced Raman scattering by molecules adsorbed on rough surfaces," *The Journal of Chemical Physics*, vol. 73, p. 3023, 1980.

[73] P. Liao and A. Wokaun, "Lightning rod effect in surface enhanced Raman scattering," *The Journal of Chemical Physics*, vol. 76, p. 751, 1982.

[74] C. Nylander, B. Liedberg, and T. Lind, "Gas detection by means of surface plasmon resonance," *Sensors and Actuators*, vol. 3, pp. 79–88, 1983.

[75] D. Cullen, R. Brown, and C. Lowe, "Detection of immuno-complex formation via surface plasmon resonance on gold-coated diffraction gratings," *Biosensors*, vol. 3, no. 4, pp. 211–225, 1988.

[76] M. Jory, G. Bradberry, P. Cann, and J. Sambles, "A surface-plasmon-based optical sensor using acousto-optics," *Measurement Science and Technology*, vol. 6, p. 1193, 1995.

[77] C. Lawrence, N. Geddes, D. Furlong, and J. Sambles, "Surface plasmon resonance studies of immunoreactions utilizing disposable diffraction gratings," *Biosensors and Bioelectronics*, vol. 11, no. 4, pp. 389–400, 1996.

[78] A. Brolo, R. Gordon, B. Leathem, and K. Kavanagh, "Surface plasmon sensor based on the enhanced light transmission through arrays of nanoholes in gold films," *Langmuir*, vol. 20, no. 12, pp. 4813–4815, 2004.

[79] K. Tetz, L. Pang, and Y. Fainman, "High-resolution surface plasmon resonance sensor based on linewidth-optimized nanohole array transmittance," *Optics letters*, vol. 31, no. 10, pp. 1528–1530, 2006.

[80] M. Stewart, N. Mack, V. Malyarchuk, J. Soares, T. Lee, S. Gray, R. Nuzzo, and J. Rogers, "Quantitative multispectral biosensing and 1D imaging using quasi-3D plasmonic crystals," *Proceedings of the National Academy of Sciences*, vol. 103, no. 46, pp. 17143–17148, 2006.

[81] A. De Leebeeck, L. Kumar, V. de Lange, D. Sinton, R. Gordon, and A. Brolo, "On-chip surface-based detection with nanohole arrays," *Analytical Chemistry*, vol. 79, no. 11, pp. 4094–4100, 2007.

[82] L. Pang, G. Hwang, B. Slutsky, and Y. Fainman, "Spectral sensitivity of two-dimensional nanohole array surface plasmon polariton resonance sensor," *Applied Physics Letters*, vol. 91, no. 12, pp. 123112–123112, 2007.

[83] A. Lesuffleur, H. Im, N. Lindquist, and S. Oh, "Periodic nanohole arrays with shape-enhanced plasmon resonance as real-time biosensors," *Applied Physics Letters*, vol. 90, no. 24, p. 243110, 2007.

[84] P. Stark, A. Halleck, and D. Larson, "Short order nanohole arrays in metals for highly sensitive probing of local indices of refraction as the basis for a highly multiplexed biosensor technology," *Methods*, vol. 37, no. 1, pp. 37–47, 2005.

[85] W. Fan, S. Zhang, B. Minhas, K. Malloy, and S. Brueck, "Enhanced infrared transmission through subwavelength coaxial metallic arrays," *Physical Review Letters*, vol. 94, no. 3, p. 33902, 2005.

[86] S. Wu, Q. Wang, X. Yin, J. Li, D. Zhu, S. Liu, and Y. Zhu, "Enhanced optical transmission: role of the localized surface plasmon," *Applied Physics Letters*, vol. 93, p. 101113, 2008.

[87] T. Kelf, Y. Sugawara, R. Cole, J. Baumberg, M. Abdelsalam, S. Cintra, S. Mahajan, A. Russell, and P. Bartlett, "Localized and delocalized plasmons in metallic nanovoids," *Physical Review B*, vol. 74, no. 24, p. 245415, 2006.

[88] L. Pang, W. Nakagawa, and Y. Fainman, "Fabrication of two-dimensional photonic crystals with controlled defects by use of multiple exposures and direct write," *Applied Optics*, vol. 42, no. 27, pp. 5450–5456, 2003.

[89] D. Kim, S. Hohng, V. Malyarchuk, Y. Yoon, Y. Ahn, K. Yee, J. Park, J. Kim, Q. Park, and C. Lienau, "Microscopic origin of surface-plasmon radiation in plasmonic band-gap nanostructures," *Physical Review Letters*, vol. 91, no. 14, p. 143901, 2003.

[90] R. Múller, V. Malyarchuk, and C. Lienau, "Three-dimensional theory on light-induced near-field dynamics in a metal film with a periodic array of nanoholes," *Physical Review B*, vol. 68, no. 20, p. 205415, 2003.

[91] P. de Gennes, "Wetting: statics and dynamics," *Reviews of Modern Physics*, vol. 57, no. 3, p. 827, 1985.

[92] en.wikipedia.org.

[93] L. Jung, C. Campbell, T. Chinowsky, N. Mimi, and S. Yee, "Quantitative interpretation of the response of surface plasmon resonance sensors to adsorbed films," *Langmuir*, vol. 14, no. 19, pp. 5636–5648, 1998.

[94] E. Stenberg, B. Persson, H. Roos, and C. Urbaniczky, "Quantitative determination of surface concentration of protein with surface plasmon resonance using radiolabeled proteins," *Journal of Colloid and Interface Science*, vol. 143, no. 2, pp. 513–526, 1991.

[95] P. Hanarp, M. Käll, and D. Sutherland, "Optical properties of short range ordered arrays of nanometer gold disks prepared by colloidal lithography," *The Journal of Physical Chemistry B*, vol. 107, no. 24, pp. 5768–5772, 2003.

[96] T. Rindzevicius, Y. Alaverdyan, A. Dahlin, F. Höök, D. Sutherland, and M. Käll, "Plasmonic sensing characteristics of single nanometric holes," *Nano Letters*, vol. 5, no. 11, pp. 2335–2339, 2005.

[97] J. Anker, W. Hall, O. Lyandres, N. Shah, J. Zhao, and R. Van Duyne, "Biosensing with plasmonic nanosensors," *Nature Materials*, vol. 7, no. 6, pp. 442–453, 2008.

[98] L. Pang, K. Tetz, and Y. Fainman, "Observation of the splitting of degenerate surface plasmon polariton modes in a two-dimensional metallic nanohole array," *Applied Physics Letters*, vol. 90, no. 11, pp. 111103–111103, 2007.

[99] J. Homola, *Surface plasmon resonance based sensors*, vol. 4. Springer Verlag, 2006.

[100] F. Yu and W. Knoll, "Immunosensor with self-referencing based on surface plasmon diffraction," *Analytical chemistry*, vol. 76, no. 7, pp. 1971–1975, 2004.

[101] H. Lu, J. Homola, C. Campbell, G. Nenninger, S. Yee, and B. Ratner, "Protein contact printing for a surface plasmon resonance biosensor with on-chip referencing," *Sensors and Actuators B: Chemical*, vol. 74, no. 1-3, pp. 91–99, 2001.

[102] D. Myszka, "Improving biosensor analysis," *Journal of Molecular Recognition*, vol. 12, no. 5, pp. 279–284, 1999.

[103] W. Chan and S. Nie, "Quantum dot bioconjugates for ultrasensitive nonisotopic detection," *Science*, vol. 281, no. 5385, pp. 2016–2018, 1998.

[104] P. Alivisatos, "The use of nanocrystals in biological detection," *Nature Biotechnology*, vol. 22, no. 1, pp. 47–52, 2004.

[105] I. Medintz, H. Uyeda, E. Goldman, and H. Mattoussi, "Quantum dot bioconjugates for imaging, labelling and sensing," *Nature Materials*, vol. 4, no. 6, pp. 435–446, 2005.

[106] H. He, H. Zhang, Q. Li, T. Zhu, S. Li, and Z. Liu, "Fabrication of designed architectures of Au nanoparticles on solid substrate with printed self-assembled monolayers as templates," *Langmuir*, vol. 16, no. 8, pp. 3846–3851, 2000.

[107] A. Kalsin, M. Fialkowski, M. Paszewski, S. Smoukov, K. Bishop, and B. Grzybowski, "Electrostatic self-assembly of binary nanoparticle crystals with a diamond-like lattice," *Science*, vol. 312, no. 5772, pp. 420–424, 2006.

[108] W. Shenton, S. A. Davis, and S. Mann, "Directed self-assembly of nanoparticles into macroscopic materials using antibody-antigen recognition," *Advanced Materials*, vol. 11, no. 6, pp. 449–452, 1999.

[109] M. Warner and J. Hutchison, "Linear assemblies of nanoparticles electrostatically organized on DNA scaffolds," *Nature Materials*, vol. 2, no. 4, pp. 272–277, 2003.

[110] J. Zheng, P. Constantinou, C. Micheel, A. Alivisatos, R. Kiehl, and N. Seeman, "Two-dimensional nanoparticle arrays show the organizational power of robust DNA motifs," *Nano Letters*, vol. 6, no. 7, pp. 1502–1504, 2006.

[111] J. Fendler, "Self-assembled nanostructured materials," *Chemistry of Materials*, vol. 8, no. 8, pp. 1616–1624, 1996.

[112] A. Tao, P. Sinsermsuksakul, and P. Yang, "Tunable plasmonic lattices of silver nanocrystals," *Nature Nanotechnology*, vol. 2, no. 7, pp. 435–440, 2007.

[113] D. LaVan, T. McGuire, R. Langer, *et al.*, "Small-scale systems for in vivo drug delivery," *Nature Biotechnology*, vol. 21, no. 10, pp. 1184–1191, 2003.

[114] A. Ashkin, J. Dziedzic, J. Bjorkholm, and S. Chu, "Observation of a single-beam gradient force optical trap for dielectric particles," *Optics letters*, vol. 11, no. 5, pp. 288–290, 1986.

[115] D. Grier *et al.*, "A revolution in optical manipulation," *Nature*, vol. 424, no. 6950, pp. 810–816, 2003.

[116] L. Ma, R. Subramanian, H. Huang, V. Ray, C. Kim, and S. Koh, "Electrostatic funneling for precise nanoparticle placement: a route to wafer-scale integration," *Nano Letters*, vol. 7, no. 2, pp. 439–445, 2007.

[117] Y. Huang, X. Duan, Q. Wei, and C. Lieber, "Directed assembly of one-dimensional nanostructures into functional networks," *Science*, vol. 291, no. 5504, pp. 630–633, 2001.

[118] Y. Xia, Y. Yin, Y. Lu, and J. McLellan, "Template-assisted self-assembly of spherical colloids into complex and controllable structures," *Advanced Functional Materials*, vol. 13, no. 12, pp. 907–918, 2003.

[119] Y. Cui, M. Björk, J. Liddle, C. Sönnichsen, B. Boussert, and A. Alivisatos, "Integration of colloidal nanocrystals into lithographically patterned devices," *Nano Letters*, vol. 4, no. 6, pp. 1093–1098, 2004.

[120] J. MacInnes, "Computation of reacting electrokinetic flow in microchannel geometries," *Chemical Engineering Science*, vol. 57, no. 21, pp. 4539–4558, 2002.

[121] S. Baker, M. Pocha, A. Chang, D. Sirbuly, S. Cabrini, S. Dhuey, T. Bond, and S. Létant, "Detection of bio-organism simulants using random binding on a defect-free photonic crystal," *Applied Physics Letters*, vol. 97, p. 113701, 2010.

[122] H. Hu, "Direct simulation of flows of solid-liquid mixtures," *International Journal of Multiphase Flow*, vol. 22, no. 2, pp. 335–352, 1996.

[123] C. Ye and D. Li, "3-D transient electrophoretic motion of a spherical particle in a T-shaped rectangular microchannel," *Journal of Colloid and Interface Science*, vol. 272, no. 2, pp. 480–488, 2004.

[124] H. Keh and J. Anderson, "Boundary effects on electrophoretic motion of colloidal spheres," *Journal of Fluid Mechanics*, vol. 153, pp. 417–39, 1985.

[125] S. Davison and K. Sharp, "Boundary effects on the electrophoretic motion of cylindrical particles: Concentrically and eccentrically-positioned particles in a capillary," *Journal of Colloid and Interface Science*, vol. 303, no. 1, pp. 288–297, 2006.

[126] N. Takashi and T. Hughes, "An arbitrary Lagrangian-Eulerian finite element method for interaction of fluid and a rigid body," *Computer Methods in Applied Mechanics and Engineering*, vol. 95, no. 1, pp. 115–138, 1992.

[127] X. Xuan, S. Raghibizadeh, and D. Li, "Wall effects on electrophoretic motion of spherical polystyrene particles in a rectangular poly-(dimethylsiloxane) microchannel," *Journal of Colloid and Interface Science*, vol. 296, no. 2, pp. 743–748, 2006.

[128] L. Pang, W. Nakagawa, and Y. Fainman, "Fabrication of two-dimensional photonic crystals with controlled defects by use of multiple exposures and direct write," *Applied Optics*, vol. 42, no. 27, pp. 5450–5456, 2003.

[129] H. Chen, L. Pang, A. Kher, and Y. Fainman, "Three-dimensional composite metallodielectric nanostructure for enhanced surface plasmon resonance sensing," *Applied Physics Letters*, vol. 94, p. 073117, 2009.

[130] J. Fan, C. Wu, K. Bao, J. Bao, R. Bardhan, N. Halas, V. Manoharan, P. Nordlander, G. Shvets, and F. Capasso, "Self-assembled plasmonic nanoparticle clusters," *Science*, vol. 328, no. 5982, pp. 1135–1138, 2010.

[131] K. Li, M. Stockman, and D. Bergman, "Self-similar chain of metal nanospheres as an efficient nanolens," *Physical Review Letters*, vol. 91, no. 22, p. 227402, 2003.

[132] S. Maier, M. Brongersma, P. Kik, S. Meltzer, A. Requicha, and H. Atwater, "Plasmonics–a route to nanoscale optical devices," *Advanced Materials*, vol. 13, no. 19, p. 2, 2001.

[133] D. Fromm, A. Sundaramurthy, A. Kinkhabwala, P. Schuck, G. Kino, and W. Moerner, "Exploring the chemical enhancement for surface-enhanced Raman scattering with Au bowtie nanoantennas," *The Journal of Chemical Physics*, vol. 124, p. 061101, 2006.

[134] H. Rochholz, N. Bocchio, and M. Kreiter, "Tuning resonances on crescent-shaped noble-metal nanoparticles," *New Journal of Physics*, vol. 9, p. 53, 2007.

[135] K. Li, L. Clime, B. Cui, and T. Veres, "Surface enhanced Raman scattering on long-range ordered noble-metal nanocrescent arrays," *Nanotechnology*, vol. 19, p. 145305, 2008.

[136] R. Bukasov and J. Shumaker-Parry, "Highly tunable infrared extinction properties of gold nanocrescents," *Nano Letters*, vol. 7, no. 5, pp. 1113–1118, 2007.

[137] X. Liu, N. Linn, C. Sun, and P. Jiang, "Templated fabrication of metal half-shells for surface-enhanced Raman scattering," *Phys. Chem. Chem. Phys.*, vol. 12, no. 6, pp. 1379–1387, 2010.

[138] J. Kim, G. Liu, Y. Lu, and L. Lee, "Intra-particle plasmonic coupling of tip and cavity resonance modes in metallic apertured nanocavities," *Optics Express*, vol. 13, no. 21, pp. 8332–8338, 2005.

[139] B. Ross and L. Lee, "Plasmon tuning and local field enhancement maximization of the nanocrescent," *Nanotechnology*, vol. 19, p. 275201, 2008.

[140] F. Hao, P. Nordlander, Y. Sonnefraud, P. Dorpe, and S. Maier, "Tunability of subradiant dipolar and fano-type plasmon resonances in metallic ring/disk cavities: implications for nanoscale optical sensing," *ACS Nano*, vol. 3, no. 3, pp. 643–652, 2009.

[141] Y. Zhang, T. Jia, D. Feng, and Z. Xu, "Quadrupole plasmon resonance mode in nanocrescent/nanodisk structure: local field enhancement and tunability in the visible light region," *Applied Physics Letters*, vol. 98, p. 163110, 2011.

[142] J. Berenger, "A perfectly matched layer for the absorption of electromagnetic waves," *Journal of Computational Physics*, vol. 114, no. 2, pp. 185–200, 1994.

[143] J. Stratton, *Electromagnetic theory*. McGraw-Hill, 1941.

[144] COMSOL, "COMSOL Multiphysics user's guide ver 3.5a," tech. rep., COMSOL AB, Stockhom, Sweden, 2009.

[145] J. Aizpurua, P. Hanarp, D. Sutherland, M. Käll, G. Bryant, and F. Garcia de Abajo, "Optical properties of gold nanorings," *Physical Review Letters*, vol. 90, no. 5, p. 57401, 2003.

[146] K. Kneipp, A. Haka, H. Kneipp, K. Badizadegan, N. Yoshizawa, C. Boone, K. Shafer-Peltier, J. Motz, R. Dasari, and M. Feld, "Surface-enhanced Raman spectroscopy in single living cells using gold nanoparticles," *Applied Spectroscopy*, vol. 56, no. 2, pp. 150–154, 2002.

[147] A. Michaels, M. Nirmal, and L. Brus, "Surface enhanced Raman spectroscopy of individual rhodamine 6G molecules on large Ag nanocrystals," *Journal of the American Chemical Society*, vol. 121, no. 43, pp. 9932–9939, 1999.

[148] K. Kneipp, H. Kneipp, V. Bhaskaran Kartha, R. Manoharan, G. Deinum, I. Itzkan, R. Dasari, and M. Feld, "Detection and identification of a single DNA base molecule using surface-enhanced Raman scattering (SERS)," *Physical Review E*, vol. 57, no. 6, pp. R6281–R6284, 1998.

[149] K. Kneipp, H. Kneipp, R. Manoharan, E. Hanlon, I. Itzkan, R. Dasari, and M. Feld, "Extremely large enhancement factors in surface-enhanced Raman scattering for molecules on colloidal gold clusters," *Applied Spectroscopy*, vol. 52, no. 12, pp. 1493–1497, 1998.

[150] E. Le Ru, E. Blackie, M. Meyer, and P. Etchegoin, "Surface enhanced Raman scattering enhancement factors: a comprehensive study," *The Journal of Physical Chemistry C*, vol. 111, no. 37, pp. 13794–13803, 2007.

[151] W. Cai, B. Ren, X. Li, C. She, F. Liu, X. Cai, and Z. Tian, "Investigation of surface-enhanced Raman scattering from platinum electrodes using a confocal Raman microscope: dependence of surface roughening pretreatment," *Surface Science*, vol. 406, no. 1, pp. 9–22, 1998.

[152] L. Wan, M. Terashima, H. Noda, and M. Osawa, "Molecular orientation and ordered structure of benzenethiol adsorbed on gold (111)," *The Journal of Physical Chemistry B*, vol. 104, no. 15, pp. 3563–3569, 2000.

[153] R. Aggarwal, L. Farrar, E. Diebold, and D. Polla, "Measurement of the absolute Raman scattering cross section of the 1584-cm^{-1} band of benzenethiol and the surface-enhanced Raman scattering cross section enhancement factor for femtosecond laser-nanostructured substrates," *Journal of Raman Spectroscopy*, vol. 40, no. 9, pp. 1331–1333, 2009.

[154] C. Szafranski, W. Tanner, P. Laibinis, and R. Garrell, "Surface-enhanced Raman spectroscopy of aromatic thiols and disulfides on gold electrodes," *Langmuir*, vol. 14, no. 13, pp. 3570–3579, 1998.

[155] S. W. Han, S. J. Lee, and K. Kim, "Self-assembled monolayers of aromatic thiol and selenol on silver: Comparative study of adsorptivity and stability," *Langmuir*, vol. 17, no. 22, pp. 6981–6987, 2001.

[156] H. Chen, L. Pang, M. Gordon, and Y. Fainman, "Real-time template-assisted manipulation of nanoparticles in a multilayer nanofluidic chip," *Small*, vol. 7, no. 19, pp. 2678–2678, 2011.

[157] Y. Xia, Y. Yin, Y. Lu, and J. McLellan, "Template-assisted self-assembly of spherical colloids into complex and controllable structures," *Advanced Functional Materials*, vol. 13, no. 12, pp. 907–918, 2003.

[158] S. Hur, Y. Zhao, Y. Li, E. Botvinick, and S. Chien, "Live cells exert 3-dimensional traction forces on their substrata," *Cellular and Molecular Bioengineering*, vol. 2, no. 3, pp. 425–436, 2009.

[159] Y. Hu and S. Chien, "Dynamic motion of paxillin on actin filaments in living endothelial cells," *Biochemical and Biophysical Research Communications*, vol. 357, no. 4, pp. 871–876, 2007.

[160] Y. Xia and G. Whitesides, "Soft lithography," *Annual review of materials science*, vol. 28, no. 1, pp. 153–184, 1998.

[161] S. Quake and A. Scherer, "From micro-to nanofabrication with soft materials," *Science*, vol. 290, no. 5496, pp. 1536–1540, 2000.

[162] T. Deng, G. Whitesides, M. Radhakrishnan, G. Zabow, and M. Prentiss, "Manipulation of magnetic microbeads in suspension using micromagnetic systems fabricated with soft lithography," *Applied Physics Letters*, vol. 78, p. 1775, 2001.